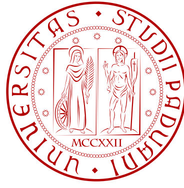

UNIVERSITY OF PADOVA
Faculty of Engineering
Department of Information Engineering

Gallium Nitride simulations using Sentaurus software

student
De Brida Christian

supervisors:
Zanoni Enrico (university supervisor)
Meneghini Matteo (university co-supervisor)
Curatola Gilberto (NXP supervisor)

Specialization in Electronic Engineering

6th December 2010
Academic year 2010/2011

UNIVERSITY OF PADOVA
Faculty of Engineering
Department of Information Engineering

Abstract

by De Brida Christian

GaN material is reaching a lot of interests because of its physical characteristics, among them have to be cited the high band gap, the direct band gap, the high critical electric field, about 10 times more that that of silicon, and the high carrier velocity saturation. Moreover high electron concentration is present in the *AlGaN/GaN* interface due to the piezoelectric and spontaneous polarizations. This high concentration is called two-dimensional-electron-gas (2DEG) allowing higher mobility than the electrons in the bulk material. These features make this material the most suitable for UV and white LED and for high frequency and high power applications, capable to operate at higher temperature then the *Si*-based devices.

Simulation activity is very useful since it can help the understanding of how the device works as well as it can be utilized in order to reproduce or predict a trend, without using real devices. Fabricating devices with wide band gap materials like *GaN* are very expensive, just think that a *GaN* row wafer costs thousands of $, so simulations can reduce the cost of a device studying. Moreover simulations are used beside the device characterization to improve the comprehension of the physical phenomena which are behind a certain behaviour.

My activity consisted in the obtaining of simulation decks which have been firstly calibrated using experimental data. At this purpose I got measurement data from NXP and, basing on these, I tried to match simulated DC characteristics with the experimental ones, both *IdVg* and *IdVd*, of two different HEMT devices. During this match trial we discovered that the simulator does not treat properly the deep level doping. Indeed in one device we implemented the iron doping in the buffer layer and we did it creating a new doping element in the materials list file but, since this material creates deep acceptor layer, the results were different respect to the case in which the doping was implemented as traps instead of dopant material. Beside the DC measurement data we got the AC experimental data as well, hence we could further improve the model. AC simulations are important in order to check the capacitive load, mostly when the device is inserted into a RF circuit or when the HEMT is used as a switch.

HEMT devices based on *GaN* and *AlGaN* suffers from strong gate leakage when high reverse voltage is applied on the gate and this could be a problem for the power consumption of the entire circuit. The gate leakage seems to be derived from traps below the gate region, present because of the damage produced by the etch process and due to the high stress which the gate edges undergo because of the high electric field. By adding a traps layer beneath the gate we sought to simulate the leakage behaviour and hence to see if these traps could be a reason for the gate leakage.

It is well known that *GaN* is a direct band material with the feature of the negative differential velocity. Based on a paper from Farahmand et all, in which a new mobility model for *GaN* has been calibrated by means of Monte Carlo simulations, we attempted to implement this model into our simulations in such a way to see whether the DC simulations could be improved.

The scope of the devices I simulated is the high voltage automotive field, so an electric field characterization within the device must be done. In high voltage regime the maximum electric field (EF) is located beneath the gate edge, region in which device failure could happen. A typical choice to spread the EF along the channel is by the field plate (FP), a gate extension towards the drain. Since it has been found that the FP helps to lower the EF peak below the gate and hence to improve the device reliability, simulations have been carried out in such a way to test the effect of the FP.

For all of these simulations I used Sentaurus software, version 2010.03, provided by Synopsys.

Acknowledgements

I would like to thank my professors Enrico Zanoni and Matteo Meneghini for gave me the opportunity to do my thesis activity in NXP Leuven.

As soon as I entered in NXP I got the feeling of a professional and stimulant environment, where the people can improve. Indeed, here I found very professional persons, like Gilberto Curatola, my internal supervisor, Jan Sonsky, the team leader, and the other components of the group in which I joined. In NXP I had the opportunity to work in a very young field: *Gallium Nitride devices*. Thanks to Gilberto I could improve my knowledge about GaN materials and mostly he helped me to become familiar with the simulator.

Thanks to Giovanni Verzellesi, a professor from Reggio Emilia, who gave me some precious hints inherent to the simulations.

I cannot forget to mention the friends I met here in Leuven with whom I shared a lot of great moments. Thanks to: Thilo, Yannick, Wagdy, Genya, Jimmy, Andreas, Alessandro and many others.

Thanks to my parents for let me decide every time what I want to do and thanks to my relatives in general for their support.

Thanks to Lydia for her patience to wait for my return. From now on we can finally start thinking about our life.

Thanks to all for this amazing experience.

Contents

Abstract **i**

Acknowledgements **iv**

Abbreviations **vii**

Physical Constants **viii**

1 Introduction **1**
1.1 Thesis organization . . . 3

2 Wide band gap materials **5**
2.1 Materials properties . . . 5
2.1.1 Gallium Nitride (GaN) . . . 6
2.1.2 Aluminium Nitride (AlN) . . . 8
2.1.3 Indium Nitride *(InN)* . . . 9
2.1.4 Aluminium Gallium Nitride ($Al_xGa_{1-x}N$) . . . 10
2.1.5 Indium Gallium Nitride ($In_xGa_{1-x}N$) and Indium Aluminium Nitride ($In_xAl_{1-x}N$) . . . 10
2.2 Substrate . . . 10
2.2.1 Sapphire substrate . . . 11
2.2.2 SiC substrate . . . 11
2.2.3 Si substrate . . . 12
2.2.4 AlN substrate . . . 12
2.3 Applications . . . 12
2.3.1 Optical applications . . . 13
2.3.1.1 LED . . . 13
2.3.1.2 LASER . . . 14
2.3.2 Electronic applications . . . 15
2.3.3 Military applications . . . 15
2.3.4 Commercial Applications . . . 15
2.4 Semiconductor physics . . . 16
2.4.1 Spontaneous and piezoelectric polarization . . . 17
2.4.2 Charge density . . . 20
2.5 Doping . . . 27
2.5.1 N-Doping . . . 28

2.5.2 P-Doping . . . 28
2.6 Traps in *GaN* and *AlGaN* . . . 29
2.6.1 Current Collapse . . . 32

3 HEMTs simulations 36
3.1 First device . . . 37
3.1.1 Device structure . . . 37
3.1.2 DC simulations . . . 38
3.2 Second device . . . 47
3.2.1 Device structure . . . 50
3.2.2 DC simulations . . . 50
3.2.3 AC simulations . . . 54
3.2.4 Gate Leakage . . . 56
3.2.5 New mobility model . . . 64
3.2.6 Electric Field evaluation . . . 68

4 Summary and Conclusions 75

A Code 79
A.1 Parameters files . . . 79
A.1.1 GaN.par . . . 79
A.1.2 AlN.par . . . 86
A.2 command files . . . 91
A.2.1 Header . . . 91
A.2.2 DC simulations . . . 93
A.2.3 AC simulations . . . 97
A.3 New mobility model files . . . 100
A.3.1 High Field Mobility . . . 100
A.3.2 Low Field Mobility . . . 107

Bibliography 111

Abbreviations

Fe	Iron
Mg	Magnesium
In	Indium
O	Oxygen
Si	Silicon
GaN	**Ga**llium **N**itride
AlGaN	**Al**uminium **Ga**llium **N**itride
SiC	**Si**licon **C**arbide
CB	**C**onduction **B**and
VB	**V**alence **B**and
EF	**E**lectric **F**ield
BV	**B**reakdown **V**oltage
2DEG	**2** **D**imentional **E**lectron **G**as
WBG	**W**ide **B**and **G**ap
CTE	**C**oefficient of **T**hermal **E**xpansion
FP	**F**ield **P**late
HEMT	**H**igh **E**elctron **M**obility **T**ransistor
FET	**F**ield **E**ffect **T**ransistor
MOSFET	**M**etal **O**xide **S**emiconductor **F**ield **E**ffect **T**ransistor
MBE	**M**olecular **B**eam **E**pitaxially
MOCVD	**M**etal-**O**rganic **C**hemical **V**apor **D**eposition

Physical Constants

Electron charge	e	$=$	$1.602\ 177\ 33 \cdot 10^{-19} C$
Permittivity of vacuum	ϵ_0	$=$	$8.854\ 187\ 817 \cdot 10^{-12} C^2/J \cdot m$
Boltzmann constant	K_B	$=$	$1.380\ 658 \cdot 10^{-23} J/K - 8.617\ 385 \cdot 10^{-5} eV/K$
Plank constant	h	$=$	$6.626\ 075\ 5 \cdot 10^{-34} J \cdot s$
reduced Plank constant	$\hbar$	$=$	$1.054\ 571\ 68 \cdot 10^{-34} J \cdot s$

Chapter 1

Introduction

[1] Transistor was born in America in the end of 1947, its discovered it's due to a long research took place in the *Bell Laboratories* by *Shockley, Bardeen e Brattain.* For this result they got the Nobel prize on 1956. The history of this device started in the years just before the Second World War, when some researchers, studying the characteristics of silicon, they discovered the existence of two different kind of semiconductors, the N type and the P type, depending on the impurities contained in the crystal lattice. It was suddenly understood that this study would have had success.

Nowadays the invention of the transistor has changed our life. It's sufficient think about how this component and its successor, the *MOSFET*, are widely used in different fields of industry, starting from the microelectronics which allowed the development of the computers, passing through the power electronics that become important with the railway diffusion and with the expansion of the electrical engine, end ending with the telecommunication field thanks to witch the electronic market grew in the last years.

[2] Since 1947 to date electronics has been renewed. During this process have changed not only the production methods but also the materials used. Among the materials, the one that still now is the most used is Silicon, the second material most present in the Earth. Recently, especially for high-tech applications and for optoelectronic fields, they are developing *compound semiconductors*, including the ones belonging to II-IV group, i.e. CdTe, *ZnSe*, e,..., or the ones that are part of the III-V group, i.e. *GaAs*, *GaN*,... or of the IV group, i.e. *SiC*, *SiGe*. Starting from these elements we can obtain further compound materials, i.e. *ternary semiconductors*, realized by the combination of two binary semiconductors with which we can get *AlGaN*, *GaInAs*, *AlGaAs*,... The tendency of using new compound material has done because of the better characteristics of these materials than the silicon. For example the electron mobility of the *GaAs* is 6 times

more then that of silicon and the critical electric field of GaN is 10 times more than that of silicon.

In 1968, Maruska and Tietjen were the first to try the *hydride vapour phase epitaxy* (HVPE) approach to grow centimeter-sized GaN layers on sapphire substrates. Sapphire was chosen as substrate material because it is a robust material that is not reactive with the ammonia used during the production and because it is cheaper than the other material used as a substrate: *SiC*. However, these films were all polycrystalline. In 1969, Maruska realized that in an ammonia environment at temperatures above 600^oC GaN growth actually would occur instead of decomposition. He increased the growth temperature to 850^oC, the temperature typically used for gallium arsenide ($GaAs$), and obtained the first single crystalline GaN film.

All GaN films grown at that time showed very high electron concentrations ($10^{20}cm^{-3}$) even without intentional doping. The responsible n-type donors were believed to be nitrogen vacancies (V_N), a concept that has caused a lot of controversy over the years. Eventually oxygen (O_2) has been proposed as the responsible donor. Oxygen with its six valence electrons on an N site (N has five valence electrons) would be a single donor. A suitable p-type dopant had however to be found. Zinc (*Zn*) seemed to be an appropriate acceptor as it worked for $GaAs$ and gallium phosphide (GaP). Although heavy *Zn* concentrations rendered GaN films to be insulating, the films never became conducting p-type. In 1972, Maruska was the first to propose magnesium (*Mg*) to be a better choice of p-type dopant than *Zn*.

In the late 1970s, GaN research ceased virtually everywhere because of the continuing difficulties encountered with the growth of high quality films needed for device development. Remaining issues were the choice and availability of a suitable substrate, how to control the very high intrinsic n-type conductivity, and difficulties with obtaining conducting p-type GaN films. In 1982 only a handful of papers were published world-wide on this material system.

It was the perseverance of Isamu Akasaki that eventually resulted in obtaining conducting p-type GaN films in 1989. The conducting p-type films were discovered during cathodoluminescence (CL) observations of *GaN:Mg* in a *scanning electron microscope* (SEM). The explanation for this phenomenon was given by Van Vechten et al. in 1992 who proposed that the shallow acceptor level of *Mg* was compensated by a hydrogen atom complexing with the *Mg* acceptor. This *Mg:H* complex passivates the acceptor and prohibits p-type conduction. The energy of the electron beam breaks up this complex and enables *Mg* to be a shallow acceptor approximately $0.16eV$ above the valence band.

In 1986, a milestone was achieved when Amano et al. reported highly improved surface morphology, and optical and electrical properties of GaN films grown by *metal organic chemical vapour deposition* (MOCVD) on sapphire substrates through the use of a low-temperature (600^oC) aluminium nitride (AlN) nucleation layer. This layer is grown between the sapphire substrate and the bulk GaN film in order to prevent the formation of defects because of the large lattice mismatch between the low-temperature AlN nucleation layer and the following GaN film. To date, MOCVD is the workhorse for the growth of GaN and related materials.

The breakthroughs achieved have lead to the revival of the GaN material system in the early 1990s. Researchers in the fields of optical and microelectronic applications showed renewed interest in GaN because the great potential of this material predicted performance enhancement over the existing semiconductors (Si, $GaAs$). In 1991, Khan et al. reported first evidence for *two-dimensional electron gas* (2DEG) formation at an $Al_xGa_{1-x}N/GaN$ heterojunction grown by MOCVD on sapphire. The first GaN metal semiconductor field-effect transistor (MESFET) and heterostructure field-effect transistor (HFET) grown by MOCVD on sapphire substrates were reported in 1993 and 1994, respectively by Khan et al. In 1993, Nakamura et al. demonstrated the first high-brightness blue double-heterostructure GaN LEDs. In 1996, Nakamura et al. reported the first continuous wave blue GaN LD.

Since these giant steps in material and device development, both research and commercial GaN activities have gained enormous attention. GaN-based optical applications have first reached the stage of commercialization while microwave high-power electronics are on the verge of their commercial breakthrough. Producibility, reproducibility and reliability of the epitaxial material and process technologies are key issues that need to be addressed to redeem the great promises GaN-based devices hold.

1.1 Thesis organization

This work is divided in 4 chapters, in the first one there is the introduction with the history of the GaN material.

In the second chapter I will present the most used *wide band gap* (WBG) materials, i.e. GaN, $AlGaN$, AlN, SiC, suitable for the realization of *high electron mobility transistors* (HEMTs), and I will explain the properties which make these materials so suitable for high voltage and high frequency applications as well as LED ones. In particular I will focus on the 2DEG formations at the $AlGaN/GaN$ interface and on the traps effects as well, including the *current collapse* mechanism. Indeed, being a new technology,

WBG semiconductors suffer of traps effects because the growth process has not still been perfected, so a large amount of defects is present within the structure. It the end there will be a summary of the most likely scopes of these materials.

In the third chapter I will start to explain my simulation activity starting from the DC simulations, both $IdVg$ and $IdVd$ characteristics, of two devices, one without Field Plate and one with it. Beside the simulations we used experimental data provided by NXP in order to match the input and output characteristics. After that I will move to AC simulations of a device with Field Plate which is a feature by means of which the electric field can be spread along the device, avoiding dangerous hot spot and then improving the device reliability. AC simulations are important whether it wants to get informations about the gate capacitance and hence about the time response of the device an about the capacitive load effect that this device could have on its driver. Always in the third chapter I will present some simulation results with the aim to check if the presence of traps under the contact gate could cause the leakage that heavily afflicts this kind of devices. In the last part of the chapter I'm going to show the results obtained about the electric field evaluation within the device with different Field Plate lengths, with the purpose to see its effect.

At the tail will follow the summary and the conclusions.

Chapter 2

Wide band gap materials

[3] Wide band gap (WBG) materials have attracted a lot of attention in the last 10 years due to their use in optoelectronic and electronic applications. The reasons of this interest are the different material properties respect to silicon, the most used material in electronics. III-V compound semiconductors are typically grown with a wurtzite structure and have a bandgap range from $1.0eV$ to $6.0eV$. This very large band gap is useful for short wave length light emitting diodes and for high power electronics, field where high breakdown voltage and resistance to high temperature are needed. WBG semiconductors are also used in radio frequency (RF) applications because of their fast carrier transport due to high intrinsic electron concentration, called (2DEG).

In this chapter we will discover the material properties of the most used WBG materials, such as GaN, AlN, SiC, comparing them with those of the common semiconductors, like Si and GaAs, in addition at the description of their application fields. Afterwards I will present the explanation for the 2DEG formation in the polar materials used to build the HEMT device as well as the traps effects, a big issue for these kind of materials.

2.1 Materials properties

[2] A large bandgap energy (Eg) results in high electric breakdown field (Ec), witch enable the application in high supply voltage and allows the material to sustain high operating temperature. As it can see in table 2.1, the critical field value for the wide band gap materials, such as SiC and GaN, is an order of magnitude higher than those of conventional semiconductors (Si, $GaAs$, InP, ...). This large band gap affects also the intrinsic carrier concentration. In electronic devices, where current has to be modulated by some means, the concentration of intrinsic carriers is fixed by the temperature and

therefore is detrimental to device performance. When the intrinsic carrier concentration increases to $10^{15}cm^{-3}$, the material becomes unsuitable for electronic devices, due to the high leakage current arising from the intrinsic carriers. A growing interest in high bandgap semiconductors is partly due to the potential applications of these materials for high-temperature devices where, due to their larger gap, the intrinsic carrier concentration remains low up to very high temperatures. This behaviour can be seen in fig 2.1, in which is presented the intrinsic electron concentration of various semiconductors as a function of the temperature.

Property	***GaN***	**AlN**	**InN**	**SiC**	**Si**	**GaAs**
Band Gap (Eg) $[eV]$	3.44	6.2	1.	3.26	1.12	1.43
Electric break down field (Ec) $[MV/cm]$	3.0	1.4 - 1.8	3.0	0.3	0.4	0.5
Saturated electron velocity (v_{sat}) $[\text{x}10^7 cm/s]$	2.5	1.7	4.5	2.0	1.0	1.0
Electron mobility (μ_n) $[cm^2/V \cdot s]$	900 (bulk) 2000 (2DEG)	135	3200	700	1500	8500
Electron effective mass (m_c) $[m_0]$	0.22	0.4	0.11	0.2	1.18	0.63
Hole effective mass (m_v) $[m_0]$	0.8	3.53	0.27	1.0	0.55	0.52
Lattice constant $[\AA]$	3.175	3.111	3.533	3.073	5.431	5.653

Table 2.1: Material properties of conventional and wide-bandgap semiconductors at 300K

2.1.1 Gallium Nitride (GaN)

[2] Gallium Nitride is the basic material in the III-N class of compounds. It's typically used in the fields where fast carrier transport and high breakdown voltage are required. *GaN* is used as a channel material in various FETs and HEMTs devices.

A primary disadvantage of fabricating transistors from bulk *GaN* and *SiC* is the relatively low values for the electron mobilities (μ_n), which is $900cm^2/Vs$ for *GaN* and approximately $700cm^2/Vs$ for *SiC*. As comparison *GaAs* presents a very high electron mobility ($8500cm^2/Vs$), that's why *GaAs* is widely used to fabricate field-effect transistors (FET). In general, WBG semiconductors have relatively low mobility but very high values for the saturation velocity, which is reached at high electric fields that can easily be supported. Indeed, the huge success of III-N materials is not mainly due to the intrinsic material transport properties, but due to interface properties. In case of III-N heterostructure, the interface allows the formation of n-channel, called *two dimensional electron gas* (2DEG), at the $Al_xGa_{1-x}N/GaN$ interface. This electron gas intrinsically provide extremely high carrier concentrations without further impurity doping. The

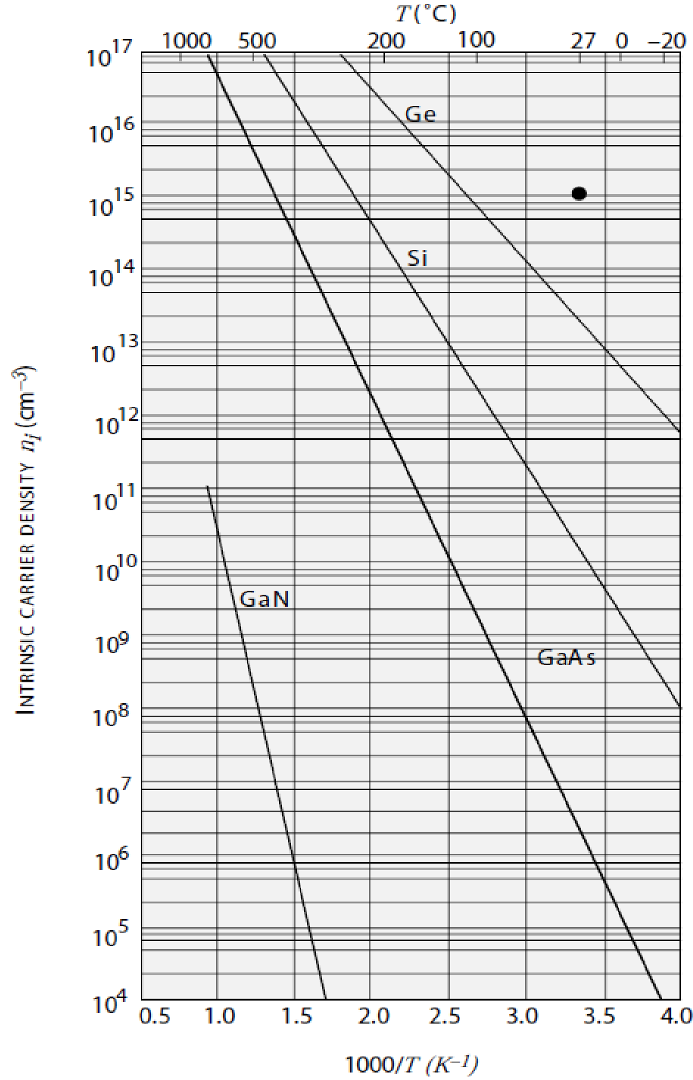

FIGURE 2.1: Intrinsic electron concentration of various semiconductors, GaN included, respect to the temperature.

mobility and saturation velocity of the 2DEG at the heterojunction is very suitable for high-power, high-frequency device applications. The room temperature mobility of the 2DEG, which is typically between $1200cm^2/Vs$ and $2000cm^2/Vs$, is significantly better than that of bulk *GaN* and *SiC*. The 2DEG sheet charge density (n_s) of the $Al_xGa_{1-x}N/GaN$ structure is very high (experimental values up to $10^{13}cm^{-2}$) due to *piezoelectric* and *spontaneous polarization* induced effects. The measured sheet charge density is about a factor of 10 better than those of $Al_xGa_{1-x}As/In_xGa_{1-x}As$ and $In_xAl_{1-x}As/In_xGa_{1-x}As$ heterostructure.

The thermal conductivity (κ) (tab. 2.2) of a semiconductor material is extremely important since this parameter is a measure of the easiness with which dissipated power can be extracted from the device. Poor thermal conductivity leads to degraded device operation at elevated temperatures. In general, conventional semiconductors are poor

thermal conductors, particularly $GaAs$ and InP. Conversely, SiC is an excellent thermal conductor, making a good choice for GaN growth. Beside the thermal conductivity, the lattice constant of these two materials are quite similar, so GaN can be grown on SiC without creating many defects.

Property	**GaN**	**AlN**	**InN**	**SiC**	**Si**	**GaAs**
Thermal conductivity (κ) $[W/cm \cdot K]$	1.3-2.1	2.85	0.45	3.7-4.5	1.5	0.5

Table 2.2: Thermal conductivity of III-N semiconductors and other materials at 300K

The relative permittivity (ϵ_r) (tab. 2.3) is an indication of the capacitive loading of a transistor and affects the device terminal impedances. The table below shows that the permittivity values for the WBG semiconductors are considerably lower than those for the conventional semiconductors. This permits for example a GaN device to be about 20% larger in area for a given impedance. As a consequence, this increased area enables the generation of larger currents and higher microwave output power.

Property	**GaN**	**AlN**	**InN**	**SiC**	**Si**	**GaAs**
Relative permittivity (ϵ_r)	9.0	9.14	15.3	10.1	11.8	12.8

Table 2.3: Relative permittivity of III-N semiconductors and other materials at 300K

For high-power/high-frequency applications there are several drawbacks. Among them are high substrate costs and low thermal conductivity. The latter makes it very difficult to effectively remove heat when used in high-power applications. Hence, not only for these reasons it's mandatory to have an high quality materials, in order to avoid ruptures that can be originated along the structural defects.

Important for the growth is the *coefficient of thermal expansion* (CTE). In the table 2.4 there is a comparison between CTE values of GaN, AlN and of different kind of substrate. As it can see GaN and AlN can be grown well onto SiC due to the comparable value of CTE. For the *Sapphire* and *Si* the difference is quite marked and the quality of the material grown will be not so good.

Property	**GaN**	**AlN**	**SiC**	**Si**	**Sapphire**
α $[10^{-6}K^{-1}]$	3.1	2.9	3.2	2.6	4.3

Table 2.4: Coefficients of thermal expansion (CTE) of III-N semiconductors and other materials at 300K

2.1.2 Aluminium Nitride (*AlN*)

[4] Second to GaN, AlN in the most important binary material in III-N material family for electronics applications and is mostly used in its ternary compound $Al_xGa_{1-x}N$,

for instance for create a barrier heterostructure. It is characterized to be an insulator due to the high band-gap energy, about $6.2eV$ at ambient temperature, and the high activation energy of donors. *AlN* is used as nucleation layer to start the growth on *SiC* or on *Sapphire* substrates. As depicted in table 2.4 thermal expansion of *AlN* is similar to those of *GaN*, moreover the intrinsic thermal conductivity is very high, even better than that of the other semiconductors, apart from the one of *BN*, *SiC* and *diamond*. [5] *AlN* nucleation layer has another function, it limits the breakdown voltage (BV) of the *GaN* buffer layer. It has been shown that BVs of the fabricated devices strongly depended on the thickness of the *AlN* nucleation layer. These characteristics make *AlN* a potentially attractive substrate material.

The high band gap of this material allows the band gap of *AlGaN* to be modified in a broad band from the value of *GaN* to that of *AlN*. With *InN*, instead of *GaN*, the band gap range of *InAlN* material can be even wider.

The electron transport in wurtzite AlN has been investigated by *Monte Carlo* (MC) simulations. The electronic characteristics are the large band gap and the relatively high-effective electron mass (m_c) of 0.48. These values lead a low field mobility of $135cm^2V^{-1}s^{-1}$ at room temperature, a very high critical field of $450kVcm^{-1}$ and a saturation velocity of $1.4 \cdot 10^{17}cm^{-3}$.

2.1.3 Indium Nitride *(InN)*

[4] *InN* and its compounds $In_xAl_{1-x}N$ and $In_xGa_{1-x}N$ are not yet widely used in electronic devices. The indium content is low to achieve the lattice matching to *GaN* buffer layer. The MOCVD growth technique of InN is complicated caused by the high temperature required and MBE method causes high amount of defects in the structure, due to the nitrogen vacancies. The MBE growth is under development and allows improved material quality and thus the use of the full range of material composition in the material $In_xGa_{1-x}N$. High quality *AlN* has been grown by MBE and a bulk electron mobility of $3.570cm^2V^{-1}s^{-1}$ at $300K$ is obtained. The thermal expansion coefficient and the lattice constant suggests the growth on sapphire substrate.

Due to the new research on samples with improved material quality, the band gap and the optical functions of *InN* are reconsidered. This fact had a dramatic impact on the calculations of the transport properties. Further MC calculations on the wurtzite material give a carrier velocity of up to $4.2 \cdot 10^7 cm \cdot s^{-1}$ at a critical field of $52 - 65KVcm^{-1}$. These properties are promising, however, compared to *GaAs* or *InGaAs* materials, they are not really surprising when considering the low effective mass, the low bandgap and maximum electron velocity. *InN* has a very low bandgap energy of $0.77eV$,

different respect the level found in the beginning, $1.89eV$. This discrepancy is explained by the existence of oxy-nitrides witch have a larger bandgap. Optically it means that a very broad range of wave length is available in the III-N compound materials, ranging from deep ultraviolet to red region.

2.1.4 Aluminium Gallium Nitride ($Al_xGa_{1-x}N$)

[4] $Al_xGa_{1-x}N$ is the most important ternary compound, as the lattice mismatch relative to GaN can be controlled for nearly all material compositions. The material properties of AlGaN ($P_{A_xB_{1-x}N}$) can be derived starting from those of GaN (P_{BN}) and AlN (P_{AN}) following the formula (2.1), called Vegard's law:

$$P_{A_xB_{1-x}N} = x \cdot P_{AN} + (1-x) \cdot P_{BN} \tag{2.1}$$

In this way It can obtain information about energy gap, dielectric constant, lattice constant and for other important electronics values. Varying the aluminium fraction (x) the band gap and other physical parameters can be tailored as needed from the one of *GaN* to the one of *AlN*, allowing for example the realization of a more efficient barriers for power electronic and optoelectronic applications.

2.1.5 Indium Gallium Nitride ($In_xGa_{1-x}N$) and Indium Aluminium Nitride ($In_xAl_{1-x}N$)

[4] The importance of *InN* and its ternary compounds is due to the smaller band gap relative to *GaN*, allowing for a broader variety of layers for band gap engineering also into the visible optical range in optoelectronic devices. High quality $In_xGa_{1-x}N$ layers were recently grown by MBE, mostly on sapphire substrate. $In_xAl_{1-x}N$ is lattice-matched to GaN for $x = 0.17$, witch has recently grown attention to this material for HEMT device applications. Good quality films , especially for high *In* contents, have not been realized with MOCVD growth. MBE has instead allowed this goal.

2.2 Substrate

[4] The reasons followed for the substrate choose are:

- Lattice mismatch relative to the materials;

- Thermal conductivity and coefficient of thermal expansion;
- Maximum electrical isolation;
- Price and price per area;
- Availability with respect to the diameter;
- Crystal quality and residual defect density;
- Surface properties and residual defect density;
- Wafer warp and wafer bowing;
- Mechanical and chemical properties with respect to thinning and viahole etching.

In this section I'm going to present the most used substrate that are suitable for *GaN* growth: sapphire, *SiC* and *Si*. Moreover a discussion about *AlN* substrate is presented.

2.2.1 Sapphire substrate

[2] *Sapphire* is the most commonly used substrate for *GaN* heteroepitaxy. Sapphire is an interesting choice because it is semi-insulating (s.i.), it can withstand the required high growth temperatures, and it is relatively cheap ($100 for a 2 inch wafer). However, its very low thermal conductivity ($0.47W/cmK$ at $300K$), large lattice mismatch (13%), and large thermal expansion coefficient (TEC) mismatch (34%) with the *GaN* epilayers makes it the worst choice for high-power applications. Nevertheless, the power results for *GaN* HFETs on sapphire substrates are astonishing and are more than 10 times higher than those which can be achieved by *GaAs* HFETs. The state-of-the-art values for output power density of small gate periphery devices (typical total gate widths of $100-250m$) with conventional T-shaped sub micron gates are about $6.5W/mm$ at $8GHz$ and $3.3W/mm$ at $18GHz$. However, using a *field plate* (FP), which is an extension of the top of a conventional T-gate towards the drain contact, has overwhelmingly increased the power density of small devices to $12W/mm$ at $4GHz$.

2.2.2 SiC substrate

[2] The high thermal conductivity ($3.7-4.5W/cmK$ at $300K$), low lattice mismatch (3.4%), and relatively low TEC mismatch (25%) are the main reasons for the superior material quality of *GaN* epilayers grown on semi insulating *SiC* compared to those grown on sapphire. [4] Other characteristics are a good isolation levels (beyond $10^9\Omega \cdot cm$) and the availability in $4-6in.$ diameters. As a consequence, the 2DEG transport properties

of GaN epilayers on SiC are much better and it is very clear that at the moment s.i. SiC is the substrate of choice for GaN microwave high-power applications. For small periphery devices with conventional gates state-of-the-art values for output power density are $10 - 12W/mm$ at X-band ($8.0 - 12.4GHz$). For small devices with a FP gate, record output power densities of over $30W/mm$ at $4 - 8GHz$ have been reported.

2.2.3 Si substrate

[2] Despite the very large lattice mismatch (17%) and enormous TEC mismatch (56%), the advantages of low substrate cost, excellent availability of large substrate diameters, acceptable thermal conductivity ($1.5W/cmKat300K$), and integration possibilities with Si electronics make this material interesting candidates for GaN hetero-epitaxy. In addition low isolation ($10 - 30K\Omega \cdot cm$) is provided by this material, giving high power losses. Although the epitaxial growth process of GaN on Si differs considerably from the ones on sapphire and s.i. SiC, the current state-of-the-art transistor results level those obtained on sapphire and even those on s.i. SiC [4] Many engineering challenges needs to be done in order to obtain a competitive Si substrate. Nevertheless many epitaxial procedures have been developed through witch the silicon substrates demonstrated very good performances.

2.2.4 AlN substrate

[4] Native AlN substrates have been only recently developed because of the possibles improvements achieved by the almost zero lattice mismatch. AlN itself is highly resistive ($> 10^{12}\Omega \cdot cm$), the thermal conductibility is very good, similar to SiC, the lattice mismatch is the lowest among the other substrates considered (1%). The drawbacks are the limited diameter and the high price.

2.3 Applications

[2] The direct bandgap of GaN and its alloys enables the material to be used for both optical and electronic applications. At 300 K the bandgap of GaN is $3.44eV$ which corresponds to a wavelength in the near ultra violet (UV) region of the optical spectrum. Figure 2.2 shows a plot of the bandgap energy versus lattice constant in combination with the visible optical spectrum for various semiconductors including the wide-bandgap materials such as SiC, GaN, AlN and other materials. It can be seen that the

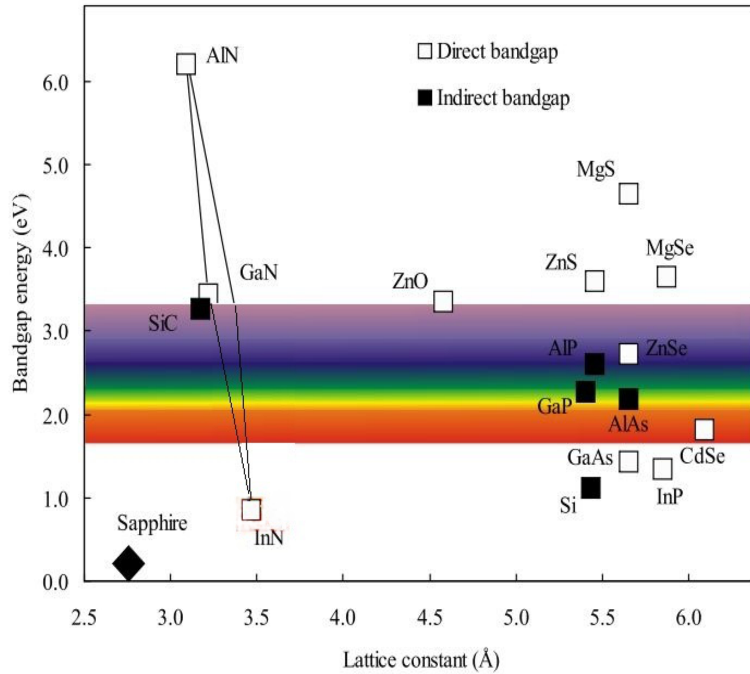

FIGURE 2.2: Bandgap energy and visible spectrum versus lattice constant for various semiconductors, including wide band gap materials.

$Al_xIn_yGa_{1-x-y}N$ alloys cover bandgap energies from $1.9eV$ to $6.2eV$, which correspond to wavelengths ranging from red to deep UV.

2.3.1 Optical applications

Among the optical applications it can be counted LEDs and LASERs, devices that recently became very popular thanks to the improvements of the reliability and of the efficiency and due to their price decreasing. For these reasons the LED and LASER market grew quickly during the last years. Indeed [6] the LED market reached $4.2 billion in 2006 and is set to emerge from its current state of low growth, according to Strategies Unlimited. Emerging applications including illumination will drive the market towards $9 billion by 2011. [7] For the LASERs is expected an annual growth rate of 9%, according to US-based market analyst Strategies Unlimited.

2.3.1.1 LED

[2] The main economical benefits of LED-based lighting are low power requirement, high efficiency, and long lifetime. In addition, solid state design render LEDs impervious to electrical and mechanical shock, vibration, frequent switching and environmental extremes. Automotive exterior lighting has been moving rapidly to incorporate

transparent-substrate $Al_xIn_yGa_{1-x-y}P$ technology. Full-motion video displays are using $Al_xIn_yGa_{1-x-y}N$ and $Al_xIn_yGa_{1-x-y}P$ technologies and will continue to proliferate as the costs are reduced. Traffic-signal applications have begun to incorporate red $AlInGaP$ and $AlGaAs$ LEDs for traffic lights and are moving toward incorporating amber and blue-green LEDs to produce a completely LED-based signal head. By using multiple LEDs, a LED cluster lamp continues to provide light even if one or more emitters fail unlike when the filament breaks in an incandescent bulb. Other important GaN-based LED applications are back lighting (cell phones, laptops, ...), white light (flash lights, car head lights), general lighting (interior and exterior), water purification systems, and medical (sensors, surgical goggles). A full colour image can be created combining red, green, and blue pixels in the display. Red and green LEDs were available using gallium arsenide phosphide ($GaAs_{1-x}P_x$) and gallium phosphide nitride ($GaP{:}N$) materials, respectively. All that was missing to realize a flat LED-based television set was a bright blue LED. These devices became available using either SiC or II-VI compounds such as zinc oxide (ZnO). However, because of their indirect bandgap SiC LEDs were not very efficient. The devices based on II-VI compounds mainly suffered from much too short lifetimes for commercial applications. Hence these devices could not be used in the envisioned display applications.

2.3.1.2 LASER

[2] Infra-red $AlGaAs$-based and red $AlInGaP$-based laser diodes (LDs), such as those in today's CD and DVD systems, have been around for decades. To increase the storage capacity on a CD, the pit size must be made smaller. A shorter wavelength LD is required to focus onto the smaller pit size. The current generation of DVD systems uses a LD with an emission wavelength of $650nm$. In the last few years the market for DVD systems has increased rapidly. However, the majority of these systems is read-only and is based on a $5mW$ $AlInGaP$ LD emitting at $650nm$. For further advances in the market recordable DVD was an obvious necessity. This required higher output power from the $650nm$ LD (typically $30-40mW$). To also achieve faster read/write speeds even higher powers are required. GaN-based blue-violet LDs with an emission wavelength of $405nm$ will be the cornerstone of next-generation DVD player-recorders and optical high-density data-storage systems for computers. Using these components it is already possible to write huge amounts of data ($27GB$) on a single-layer $12cm$ DVD disk which is almost six times the storage capacity possible with ordinary red LDs. This is enough to store more than two hours of high-definition (HD) video or 13 hours of standard-definition (SD) video.

2.3.2 Electronic applications

[2] *GaN* is an excellent option for high-power/high-temperature microwave applications because of its high electric breakdown field and hence the high electron saturation velocity. High BV is a result of the wide bandgap and enables the application of high supply voltages, which is one of the two requirements for high-power device performance. In addition, the wide bandgap allows the material to withstand high operating temperatures ($300^oC - 500^oC$).

A big advantage of *GaN* over *SiC* is the possibility to grow heterostructures, e.g. *AlGaN/GaN*. The resulting two-dimensional electron gas (2DEG) at this heterojunction serves as the conductive channel. Large drain currents ($> 1A/mm$), which are the second requirement for a power device, can be achieved because of the high electron sheet densities ($10^{13}cm^{-2}$) and mobilities ($1500 - 2000cm^2/V \cdot s$). These material properties clearly indicate why *GaN* is a serious candidate for next-generation microwave high-power/high-temperature applications.

2.3.3 Military applications

[2] Research programs have focused on achieving hero values with respect to current densities and output power densities at microwave frequencies in order to prove the high expectations. The new programs however start for the basics (material growth, etching, contacts) and move through the stage of discrete devices to the eventual goal of *GaN*-based microwave monolithic integrated circuits (MMICs). The focus now is on understanding the physical reasons behind device failures and the development of physical models to predict performance in order to increase reproducibility and reliability. In general, defence research programs focus on the development of *GaN* technology for use in components such as surface radars, broadband seekers, jammers, battlefield communication, satellite communication links, transmit/receive modules, broadband high-power amplifiers (HPAs), and low noise amplifiers (LNAs). The frequencies of interest for these applications range from $2GHz - 40GHz$.

2.3.4 Commercial Applications

[2] Commercial *GaN*-based applications are on the verge of their breakthrough. The first products will most probably be high-efficiency and high-linearity power amplifiers for base-stations, which power 3G wireless broadband cellular networks in the so-called S-band ($2GHz - 4GHz$). Other high-volume commercial applications in which *GaN*-based electronics could lead to significant performance enhancement and cost reduction

are high-frequency MMICs (wireless broadband communication links), hybrid electric vehicles (DC-AC conversion), high-temperature electronics (automotive, energy production), switches (plasma display panels, low-frequency high-power switching), high-voltage power rectifiers (inverter modules), micro electro mechanical systems, MEMS (pressure sensors), and Hall sensors (automotive applications).

Most of the high-power devices it uses silicon insulated gate bipolar transistors (IGBTs) for the primary switching element, with Si p-i-n diodes as the fly-back diode, configured in a module designed to control three-phase motors. However, like all silicon devices they are limited to junction temperatures of $150^oC - 175^oC$. Controlling the junction temperature of the Si electronics requires large heat sinks and liquid cooling, but both these solutions are costly and difficult to integrate.

Besides the great opportunities that GaN-based high-temperature electronics present to HEVs, they also offer important capabilities to aerospace, energy production, and other industrial systems that will affect modern everyday life. The inherent ability of a GaN junction to properly rectify with low reverse leakage current at junction temperatures as high as 600^oC enables power-device operation at higher ambient temperatures. In addition, superior power switching properties of WBG devices are also present at room temperature ambient. GaN is going to play a critical role in realizing high-power electronics beyond the capability of Si at all temperatures.

2.4 Semiconductor physics

[3] Semiconductors such as GaN, In, and AlN are called *polar materials* since they can have net polarization due to a shift in the cation and anion sublattices. In unstrained zinc-blende structures the cation and anion sublattices are arranged in such a way that there is no net polarization in the material. However, in the wurtzite crystal (like InN, GaN, AlN) the arrangement of the cation and anion sublattices can be such that there is a relative movement from the ideal wurtzite position to produce a *spontaneous polarization* in the crystal which becomes very important for heterostructures.

In addition to spontaneous polarization is another phenomena which can lead to polarization in the material: *piezoelectric polarization*. Strain can cause a relative shift between the cation and anion sublattices and hence create net polarization in the material.

[8] These very high polarizations and resulting electric fields produce high interface charge densities at group-III-nitride interfaces and spatial separation of the hole and electron wave functions in GaN-based quantum well structures.

2.4.1 Spontaneous and piezoelectric polarization

[2] The group III-nitrides *AlN*, *GaN*, and *InN* can crystallize in the following three crystal structures: wurtzite, zinc-blende, and rock-salt. However, at ambient conditions the wurtzite structure is the thermodynamically stable phase, consisting of two inter penetrating hexagonal close packed lattices, which are shifted respect to each other ideally by $3/8 \cdot c0$, where $c0$ is the height of the hexagonal lattice cell as shown in 2.3

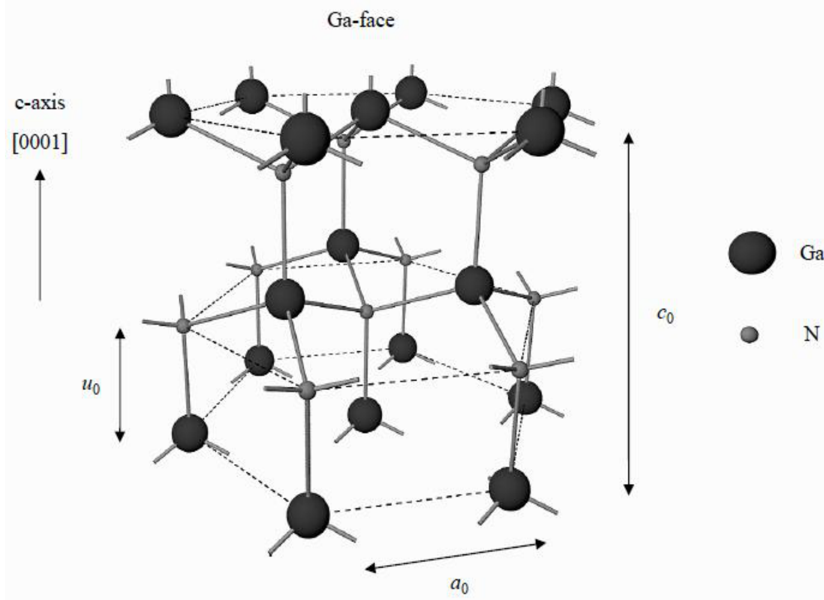

FIGURE 2.3: Wurtzite crystal structure unit cell of GaN material

The chemical bonds of III-nitride compounds such as *GaN* are predominantly covalent with a tetrahedral structure, which means that each atom is bonded to four atoms of the other type. Because of the large difference in electronegativity of *Ga* and *N* atoms, there is a significant ionic contribution to the bond which determines the stability of the respective structural phase. The electrons involved in the metal-nitrogen covalent bond will be strongly attracted by the Coulomb potential of the *N* atomic nucleus, more electronegative respect to *GaN* ones. This means that this covalent bond will have stronger ionicity compared to other III-V covalent bonds. This ionicity, which is a microscopic polarization, will result in a macroscopic polarization if the crystal lacks inversion symmetry. Although this effect also exists in the [111] direction of zinc-blende crystals such as *GaAs* and *InP*, it is much less pronounced because of the smaller ionicity of the covalent bond. Since this polarization effect occurs in the equilibrium lattice of III-nitrides at zero strain, it is called *spontaneous polarization.*

[8] Wurtzite *GaN* crystals have two distinct faces, commonly known as *Ga*-face and *N*-face, which correspond to the [0001] and $[000\overline{1}]$ crystalline faces. In fig 2.3 is depicted the *Ga*-face, instead the *N*-face material can be obtained by flipping the *Ga*-face material

upside-down. In the case of heteroepitaxial growth of thin films, the polarity of the material cannot be predicted in a straightforward way, and must be determined by experiments.

[2] It has to be noted that for *Ga*-face material the N atom is stacked directly over the *Ga* atom and vice versa for *N*-face. Figure 2.3 also shows the three parameters that define the wurtzite lattice. These are the edge length of the basal hexagon (a_0), the height of the hexagonal lattice cell (c_0), and the cation-anion bond length ratio (u_0) along the [0001] direction. The subscript '0' indicates that these values are those of the equilibrium lattice.

In table 2.5 are showed the parameters of the most used III-N semiconductors.

parameter	**AlN**	**GaN**	**InN**
$a_0[\AA]$	3.112	3.189	3.54
$c_0[\AA]$	4.982	5.185	5.705
$u_0[c_0]$	0.380	0.376	0.377

Table 2.5: Lattice parameters of wurtzite III-nitrides at 300 K

In addition to the ionicity of the covalent bond, the degree of non-ideality of the crystal lattice also affects the strength of spontaneous polarization. In III-nitrides, although the covalent bond parallel to the c-axis is strongly ionic and is primarily responsible for the spontaneous polarization, the other three covalent bonds in the tetrahedral structure are also equally ionic. The resultant polarization from these other three bonds is actually aligned in the opposite direction and serves to counteract the polarization of the other bond. As the c_0/a_0 ratio decreases, c_0 decreases and a_0 increases, these three covalent bonds will be at a wider angle from the c axis and their resultant compensation polarization will decrease. As a result the macroscopic spontaneous polarization will increase. Table 2.6 shows the c_0/a_0 ratio and the spontaneous polarization for *AlN*, *GaN*, and *InN*. It can be seen that as the lattice non-ideality increases, c_0/a_0 ratio moves away from 1.633 of the ideal lattice, the value of spontaneous polarization (P_{SP}) increases from *GaN* to *InN* to *AlN*.

parameter	**AlN**	**GaN**	**InN**
c_0/a_0	1.6010	1.6259	1.6116
$P_{SP}[C/m^2]$	-0.081	-0.029	-0.032
$C_{13}[GPa]$	108	103	121
$C_{33}[GPa]$	373	405	182
$e_{33}[C/m^2]$	1.46	0.73	0.97
$e_{31}[C/m^2]$	-0.60	-0.49	-0.57

Table 2.6: Influence of lattice non-ideality on the value of spontaneous polarization, elastic and piezoelectric constants value for wurtzite structure of III-nitrides materials

If the ideality of the III-nitride lattices is changed externally, then due to the strong ionicity of the metal-nitrogen covalent bond there will be large changes in the polarization of the crystal. One way to change the ideality of the crystal lattice is through strain. If stress is applied to the III-nitride lattice, the ideal lattice parameters c_0 and a_0 of the crystal structure will change to accommodate the stress. Hence, the polarization strength will be changed. This additional polarization in strained III-nitride crystals is called *piezoelectric polarization.*

[8] The spontaneous polarization along the c-axis of the wurtzite crystal is $P_{SP} = P_{SPz}$.

The piezoelectric polarization can be calculated with the piezoelectric coefficients e_{33} and e_{13} (in table 2.6) as:

$$P_{PE} = e_{33}\epsilon_z + e_{31}(\epsilon_x + \epsilon_y) \tag{2.2}$$

where ϵ_z is the strain along the c-axis, ϵ_x and ϵ_y indicate the in-plane strain:

$$\epsilon_z = \frac{c - c_0}{c_0} \tag{2.3}$$

$$\epsilon_x = \epsilon_y = \frac{a - a_0}{a_0} \tag{2.4}$$

The relation between the lattice constants of the hexagonal GaN is given to

$$\frac{c - c_0}{c_0} = -2\frac{C_{13}}{C_{33}}\frac{a - a_0}{a_0} \tag{2.5}$$

where C_{13} and C_{33} are elastic constants (in table 2.6).

Using equations 2.2 and 2.5, the amount of the piezoelectric polarization in the direction of the c-axis can be determined by

$$P_{PE} = 2\frac{a - a_0}{a_0}\left(e_{31} - e_{33}\frac{C_{13}}{C_{33}}\right) \tag{2.6}$$

Since $[e_{31} - e_{33}(C_{13}/C_{33})] < 0$ for *AlGaN* over the whole range of compositions, the piezoelectric polarization is negative for tensile and positive for compressive strained barriers, respectively. The spontaneous polarization for *GaN* and *AlN* was found to be negative, meaning that for *Ga(Al)*-face heterostructures the spontaneous polarization is pointing towards the substrate, as depicted in figure 2.4.

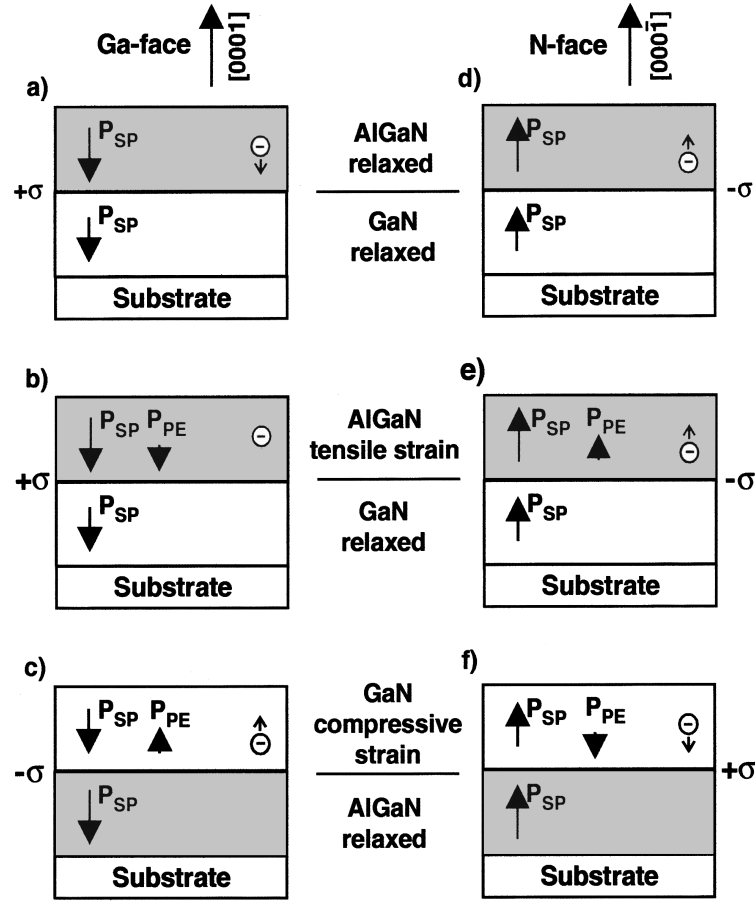

FIGURE 2.4: Polarization induced sheet charge density and directions of the spontaneous and piezoelectric polarization in *Ga*-face and *N*-face strained and relaxed *AlGaN/GaN* heterostructures.

As a consequence, the alignment of the piezoelectric and spontaneous polarization is parallel in the case of tensile strain, and anti-parallel in the case of compressively strained top layers. If the polarity flips over from *Ga*-face to *N*-face material, the piezoelectric, as well as the spontaneous polarization changes its sign.

2.4.2 Charge density

[8] For determining the charge density I'll take as example the structure in fig. 2.5.

Associated with a gradient of polarization in space is a polarization induced charge density given by $\rho_P = \nabla P$. In analogy, at an abrupt interface of a top/bottom layer (*AlGaN/ GaN* or *GaN/AlGaN*) heterostructure the polarization can decrease or increase within a bilayer, causing a polarization sheet charge density defined by

$$\sigma = P(top) - P(bottom) = P_{SP}(top) + P_{PE}(top) - P_{SP}(bottom) - P_{PE}(bottom) \quad (2.7)$$

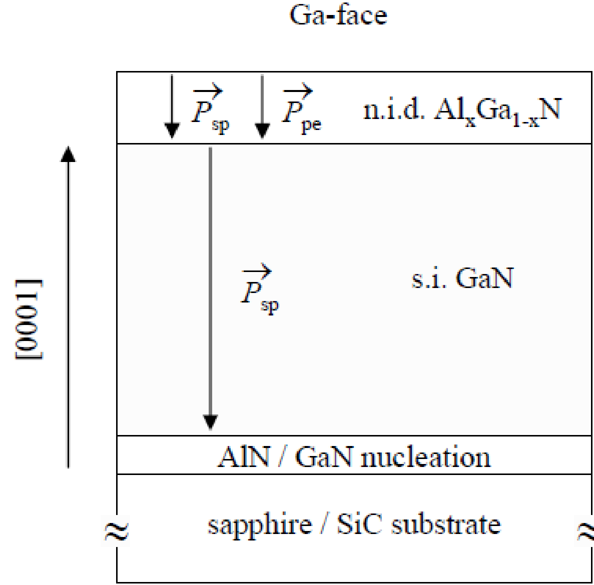

FIGURE 2.5: Directions of the spontaneous and piezoelectric polarization vectors for an undoped *Ga*-face *AlGaN/GaN* heterostructure where the *AlGaN* layer is under tensile stress.

Although, variations in composition, surface roughness, or strain distribution will alter the local distribution of polarization induced sheet charge density. However, the total sheet charge, which is associated with the change of polarization across the interface region will be very nearly equal to that present at an abrupt interface. If the polarization induced sheet charge density is positive ($+\sigma$), free electrons will tend to compensate the polarization induced charge. These electrons will form a 2DEG with a certain sheet carrier concentration (n_S) , assuming that the *AlGaN/GaN* band offset is reasonably high and that the interface roughness is low. A negative sheet charge density ($-\sigma$) will cause an accumulation of holes at the interface.

For a *Ga(Al)*-face *AlGaN* on top of *GaN* heterostructure the polarization induced sheet charge is positive (Fig. 2.4a). Even if the heterostructure is relaxed (*AlGaN* thickness $> 65nm$), electrons will be confined at the interface because of the difference in spontaneous polarization of *GaN* and *AlGaN*. If this heterostructure is grown pseudomorphic (Fig. 2.4b) the piezoelectric polarization of the tensile strained *AlGaN* barrier will increase the difference $P_{SP}(AlGaN) - P_{SP}(GaN)$, and likewise the sheet charge and the sheet carrier concentration. For *N*-face *AlGaN/GaN* heterostructures, the spontaneous and piezoelectric polarization have opposite directions in comparison to the *Ga*-face structure. The polarization induced sheet charge is negative, and holes can be accumulated at this interface (Figs. 2.4d and 2.4e). In *N*-face heterostructures, electrons will be confined if *GaN* is grown on top of *AlGaN*, due to the positive sheet charge which will be formed in this case (Fig. 2.4f).

To calculate the amount of the polarization induced sheet charge density σ at the $AlGaN/GaN$ and $GaN/AlGaN$ interfaces in dependence of the Al-content x of the $Al_xGa_{1-x}N$ barrier, we use the following set of linear interpolations between the physical properties of GaN and AlN:

- lattice constant:

$$a(x) = (-0.77x + 3.189) \cdot 10^{-10}[m] \tag{2.8}$$

- elastic constants:

$$C_{13}(x) = (5x + 103)[GPa] \tag{2.9}$$

$$C_{33}(x) = (-32x + 405)[GPa] \tag{2.10}$$

- piezoelectric constants

$$e_{31}(x) = (-0.11x - 0.49)[C/m^2] \tag{2.11}$$

$$e_{33}(x) = (-0.73x + 0.77)[C/m^2] \tag{2.12}$$

- spontaneous polarization

$$P_{SP}(x) = (-0.052x - 0.029)[C/m^2] \tag{2.13}$$

The amount of the polarization induced sheet charge density for the undoped pseudomorphic N-face heterostructure is calculated using the equations (2.6), (2.7) and (2.13):

$$|\sigma| = |P_{PE}(Al_xGa_{1-x}N) + P_{SP}(Al_xGa_{1-x}N) - P_{SP}(GaN)| \tag{2.14}$$

$$|\sigma| = \left| 2\frac{a(0) - a(x)}{a(x)} \left[e_{31}(x) - e_{33}(x)\frac{C_{13}(x)}{C_{33}(x)} \right] + P_{SP}(x) - P_{SP}(0) \right| \tag{2.15}$$

By increasing the Al-content of the barrier, the piezoelectric and spontaneous polarization of $AlGaN$ are increasing. The sheet charge density caused by the different total polarizations of $AlGaN$ and GaN is increasing slightly more than linear, as shown in figure 2.6, where the amount of the spontaneous, piezoelectric, and total polarization of

the *AlGaN* barrier, as well as the sheet charge density at the *GaN/AlGaN* interface, are shown versus the *Al* percentage. It can clearly be seen that both polarizations significantly contribute to the total sheet charge over the entire range of *Al* alloy composition.

For $x = 0.18$, a remarkably high sheet charge σ of $1{\cdot}10^{13}cm^{-2}$, increasing to $1.7{\cdot}10^{13}cm^{-2}$ if the *Al*-content of the barrier is enhanced to $x = 0.3$, is determined. These calculated sheet charges located at the *AlGaN/GaN* interface are about ten times higher than in comparable heterostructures of other $III-V$ heterostructures.

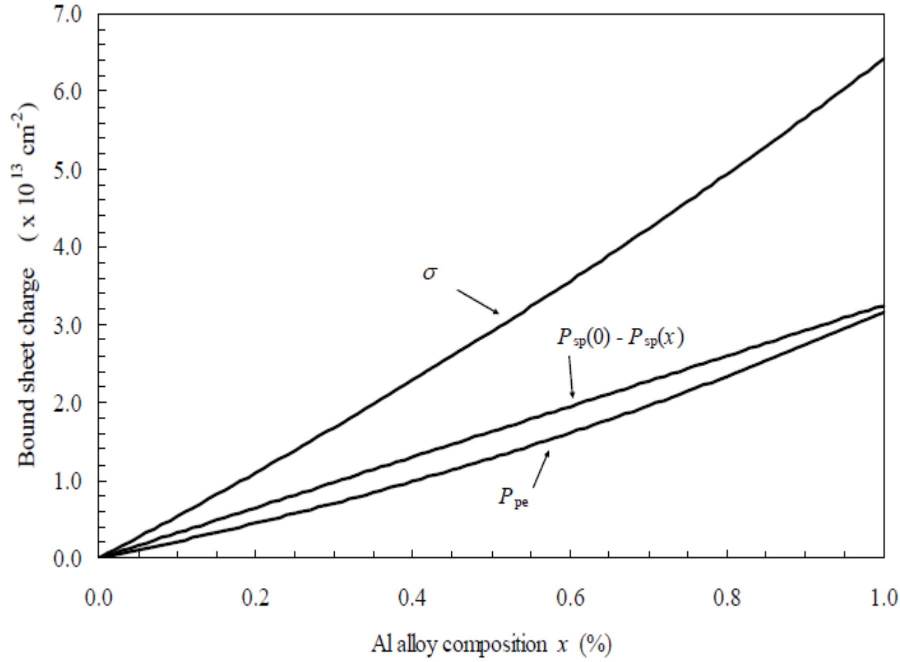

FIGURE 2.6: Polarization induced bound sheet charge at *AlGaN/GaN* interface as a function of *Al* alloy composition of the *AlGaN* barrier layer for *Ga*-face undoped material.

Although an accurate calculation of the 2DEG density in this structure would require a sophisticated simulation tool, a simple semi-classical electrostatic analysis assuming charge neutrality to hold between the sheet charge densities at the surface and the interface, leads to the following analytical expression for the 2DEG sheet charge density (n_S) as a function of the *Al* alloy composition (x) of the $Al_xGa_{1-x}N$ barrier layer:

$$n_s(x) = \frac{+\sigma(x)}{e} - \left(\frac{\epsilon_0\epsilon(x)}{de^2}\right)(e\Phi_b(x) + E_F(x) - \Delta E_C(x)) \tag{2.16}$$

where d is the width of the *AlGaN* barrier $e\Phi_b(x)$ is the Schottky Barrier of the gate contact, E_F is the Fermi level with respect to the *GaN* conduction-band-edge energy, and $\Delta E_C(x)$ is the conduction band offset at the *AlGaN/GaN* interface. To determine the sheet carrier concentration from the polarization induced sheet charge density from eq. 2.16, we use the following approximations:

- dielectric constant:

$$\epsilon(x) = -0.5x + 9.5 \tag{2.17}$$

- Shottky barrier:

$$e\Phi_b(x) = 1.3x + 0.84[eV] \tag{2.18}$$

- Fermi energy:

$$E_F(x) = E_0(x) + \frac{\pi\hbar^2}{m^*(x)} n_S(x), \tag{2.19}$$

where the ground Fermi energy (E_0) is given by

$$E_0(x) = \left\{ \frac{9\pi\hbar e^2}{8\epsilon_0\sqrt{8m^*(x)}} \frac{n_S(x)}{\epsilon(x)} \right\}^{2/3}, \tag{2.20}$$

the band offset ($\Delta E_C(x)$) is

$$\Delta E_C(x) = 0.7(E_g(x) - E_g(0)) \tag{2.21}$$

and the effective electron mass $m^* = 0.22m_e$.

The band gap of *AlGaN* is measured to be

$$E_g(x) = xE_g(AlN) + (1-x)E_g(GaN) - x(1-x) \tag{2.22}$$

Using equations (2.16) - (2.22), the 2DEG sheet charge density can be calculated as a function of *Al* alloy composition or the thickness of the barrier layer assuming the surface barrier to be constant. Figure 2.7 shows the calculated 2DEG density as a function of the *Al* alloy composition with the *AlGaN* barrier thickness as a parameter. In addition, the bound polarization induced sheet charge ($\sigma = \sigma_{2DEG}$) is plotted as a reference. Three *AlGaN* barrier layer thickness, 100$\AA$, 200$\AA$, and 300$\AA$ are plotted to illustrate the effect of barrier thickness variation. It can clearly been seen that for decreasing *AlGaN* barrier thickness the 2DEG density drops, which is due to increased Schottky barrier depletion, and that the 2DEG density approaches the bound polarization induced sheet charge for increasing *AlGaN* barrier thickness.

In accordance on what written before, the resulted polarizations create a positive charge (σ_{int}) in the *AlGaN/GaN* interface. Because of the neutrality of the system, a negative charge (σ_{comp}) is present at the *AlGaN* top interface, which compensates the σ_{int}. In fig. 2.8 are presented the band diagram of a typical *AlGaN/GaN* heterostructure and the relative charges position. In the region close to the contact it can be seen a negative charge (σ_{surf}) and in the *GaN* buffer layer can be seen the another negative

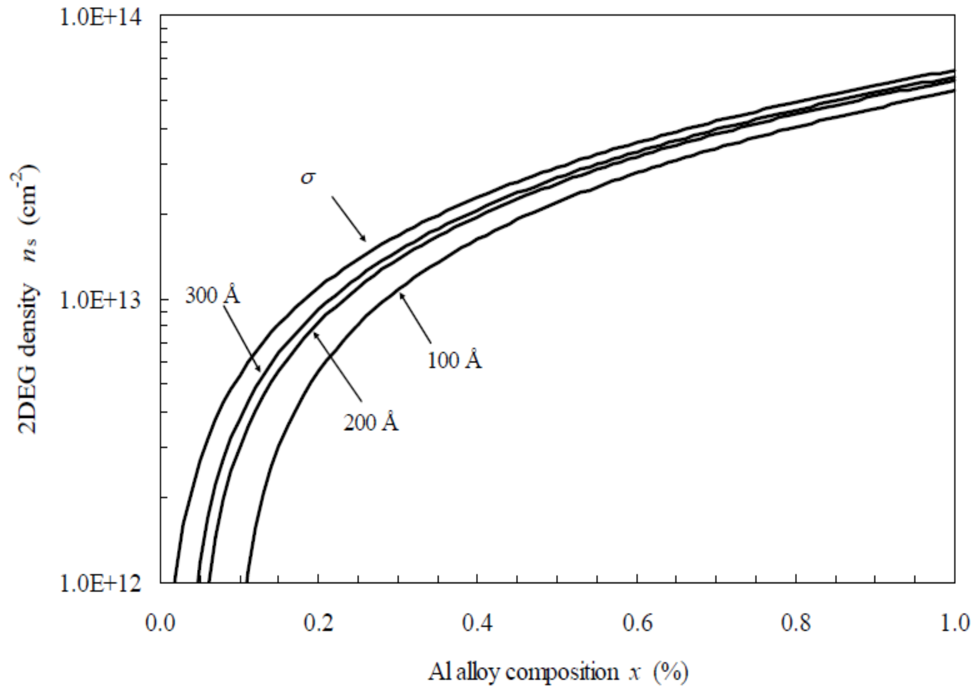

FIGURE 2.7: Calculated 2DEG density as a function of the *Al* alloy composition of the *AlGaN* barrier barrier layer for three different thickness. The bound polarization induced sheet charge σ is plotted as reference.

charge (σ_{2DEG}) that originates the 2DEG. These electrons have an increased mobility in comparison to electrons in the bulk of the active layer, since the carriers are spatially separated from dopants in the barrier layer. From a bands diagram point of view the 2DEG presence is visible because the conduction band of the *GaN* in the proximity of the *AlGaN* layer crosses the Fermi level, meaning that a large amount of electrons are accumulated there.

Understanding and controlling the source of the electrons in *AlGaN/GaN* HFETs is important for the optimization of their performance. However, the issue is currently not well understood. One of the possible scenarios is based on the existence of the surface donor-like states in the *AlGaN* layer. Indeed it has to be noted that as the considered *AlGaN/GaN* structures are undoped, the compensating mobile sheet charge density (σ_{2DEG}) consists of electrons that must be originated within these two layers. This surface positive charge at the surface could be originated from dangling bonds or from interaction with the ambient. [9] The 2DEG cannot be due to electrons generated thermally in the buffer, which have to leave behind a positive space charge. Furthermore, since the magnitude of the buffer charge should be as small as possible in a well-designed FET, it is reasonable for the sake of clarity to neglect it entirely and assume that the Fermi level lies close to the *GaN* conduction band edge. The 2DEG can be instead originated by donors in the *AlGaN* barrier, so too a positive surface charge must be

due to electron transfer from donor-like surface states into empty states in the *GaN* that are lower in energy. Conversely, any negative surface charge must be due to the transfer of electrons into acceptor-like surface states at the expense of the 2DEG. Put into words therefore, the number of the electrons in the 2DEG is equal to the number of ionized donors in the *AlGaN* layer, if they are present, plus(minus) the number of ionized donor(acceptor)-like states on the surface. For a truly undoped barrier, it follows that any 2DEG electrons are due to donor-like surface states.

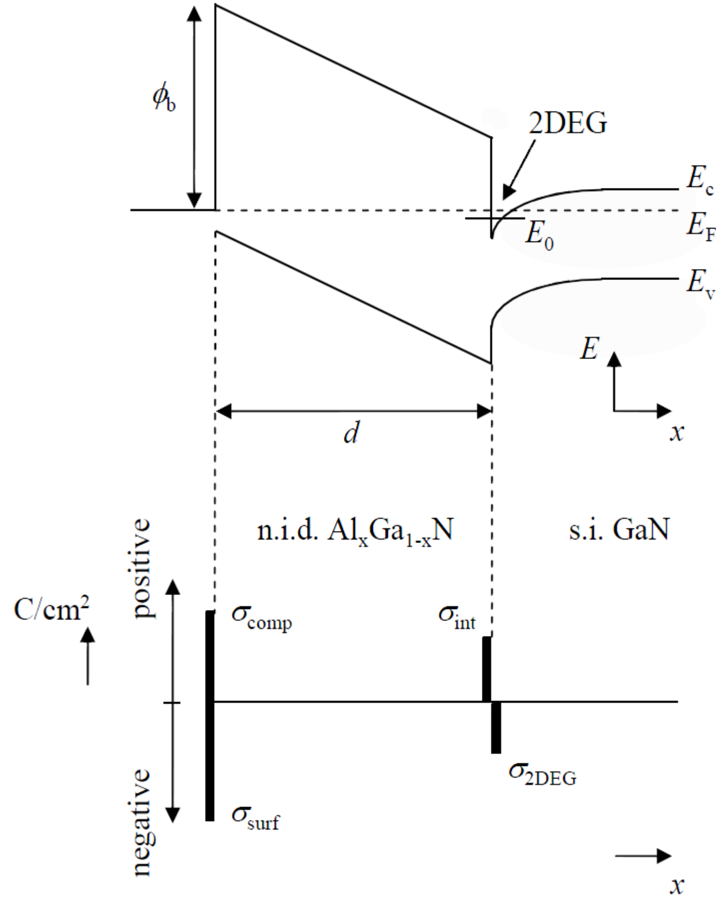

FIGURE 2.8: Energy band diagram of a *Ga*-face undoped *AlGaN/GaN* heterostructure and the polarization induced bound and compensating mobile sheet charge densities.

It has to be noted that the 2DEG exists as long as the *AlGaN* barrier is thick enough to allow the valence band to reach the Fermi level at the surface. Ibbetson et all. discovered that no 2DEG was observed for an *AlGaN* barrier thickness less than $35\mathring{A}$ (the measured charge was $< 10^{11} cm^{-2}$). The 2DEG density then increased rapidly with increasing barrier thickness, reaching a value of $7.1 \cdot 10^{12} cm^{-2}$ at $70\mathring{A}$. The increasing of 2DEG population is not however proportional at the barrier thickness because over a certain value strain relaxation starts to occur and no 2DEG population increment has been seen. They guess that the donor-like surface states are located quite deep in the *AlGaN* band gap, they will all be occupied at small values of *AlGaN* thickness (d). No 2DEG will

be formed and the field in the top layer will be determined by the polarization-induced charges (fig 2.9 (a)). As the width of the *AlGaN* layer increases, the Fermi level at the surface slides down approaching the deep donor level (fig 2.9 (b)). Once the Fermi level hits the surface states they start emptying. A two-dimensional electron gas can then be formed at the *AlGaN/GaN* interface and the field in the *AlGaN* barrier will be reduced (fig 2.9 (c)).

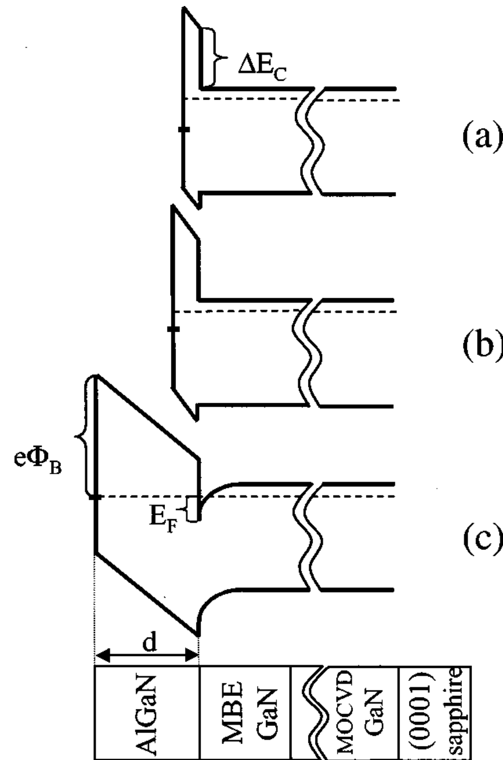

FIGURE 2.9: Schematic diagram showing the development of the band structure in *AlGaN/GaN* samples with increasing *AlGaN* barrier width.

2.5 Doping

Since the 2DEG is formed spontaneously, without any kind of doping, doping is not so relevant as in the silicon technology. Indeed, in *AlGaN/GaN* HEMTs, the polarization and interface charges rather than doping determine the channel charge. [4] However doping is important because allows changing the materials properties as needed. III-N semiconductors are doped with impurities such as *Si*, *Ge*, *Se*, *Mg*, *O*, *Be* and *Zn*. Typical unintentional impurities are *C*, *H* and *O*, that are incorporated during the growth, and grown-in defects.

[10] There are however other materials that can be added. For instance Aluminium can be used as a dopant in such a way to improve the performance by reducing traps concentration. Doo-Hyeb Youn et all. reached good results by implementing *Al* doping

into GaN material, i.e. the performance achieved was better than those obtained without Al.

2.5.1 N-Doping

[4] N-Doping is caused by N vacancies (the main reason), Ga interstitials or Oxygen incorporation, in an unintentional doped GaN material, depending on the grown method. However Si doping is the typical choice for intended N-doping. The activation energy of the Si in GaN material is $5 - 9meV$, which allows effective doping. Apart from the polarization, silicon doping can serve as additional carrier source for instance when it puts on the top of the $AlGaN$ layer a Si-doped GaN sheet in such a way to provide more electrons in the 2DEG.

2.5.2 P-Doping

[11], [12] P-Doping is used when high buffer resistivity wants to be achieved, for example when it wants to have both a complete channel pinch-off and an efficient off-state high voltage blocking. Indeed for empty the channel a sort of compensation will help and at the same time it will ensure a more difficult path for the electrons that are moving from the source to the substrate. This latter behaviour is called *punch-through* and it is one of the factors that limits the break-down voltage in the HEMT devices. The reason for the compensation is that the P-doping captures some electrons, preventing their movement and therefore the participation at the current flow. Fe doping into the GaN buffer layer should be employed to avoid the charge compensation effect in the channel, indeed most parts of the GaN buffer layer has a uniform Fe doping concentration (typical value of $10^{17} - 10^{18}cm^3$, with the Fe concentration decaying rapidly toward the $AlGaN/GaN$ interface and reaching the detection limit near the interface. Young Chul Choi et all. found an increment of break-down voltage of a factor of 2 respect to the devices without P-doping, keeping the on-resistance low, in such a way to minimize the power loss. This means that high resistivity substrate has been produced, avoiding the electrons flowing toward the substrate. The resistivity that can be reached is $> 10^5\Omega \cdot cm$, like Masashi Kubota et all. managed to reach (resistivity value of the bottom GaN layer higher than $10^{18}\Omega \cdot cm$). For the compensation I wrote about before, iron doping will affect the threshold voltage as well, as reported by Young Chul Choi et all. Indeed they found a rightward shift of the V_{th} value in the sample doped with Fe.

2.6 Traps in *GaN* and *AlGaN*

[2] The structures built using wide band semiconductors suffer from trapping and detrapping of 2DEG electrons both inside the layer structure and at the semiconductor surface. These trapping effects give rise to the formation of quasi-static charge distributions that cause the current-voltage (I-V) characteristics at microwave frequencies to be considerably lower than under direct-current (DC) conditions. Consequently the microwave output power capability of the devices is significantly lower than expected from the DC output (I-V) characteristics and the chosen operation class.

Whereas the occurrence of traps heavily affects the device performances, it's very important understanding the traps spatial and energy locations. The presence of traps is partially due to the heteroepitaxy growth technique and for this reason traps could be generated both within the layer and in the heterointerface. The former type is due to the not still perfect material quality obtained by the growth process. The latter type instead is due to the difference in the lattice constant of the two semiconductors, meaning that the material grown on top produces defects because it has to adapt its lattice parameter at the one of the lower material (fig 2.10). Both of the type produce defects like the ones showed in fig 2.11.

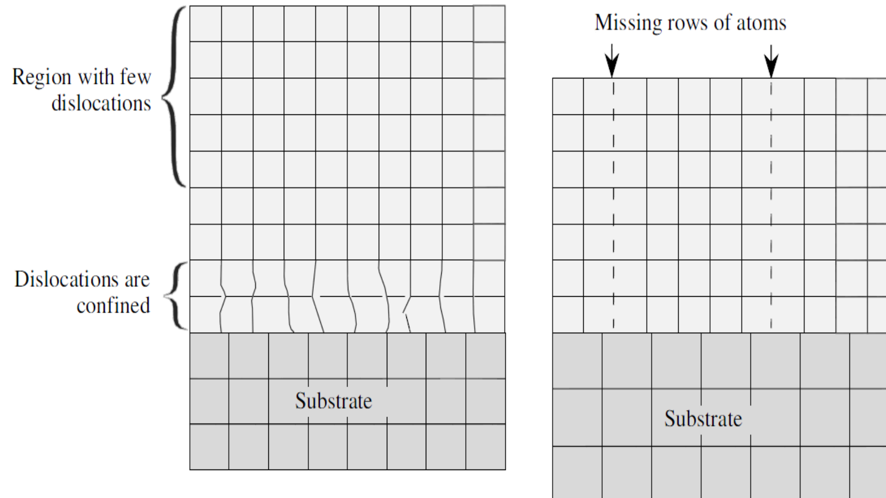

FIGURE 2.10: The left hand side figure shows a desirable structure in which the dislocations are confined near the overlayer-substrate interface. On the right hand side, the dislocations are penetrating the overlayer.

[13] There are also superficial donor traps, produced by dangling bonds, witch behave like positive superficial charges.

All of these traps degrades the device performance because they cause a reduction of the drain current due to the *current collapse*, a phenomena by which the 2DEG is depleted. This mechanism will be explained later in this section.

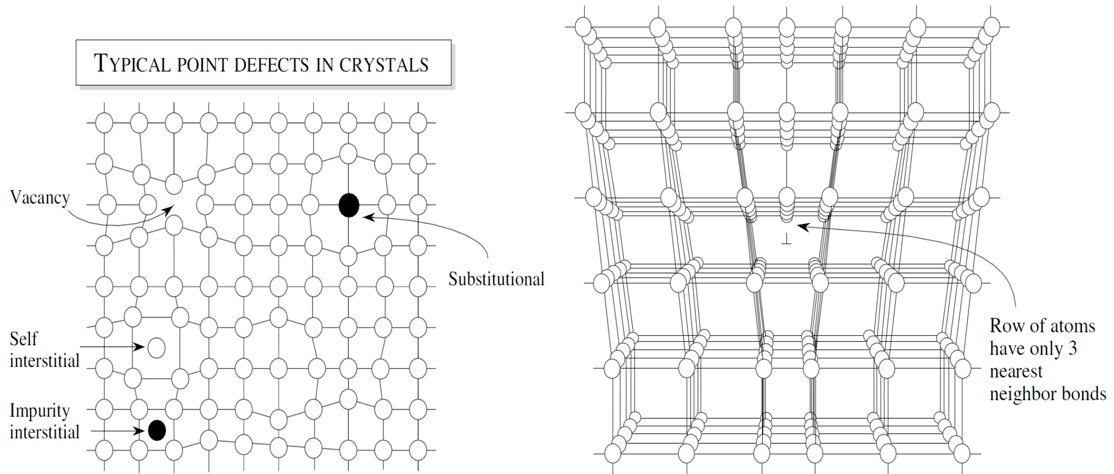

FIGURE 2.11: **left:** some important point defects in a crystal. **right:** volumetric dislocation.

It has to be said that in literature there is no coherence about the traps energy locations in GaN material and even the causes of their presence are not clear because deep levels traps can have many origins, e.g., impurities, point defects, extended defects, growth conditions. For this a detailed characterizations of the traps is not available to date. However a traps summary has been done in order to collect the latest informations regarding traps.

The results which come from various efforts to characterize the traps in the GaN material are different considering various papers:

- [14] Klein et all. have reported two main deep levels for the electrons in the GaN bulk layer, one at $1.8eV$ and another one at $2.85eV$ from the conduction band.
- [15], [16], [17], [18] Polyakov et all. assumed the electrons traps in the undoped GaN located mainly at $0.5 - 0.6eV$ and $1.0eV$ from conduction band, where the former level is due to dislocation in the lattice and the latter level is formed by nitrogen interstitials or gallium vacancies. They discovered another minor effect due to level at $0.25eV$ from the CB. For the Fe-doped device the level they found is at $Ec - 0.5eV$, probably related to the Fe energy level or related to the defects promoted by Fe incorporation.
- [19] H. K. Cho et all. spoke about traps situated at $E1 = 0.18 - 0.27eV$ associated with N vacancy and to defects caused by different buffer growth conditions and $E2 = 0.50 - 0.60eV$ from the CB, originated from N antisite.
- [20] Masashi Kubota et all., using a photoluminescence (PL) measurements in an undoped material, presumes that the origin of the so-called yellow luminescence

(YL) in *GaN* has been assigned to acceptor-type defect complexes composed of *Ga* vacancies (VGa) and/or VGa-O at $2.2eV$ from the CB, and the origin of the blue luminescence is due to carbon impurity levels at $2.8eV$ from the CB. Only for the *Fe*-doped *GaN* they found a level at $1.3eV$ as well as the other two. This could be due to the defects induced by *Fe* dopant.

- [21] Jungwoo Joh and J. del Alamo wrote about shallowed traps in *GaN* material that are thermally activated and deep traps which are not thermally activated.
- [22] T. Okino et all discovered, by DLTS measurement, two electron traps levels with activation energy of $0.58eV$ and of $1.1eV$.

If there is quite confusion in *GaN* traps data because various efforts have been done in order to characterize this material, the same cannot be said for the *AlGaN*, for witch only a few efforts have been done.

[21] The only paper I found regarding the *AlGaN* traps is the one written by Jungwoo Joh and J. del Alamo. They found electron traps in *AlGaN* layer with an activation energy of $0.57eV$ from the conduction band, responsible for the performance degradations. Indeed these traps become a path way for electrons to flow from the gate down to the channel. If these traps get filled with electrons, their electrostatic influence partially depletes the electron charge in the channel and this degrades maximum drain current.

[4] The interfaces in heterostructures are typical locations for the presence of traps, due to the abrupt modification of the lattice constant. Moreover in the top interface of the *AlGaN* a strong strain is observed in the *GaN* material that constitute the cap layer, when this layer is present. This strain yields strong optical emission at energy $< 1.6eV$.

Not only in the interfaces there are traps but in the region underneath the gate as well. [23], [24] Since *GaN* and *AlGaN* are strongly piezoelectric materials, in response to high voltages, large stresses are induced inside these layers. By their very nature, in an *AlGaN/GaN* HEMT under high voltage operation, a large electric field appears under the gate edge across the barrier. This can result in very large mechanical stress concentrated in a very small region of the *AlGaN* barrier. To make matters worse, due to their lattice mismatch, *AlGaN* on *GaN* is typically under substantial tensile strain and therefore stores a sizable amount of elastic energy at rest. Under electrical stress, very high in the gate edge region, the elastic energy in the high-field region increases on top of this. If the elastic energy exceeds a critical value, crystallographic defects are formed. These defects are electrically active and affect the device characteristics in a profound way. *Cross-Sectional Transmission Electron Microscopy* (XTEM) studies of degraded devices have shown the presence of prominent crystallographic damage on the

drain side of the device right next to the gate edge. The damage consists of dimples, cracks that extent through the *AlGaN* but stop at the *GaN* interface and, in extreme cases, metal diffusion from the gate down the crack.

[25] As in the *GaAs* case, surface trapping can generally be identified through gate lag measurements. A number of groups have used this approach to study the effect of trapping on *GaN* devices. Is very important to understand the traps effect because in this kind of devices it increases the current collapse phenomena. The association between gate lag and surface trapping is generally established by correlating gate lag with changes made to the device surface through techniques such as chemical treatment or dielectric passivation. Binari et al. associated gate lag with the presence of surface trapping in the access region between gate and drain.

[4] According to what written above, it understands that the effects of the traps in wide band gap materials is very important since significant current reduction have been discovered. The most well known one is the *generation/recombination* mechanisms. These mechanisms, by which the electrons don't participate at the current flow, involve the following process:

1. SRH generation/recombination, more evident for high temperature as the SRH effect increase its efficiency with the temperature rises up;
2. Radiative and Auger recombinations, particularly evident at high carrier concentration, hence very important in the 2DEG region.

Another effect is the *current collapse*.

2.6.1 Current Collapse

[2] The current collapse in *GaN*-based HFETs can be caused by instabilities in the positive compensation charge density, mostly in the gate to drain region, that needs to be present to maintain the 2DEG channel. Such positive sheet charge can arise from the polarizations, the donor-like traps in *AlGaN* layer and from surface states created by dangling bonds, threading dislocations accessible at the surface, where ionized donor states are present. Neutralizing the positive surface charge, either by the capture of electrons in trap states or by the adsorption of charged ions from the ambient environment, leads to depletion of the 2DEG density and hence a reduction of the drain current and a lower output power. The current collapse observed during a drain lag measurement has been related mainly to trapping of hot 2DEG electrons inside the layer stack.

[4] The electrons responsible for this behaviour can come from the gate, in case of tunneling or of thermionic emission when the gate is in the reverse bias condition. Indeed, moving the bands upwards becomes more easy for the electrons jumping over the barrier or crossing the barrier by tunneling, if the barrier is thin enough, and go filling the traps in the *AlGaN* layer, compensating the positive charge. This process has been proved, because an effective barrier thinning through unintentional surface defect donors is found to enhance the Schottky barrier tunnelling in *AlGaN/GaN* FETs, leading an increment of the leakage gate current. Another situation in which an electron can compensate the positive charge in the layers above the buffer is when it has enough energy to jump from the electrons channel and go to fill the positive charge in the barrier. This latter condition requires high voltage and high current regime.

In order to restore the drain current, the net positive charge on the *AlGaN* surface has to be restored. [24] This can be done either by forward biasing the gate with respect to the source and drain or by illumination using photons with a properly energy, in such a way to free the electrons trapped in the upper layers of the device. The same result, but less intensive, could be obtained by heating the device.

Recovery from current collapse by thermal emission of the trapped carriers has a characteristic time dependence which can be investigated by measuring the drain current at a low drain-source voltage (typically $V_{DS} < 1V$) before and after applying a large drain-source voltage (typically $V_{DS} > 20V$) while keeping the gate-source voltage at $0V$ (open channel). Exposure to the high drain-source voltage induces current collapse and the recovery of the drain current to its low-field value has been monitored as a function of time. [21] Alamo et al. have determined two time constants, designated as fast ($\approx 0.1s$) and slow ($> 10s$), which can be assigned to traps at the semiconductor surface, at deep levels in the *AlGaN* barrier layer and traps at the *AlGaN/GaN* interface.

[2] A continuous transition from partial to complete drain current recovery was observed upon decreasing the wavelength of the light used from $720nm$ to $366nm$ (corresponding to the *GaN* bandgap energy at RT), respectively. The same behaviour can be observed if the ambient temperature is increased up to temperatures over 150^oC, which is consistent with thermal emission of trapped electrons from shallow traps.

The conclusion is that the trapping of electrons responsible of the current collapse occurs either in the *AlGaN* barrier layer or at the *AlGaN* surface and not in the *GaN* buffer layer. Despite the fact that this effect has been observed over a wide range of time and frequency, which makes it very difficult to unambiguously determine the location of the responsible trapping mechanism, various research groups have confirmed that drain current reduction during large-signal operation at microwave frequencies is mainly caused by trapping of electrons at the free *AlGaN* surface.

[13], [26] It has been reported that the current collapse can effectively be reduced by passivation of the free $AlGaN$ surface. Traditionally a silicon nitride film (SiN) has been used as a superficial passivation layer. However other passivation layers, e.g. silicon dioxide (SiO_2), scandium oxide (Sc_2O_3), and magnesium oxide (MgO), have also been reported. In the inset of fig 2.12(left) it can see the passivation layer which covers the top of the device. The deposition of a SiN film results in an increase of the 2DEG density and in a little shift of the threshold voltage towards more negative value. The reasons for these effects are various:

- upon passivation with *SiN* the properties of the surface traps are changed leading to an unchanged or even slightly increased amount of positive charge at the *SiN/AlGaN* interface preventing drain current reduction;
- *SiN* film buries the positively charged surface donors and makes them inaccessible to electrons leaking from the metal gate. The total amount of positive surface charge remains unchanged, at least, and drain current reduction is prevented. In addition to this mechanism, the *SiN* film or the deposition process is assumed to change the energy level of the surface donor;
- *SiN* avoid the interaction of the active layer surface with the air.

[26] The drawback of the passivation is the increment of the gate leakage current because of the occurrence of deep traps at the surface, as argued by S. Arulkumaran at all. In his experiment he showed that the passivation layer helps to reduce the current collapse (fig 2.12 left) but at the same time it increases the gate leakage (fig 2.12 right).

[27] Another solution possible in order to overcome at the collapse of the drain current is using *GaN/AlGaN/GaN* epitaxial structures with a thin (typically $3-5nm$) *GaN* cap layer, that can be even n-type-doped. This sheet has been suggested to act as a surface-charge-control layer that reduces the effect of surface polarization charge by screening the 2DEG channel from the surface traps. The use of the *GaN* cap in combination with *SiN* surface passivation has actually allowed record output power performance as well as long-term stable RF operation to be achieved.

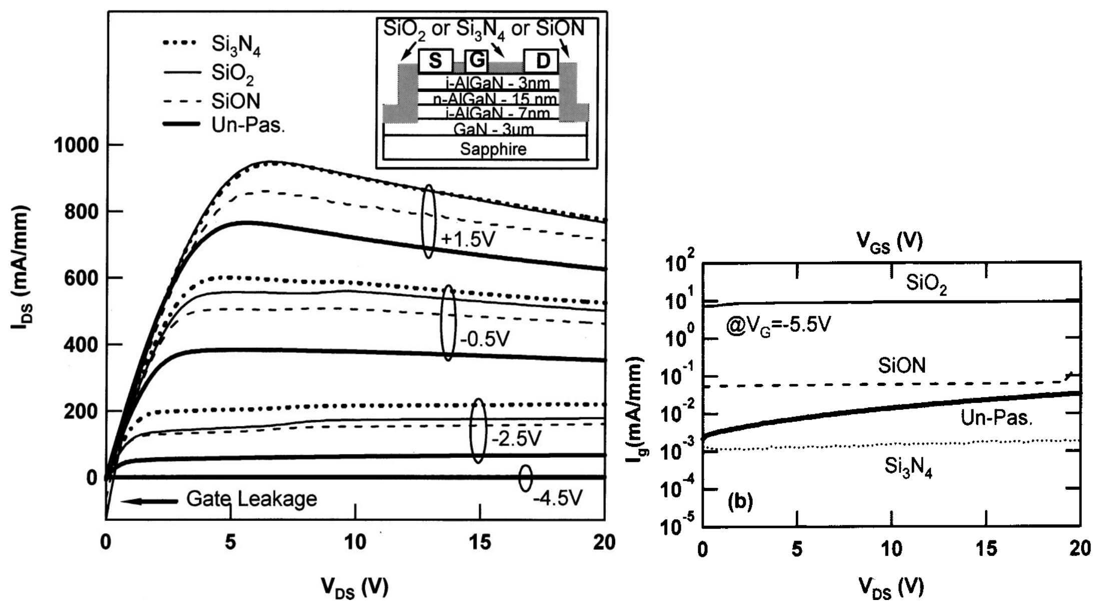

FIGURE 2.12: **left:**dc $I_{DS}V_{DS}$ characteristics of Si_3N_4, SiO_2 , $SiON$ passivated and unpassivated $AlGaN/GaN$ HEMTs on sapphire substrate. Inset is a schematic diagram of passivated $AlGaN/GaN$ HEMTs. **right:** IgV_{DS} characteristics of passivated and unpassivated HEMTs measured at subthreshold regime ($V_G = -5.5V$)

Chapter 3

HEMTs simulations

Simulation activity can be done by means of specific programs that try to reproduce the real behaviour of either a device or a circuit. In my case I utilized a microelectronics simulator, Sentaurus version 2010.03, provided by Synopsys, for simulate HEMT devices made with *GaN* and *AlGaN* materials.

Sentaurus simulator is composed by various programs, among them I used *Devise*, a structure editor, and *Dessis*, the simulator. With the first program it can create the structure of the device using various kinds of materials, like *Si*, *GaAs*, *Ge*, *GaN*, *AlN* and many others. With Dessis instead, it can use the structure created by the previous program, adding to it the suitable physical models and completing the input file with the choice of the type of simulation you want to run (DC, AC, pulse) as well as the goals you want to achieve, i.e. in case of HEMTs it can choose the Vd, Vg, Vs, Vb ranges. Beside these program I used *Techplot* and *Inspector* in such a way to check the structure and to see the simulation result. With Techplot it can also see the distribution of the physical parameters within the device. For this purpose the simulator resolves the Poisson equation, the continuity equation of electrons and the continuity equation of holes for each point of the *mesh*, where the mesh is an array of point in which the device is divided (fig 3.3).

Simulations are useful because they can help in the understanding of how the device works as well as they can be utilized in order to reproduce or predict a trend, without using real devices. Fabricating devices with wide band gap materials like *GaN* are very expensive, just think that a *GaN* row wafer costs thousands of $, so simulations can reduce the cost of a device studying. Moreover simulations are used beside the device characterization to improve the comprehension of the physical phenomena which are behind a certain behaviour.

In this chapter I will present the results obtained by carrying out simulations of two HEMT devices, the first one without *Field Plate* (FP) and the second one with it. We started with simple DC simulations, like IdVg and IdVd characteristics, then we moved towards most complicated ones, which are AC, leakage and breakdown simulations.

3.1 First device

In this fist set I run $IdVg$ and $IdVd$ simulations of an HEMT device without Field Plate. We compared all of these results with measurement data we got from NXP in order to fit the characteristics and to obtain a deck suitable for predictive simulations.

3.1.1 Device structure

The structure of the device I simulated as first is the one in fig 3.1.

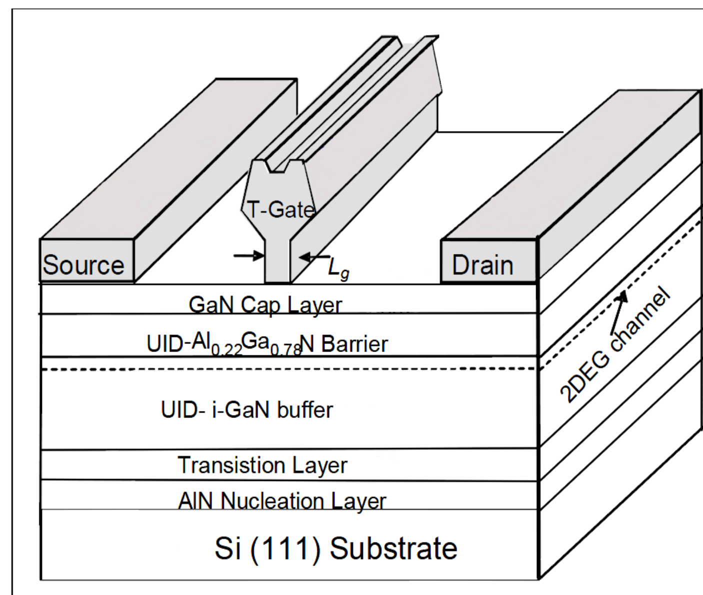

FIGURE 3.1: HEMT structure of the device object of the first set of simulations.

For its realization I used Dessis tool and I specified the substrate in *SiC*, the nucleation layer in *AlN*, the buffer layer in *GaN*, the barrier layer in *AlGaN*, the cap layer in *GaN*, the passivation layer on top of the device in *Nitride*, and the Drain and Source regions. In the end I placed the contacts of Gate, Drain, Source and Substrate and I obtained the structure shown in fig 3.2.

The next step was to create a good mesh in such a way to evaluate the electrical behaviour and the distribution of the physical parameters like electric field, electrons population, electrostatic potential and so on. For this purpose it has to be sure that all the

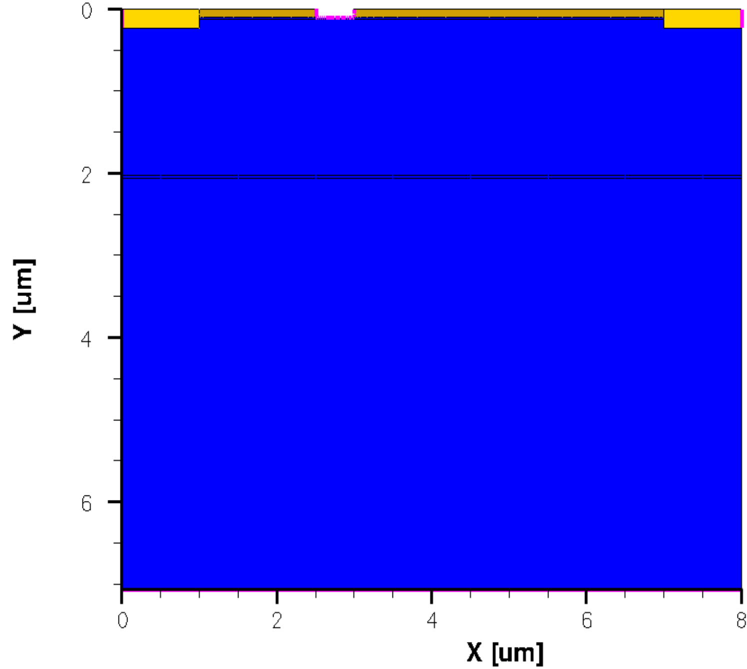

Figure 3.2: HEMT device structure for the first set of simulations implemented by Dessis tool.

regions subjected to high current, to high electric field and to abruptly changes have to be covered by a thin mesh. This means that a good mesh needs to be placed in the 2DEG region, which is the region interested by high current, in the regions where edges are present, that is where the high electric field is concentrated, and in the part where there are material changes. As a result I obtained the mesh shown in fig 3.3. In the top view it has shown the presence of a thin mesh in the upper part and in the middle part of the device. The mesh in the middle is present only because of the materials changes. In the bottom view is present a zoom of the gate area in which there are 2 different types of mesh, the thinner one for the 2DEG and for the materials changes, and the one which covers the gate edges.

3.1.2 DC simulations

The first simple simulation concerns *IdVg* characteristic. For this aim we firstly added the polarization charges due both to the piezoelectric and spontaneous effects, as written in chapter 2, then we added the following physical models: the *high electric field saturation* for the carriers and the *SRH* and *Auger* recombinations. The first model is used since high band gap materials are very suitable for high voltage applications and, as it is well known, at high electric field the carriers velocity starts not to follow the rule valid for low field, that is $v = \mu \cdot E$, where v is the carrier velocity, μ the carrier mobility and E the electric field. At high field indeed the carrier velocity saturates and

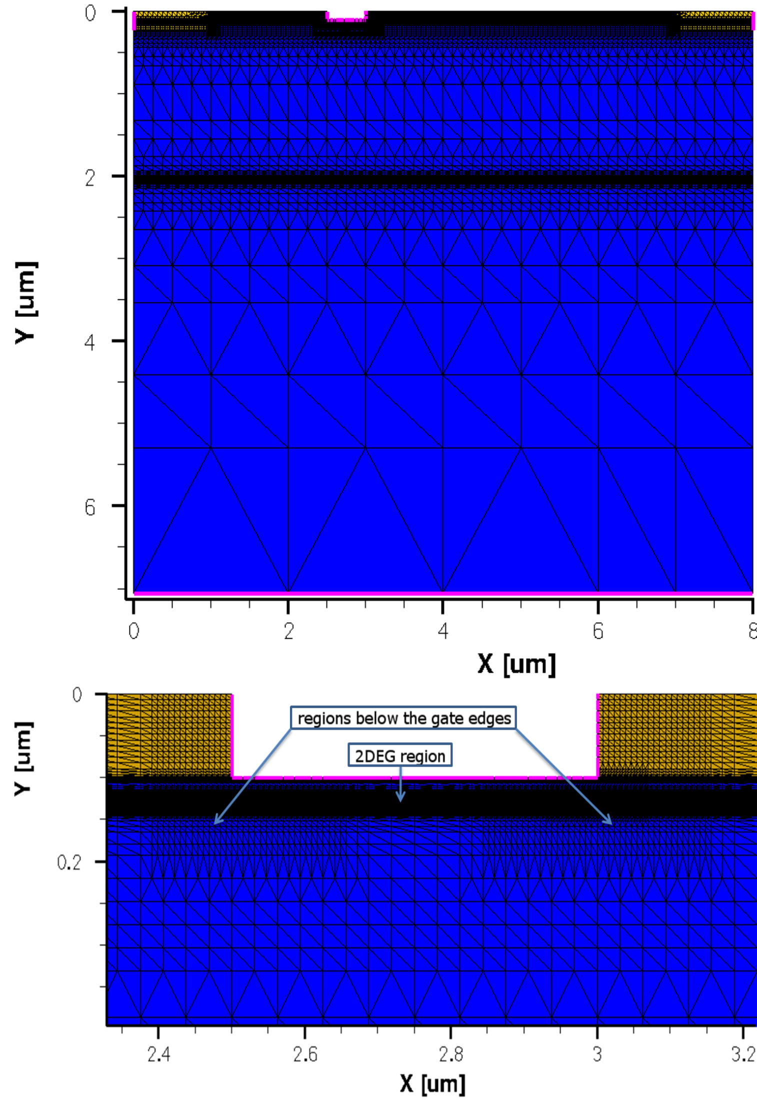

FIGURE 3.3: HEMT device structure for the first set of simulations with mesh included. ***top view:*** entire device, ***bottom view:*** zoom in the gate region.

for this reason it's useful taking into account this behaviour. The SRH and the Auger recombinations are important when high carrier concentration is involved, like the one which can be found at the *GaN/AlGaN* interface.

In the first set of simulations we implemented the *iron doping* as well. This because [28] good electrical isolation of the HEMT devices from the substrate is necessary to achieve both channel pinch-off and efficient OFF-state high-voltage blocking, which is supported by the low concentration of carriers in the *GaN* buffer layer. Since undoped *GaN* typically exhibits some degree of n-type conductivity, presumably due to the unintentional doping of residual impurities such as *Si* and *O*, the residual donors in an unintentionally n-doped *GaN* buffer should be compensated by deep acceptor states to obtain high resistivity. Young Chul Choi et all compared 2 HEMT devices, one with iron doping in the buffer layer and the other without it. They got a lowering in the

threshold voltage and a decrease in the $Idmax$ for the device doped with *Fe*, proving that the new material introduced is working as a P-dopant, decreasing the 2DEG concentration. In the doped device they found an enhancement in the BV as well, meaning that the *punch through* has been reduced. The punch through is a phenomena by which the electrons from the substrate can be easily injected to the drain through the thin *AlN* nucleation layer, in high voltage regime. In this situation, the premature device failure can occur at the *GaN/AlN/substrate* junction of the structure. Indeed in terms of OFF-state breakdown characteristics, it appears that the *GaN/AlN/substrate* junction is weaker than the *AlGaN/GaN* junction. Thus, the OFF-state breakdown behaviour may be stabilized by increasing the thickness of the *AlN* nucleation layer. However, the issue of surface cracking should be carefully considered with increasing *AlN* nucleation layer thickness. That's why they used *Fe* doping instead of further increasing the *AlN* thickness.

[20] *Fe* atoms incorporated in *GaN* matrix substitute *Ga* sites and introduce the charge transfer level $FeGa^{3+/2+}$ in the midgap. The energy of the level has been determined from the photo-luminescence PL excitation measurements to be $2.6eV$, 3.17 or $2.863eV$ above the VB, depending on the ionization status. The Fermi level pinning approximately $0.5-0.6eV$ below the *conduction band minimum* (CBM) has also been confirmed using a capacitance voltage method. When the ionization status moves form Fe^{3+} to Fe^{2+} by capturing an electron, an *Fe* atom acts as a compensating deep acceptor in *GaN*. As the *Fe* concentration is increased sufficiently in moderately *GaN*, the Fermi level shifts toward the midgap and $FeGa^{3+/2+}$ level is inversely transferred from $FeGa^{2+}$ to $FeGa^{3+}$ by releasing an electron. At this point the compensation occurs.

In order to introduce the iron doping into the device, firstly I added the *Fe* material in the *datexcode.txt* which is the materials list file included in the simulator. This has been done since iron material was not present in the available materials list. Beside its definition in the datexcode.txt I added the energy level, the electron cross section and the degeneracy factor of the new material in the parameter file of *GaN*. In this way Iron was available among the doping materials and it could be used directly in the device editor.

Afterwards, speaking with Giovanni Verzellesi, a professor from Reggio Emilia, we changed the iron doping declaration. In this new way we declared the *Fe* not as dopant material but as traps. This because Giovanni Verzellesi, an expert in HEMT simulations, said that the simulator treats doping in a simpler way respect to the traps, especially when deep levels are considered. This difference affects the simulation results as well, as it can see in fig 3.4. Indeed, in the device in which the Iron doping was implemented as dopant the current was higher than in the other case.

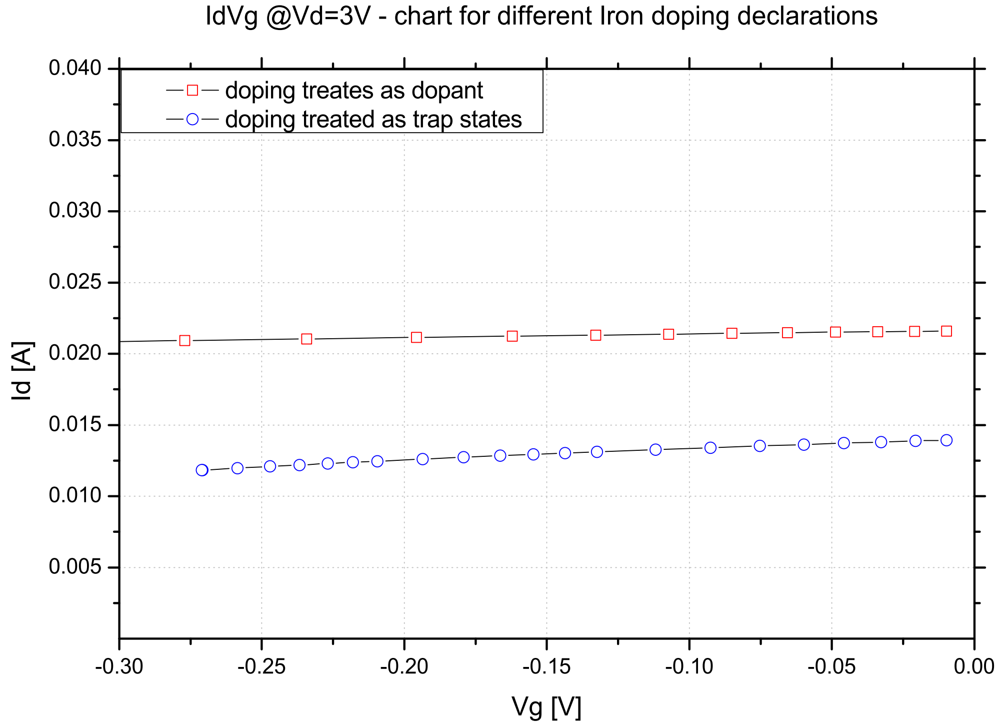

FIGURE 3.4: Simulations for different Iron doping declarations.

With the aim to check the iron doping behaviour, we run some simulations only varying the Fe concentration, keeping the activation energy and the electron cross-section constants. These two values have been set respectively at $0.8eV$ from the CB and $10^{-15}cm^{-2}$, the typical cross section value used in the simulations. The results obtained are depicted in fig 3.5 and it can see that increasing the Iron concentration the current is reducing, meaning that a compensation effect is more and more efficient, i.e. the doping helps to empty the channel by trapping the electrons. This behaviour is clearly seen both in the top view, where the on-state characteristics are present, and in the bottom view, where the sub-threshold characteristic is shown. Indeed, in both of the images the simulated curve is getting closer and closer to the measured one.

The next step has been the one to add the acceptor traps in the buffer layer. These traps behaves the same as the iron doping, i.e. they contribute to depopulate the 2DEG. By adding both the iron doping and the traps we managed to fit the $IdVg$ curves with the measured ones, obtained for various Vd values. The results, which are depicted in fig 3.6 - 3.9, have been obtained using a concentration traps of $3 \cdot 10^{17}cm^{-3}$, an activation energy of $1eV$ from the CB and a standard electron cross section of $10^{-15}cm^{-2}$.

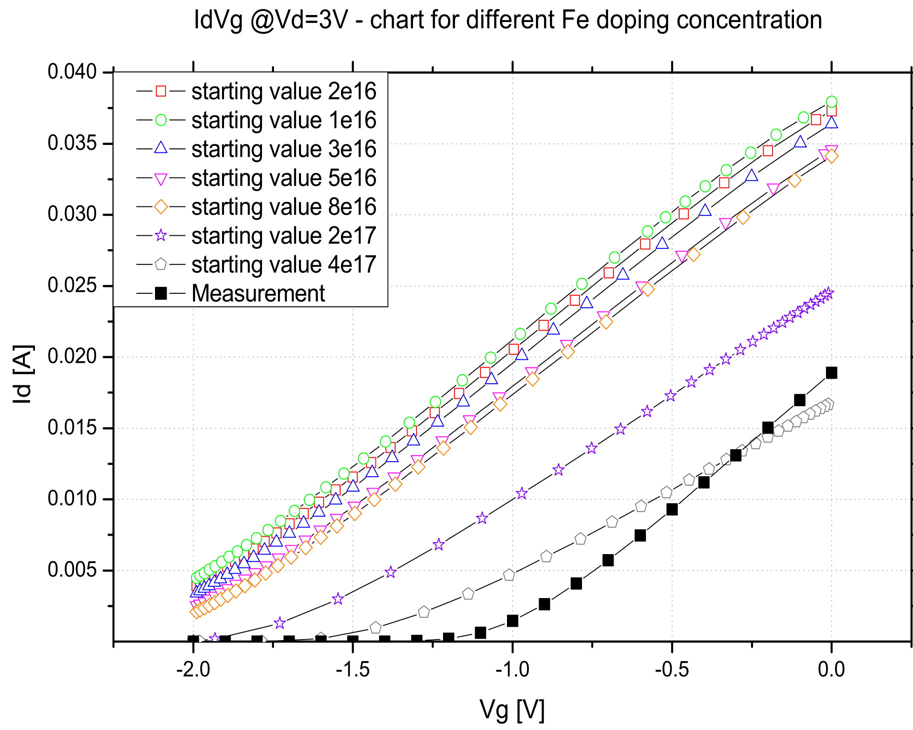

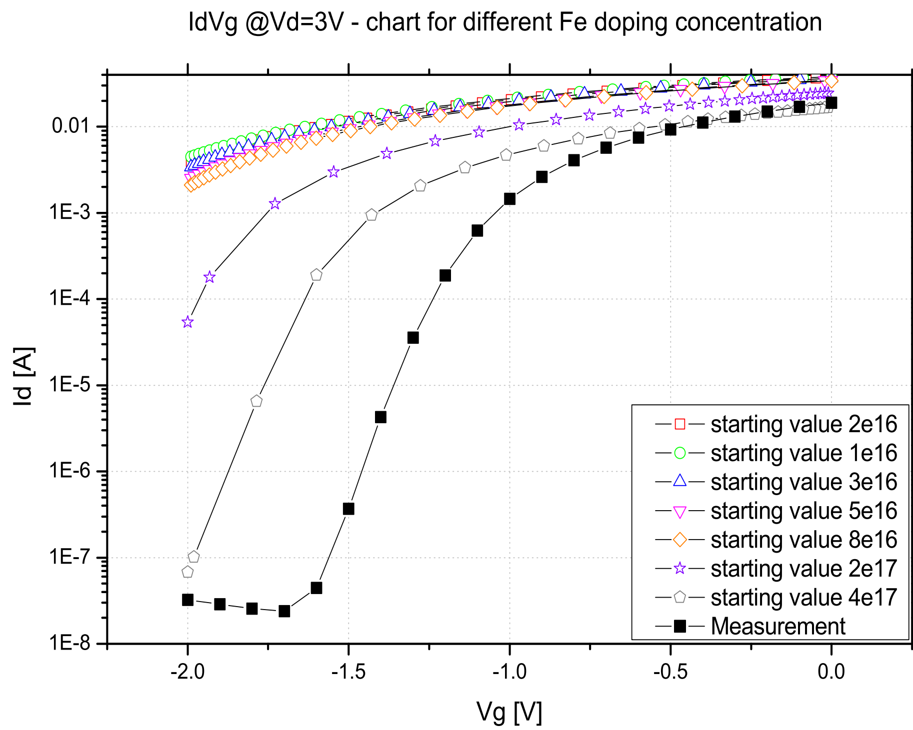

FIGURE 3.5: Comparison between simulation result with different Iron concentrations and measurements result. ***top view:*** on state characteristics, ***bottom view:*** behaviour below threshold voltage.

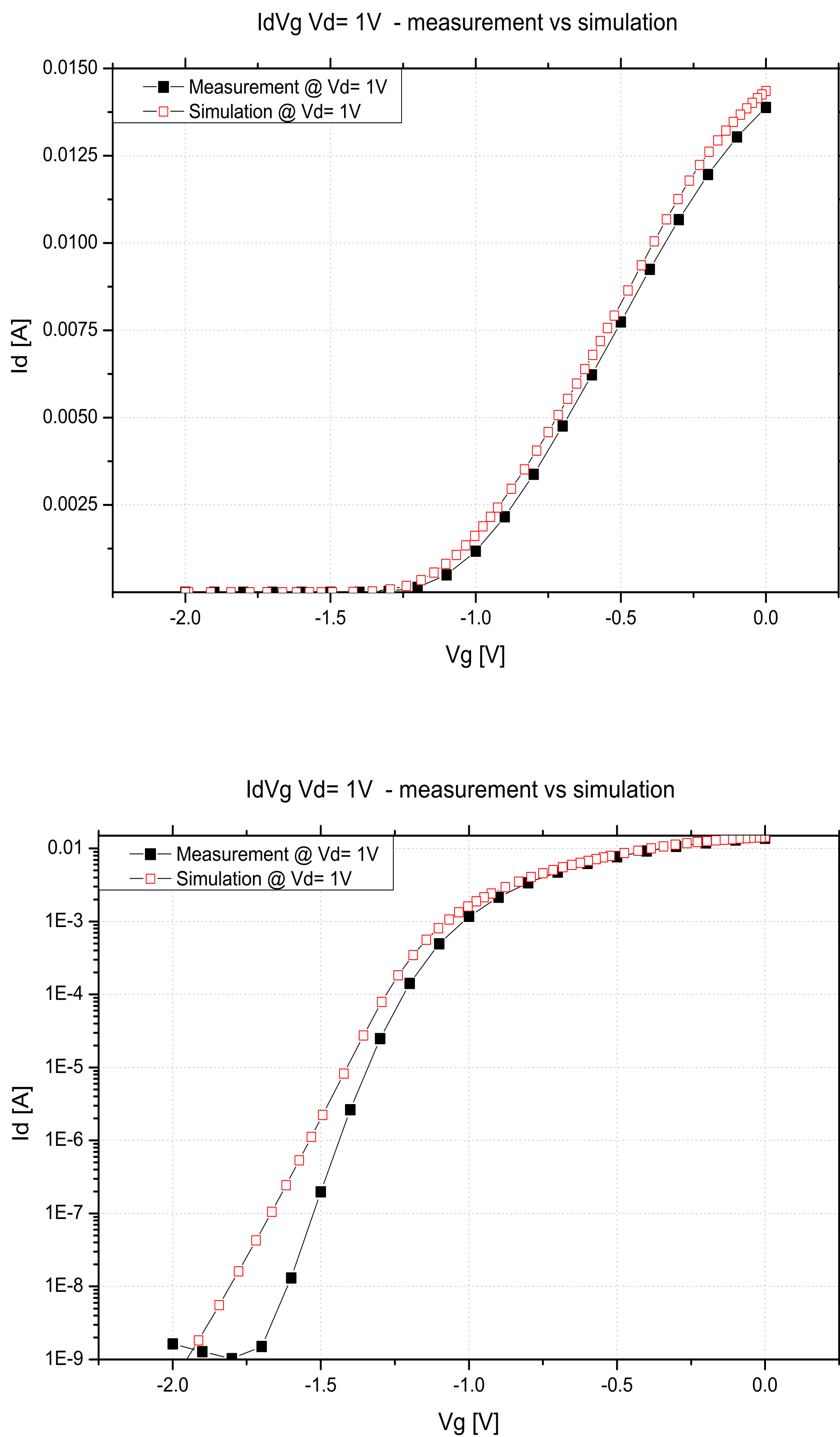

FIGURE 3.6: Comparison between simulation and measurement results for the first device. IdVg characteristic for $Vd = 1V$. ***top view:*** on state characteristics, ***bottom view:*** behaviour below threshold voltage.

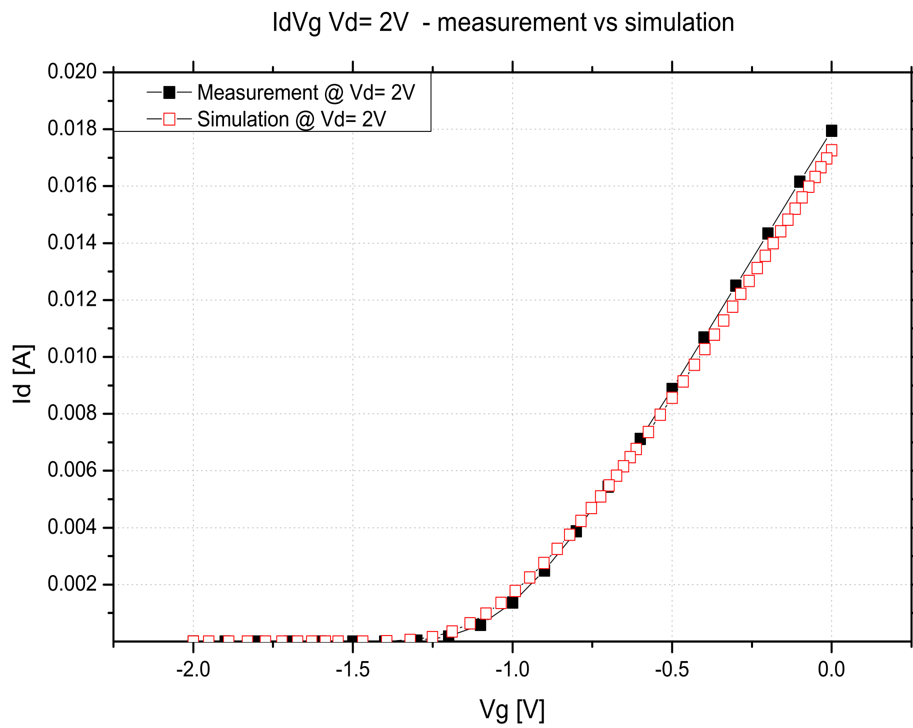

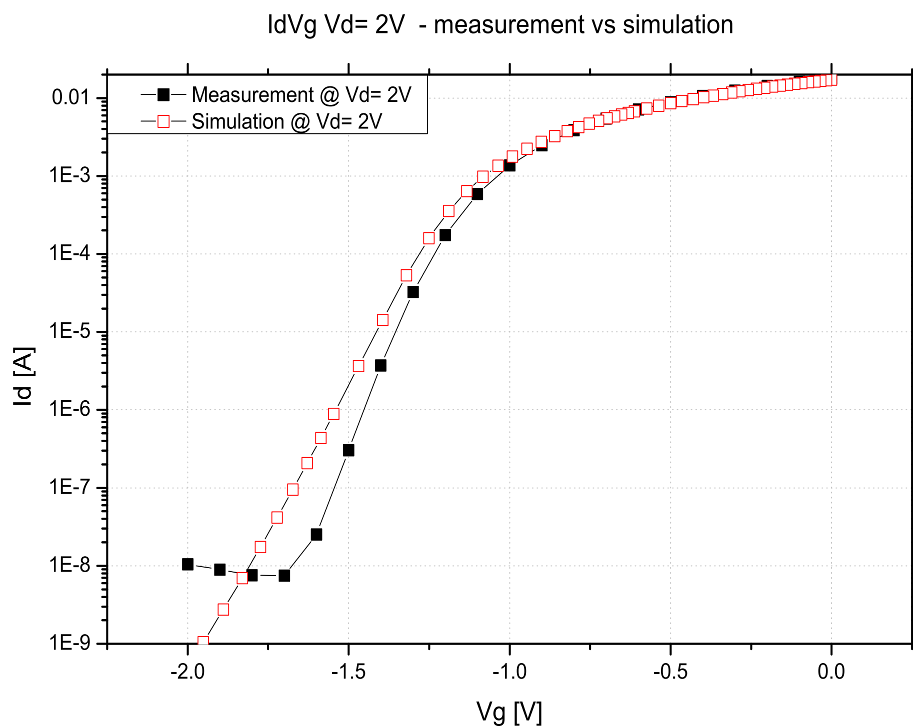

FIGURE 3.7: Comparison between simulation and measurement results for the first device. IdVg characteristic for $Vd = 2V$. ***top view:*** on state characteristics, ***bottom view:*** behaviour below threshold voltage.

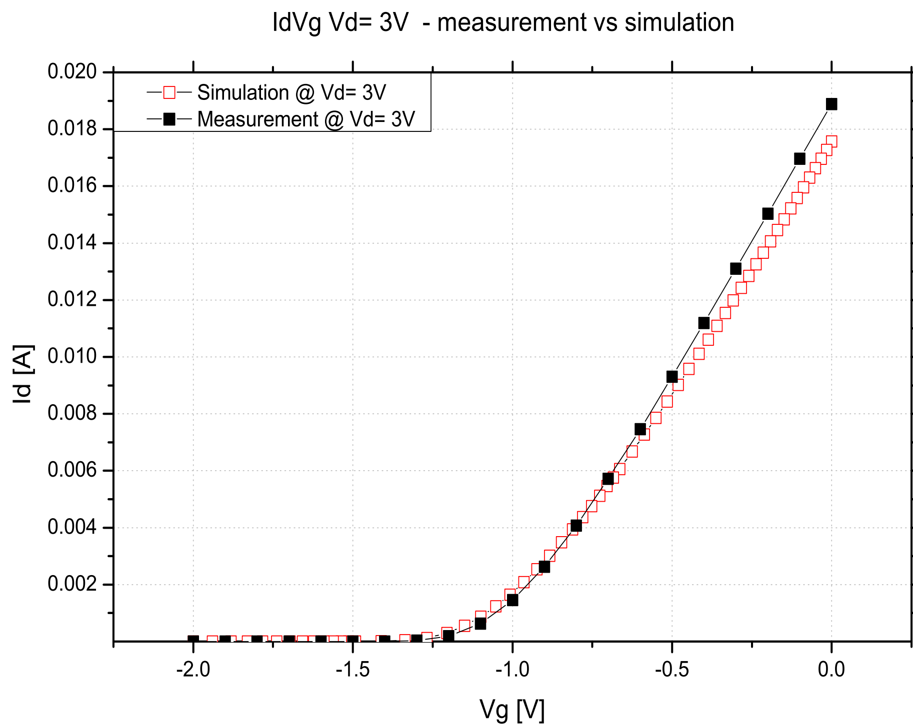

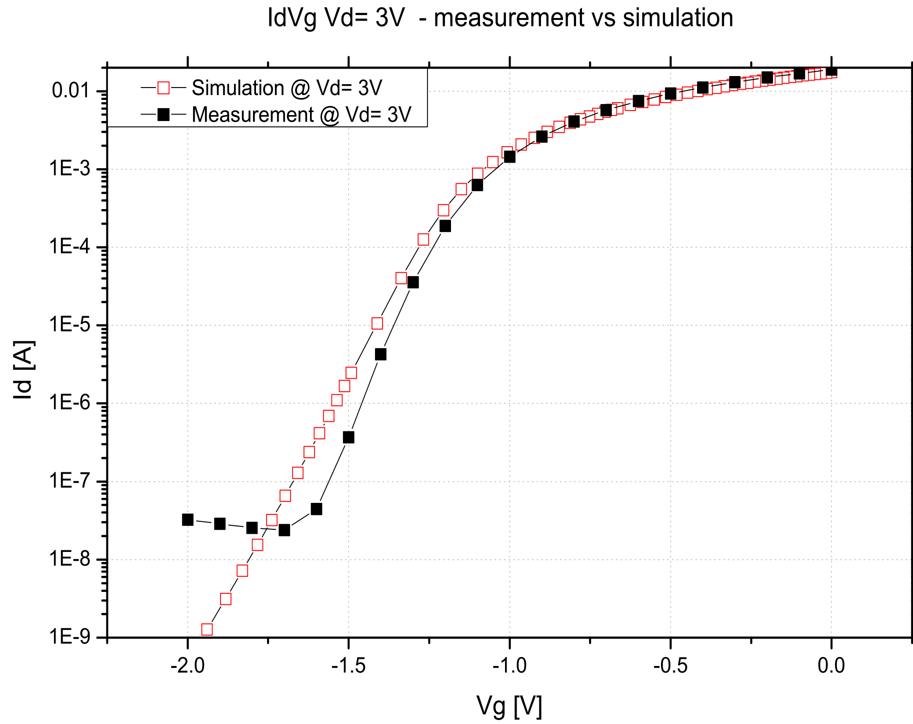

FIGURE 3.8: Comparison between simulation and measurement results for the first device. IdVg characteristic for $Vd = 3V$. ***top view:*** on state characteristics, ***bottom view:*** behaviour below threshold voltage.

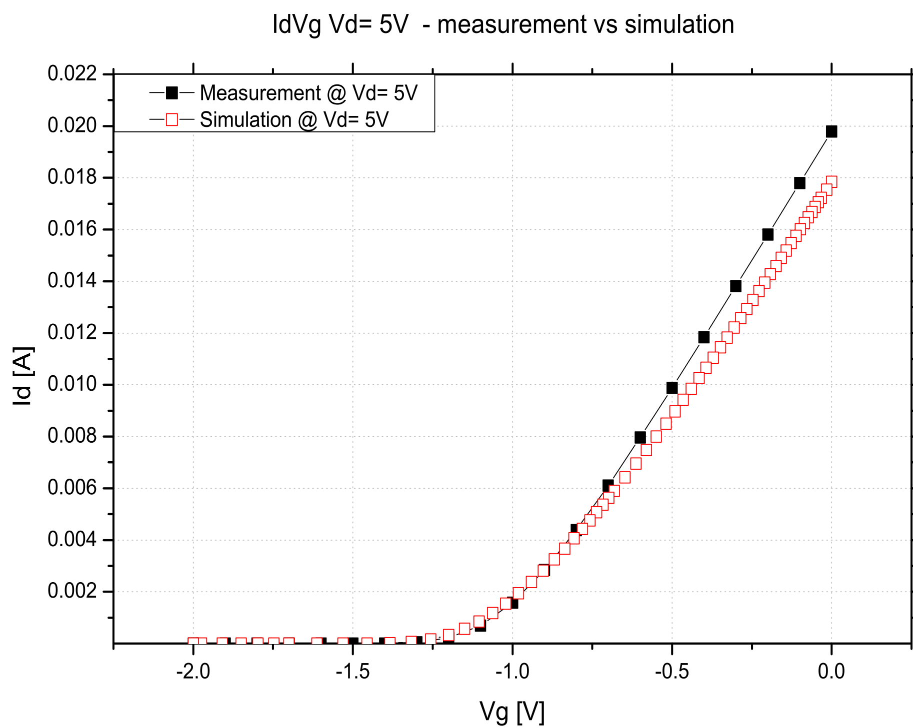

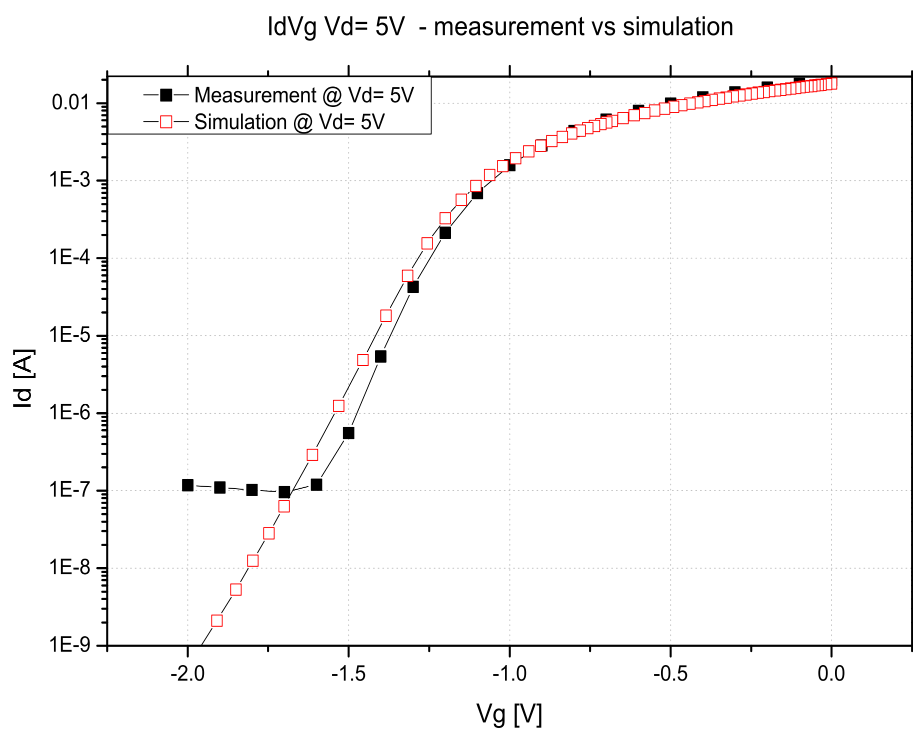

Figure 3.9: Comparison between simulation and measurement results for the first device. IdVg characteristic for $Vd = 5V$. ***top view:*** on state characteristics, ***bottom view:*** behaviour below threshold voltage.

Good fitting with the measurement data has been obtained, indeed we could fit very well both the on state characteristics and the region around the threshold voltage. For the off state characteristics instead, being the leakage not included in our model, some discrepancies are present between the simulations and the measurements.

As it can be seen from the images above, the threshold voltage of the device is below $0V$, meaning that the device is on even when $0V$ are applied to the gate. For this reason this device is *normally on* and this characteristic is due to the polarizations which create the 2DEG without any applied voltage to the gate. This fact could be a problem because it requires non zero voltage value for the off state, negatively impacting on the power consumption of the circuit in which the HEMT device is used, and it requires a more complicated driver which has to manage two non zero voltage values, one for the on state and the other for the off state, increasing the final cost of the project.

After the $IdVg$ simulations we run $IdVd$ ones as well, managing to obtain a good fitting (fig 3.10). The results so far explained prove the utility of the simulator for the obtaining of DC predictive results. For example it can be interested in normally off device, so a device with a threshold voltage greater or equal to $0V$. For this purpose it can vary the structure of the device and it can run the simulations in such a way to try to obtain a normally off behaviour, without physically process expensive sample devices.

3.2 Second device

The second device is the one in which we put most of our efforts. The only difference respect to the first one is the presence of the *Field Plate*. The Field Plate is an extension of the gate contact towards the drain region (image in fig. 3.11) in order to spread the electric field and hence avoid dangerous hot spots which could be the origin of the device failure. [4] Conventional metal semiconductor contact provides a potential weak point for III-N devices. Devices with conventional gates does not exploit the full basic breakdown properties of WBG semiconductors as the highly uniform field distribution provides early breakdown. For this reason the gate contact has been modified by the use of *gate extensions* and of field plates. The most important parameter apart from the gate length and the contact separation between source, gate and drain, are the length of the field plate (l) connected to the source or to the drain. Further the vertical height (t) above the semiconductor has a strong impact on the field distribution in the channel and in the barrier.

[29], [30] It is possible to anticipate qualitatively, several important trends in the behaviour of FP-HEMT as a function of the five variables, the insulator thickness (t), the

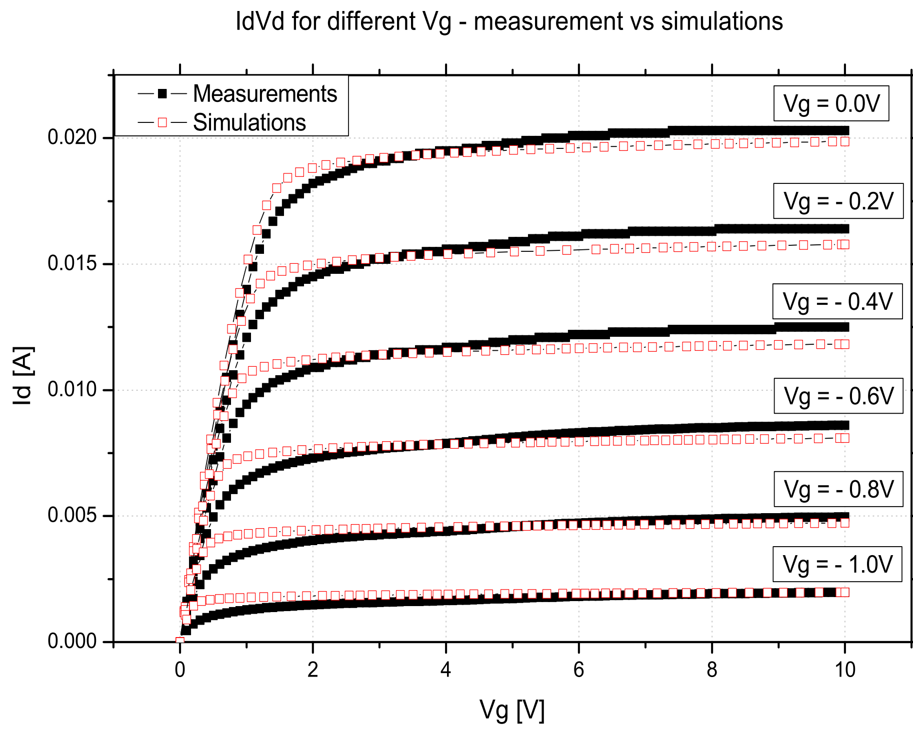

FIGURE 3.10: Comparison between simulation and measurement results for the first device. IdVd characteristic for various Vg.

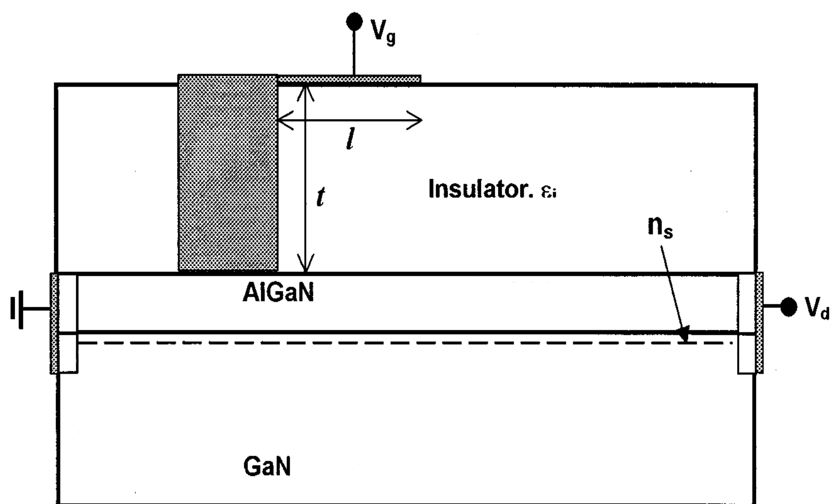

FIGURE 3.11: HEMT structure with Field Plates.

FP length (l), the insulator dielectric constant (ϵ), the gate to drain distance (L_{dg}) and the 2DEG concentration (n_s):

- Maximum will be obtained for an optimum t. This is because, for large t, the effect of FP vanishes and the field distribution consists of a single triangular lobe near the gate edge (see fig 3.11). For $t = 0$, the FP simply extends the gate by the FP length l, so that the field distribution is same as that for large t (but shifted to the new gate edge);
- This optimum t will increase with increase in ϵ (roughly $t \propto \epsilon$), because the FP influences the electric field along the 2DEG channel by a capacitive action;
- The optimum t will reduce with increase in n_s, on account of the same capacitive action and the fact that a stronger FP influence is required to manage a higher 2DEG concentration;
- The breakdown voltage (V_{br}) will decrease with increase in n_s. This corresponds to the situation in MESFETs in which decreases with increase in channel doping;
- The V_{br} will not increase for increase in l beyond a certain point. This is because, the field distribution along the 2DEG consists of two triangular lobes with peaks near the gate edge and the FP one (fig. 3.12). Further extending l could be possible to move the peak from the gate edge to the FP one.

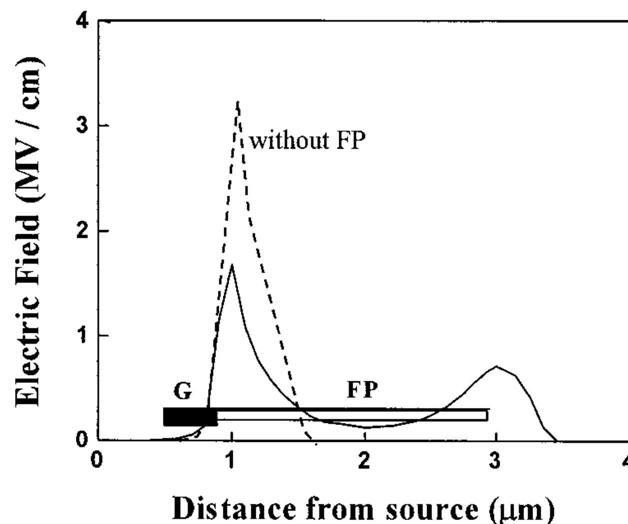

FIGURE 3.12: Distribution of the EF in an HEMT device. Difference between the one with FP and the one without it.

Drawback of the FP is the increment of the capacitance load at the gate and the relative decrement of the frequency *cut-off* (ft). However the influence in the ft lowering is not so heavy. Indeed the rate between the ft of the device with FP and the one of the device without it is quite close to 1 $(0.7, 0.8)$.

3.2.1 Device structure

The second device, object of our simulations, is the one depicted in fig. 3.13. As it can see, there are two field plates, one on the gate contact and the latter one above the insulator layer. Both of them have the aim to spread the electric field whom, otherwise, would be concentrated at the gate corner, providing a bad device reliability.

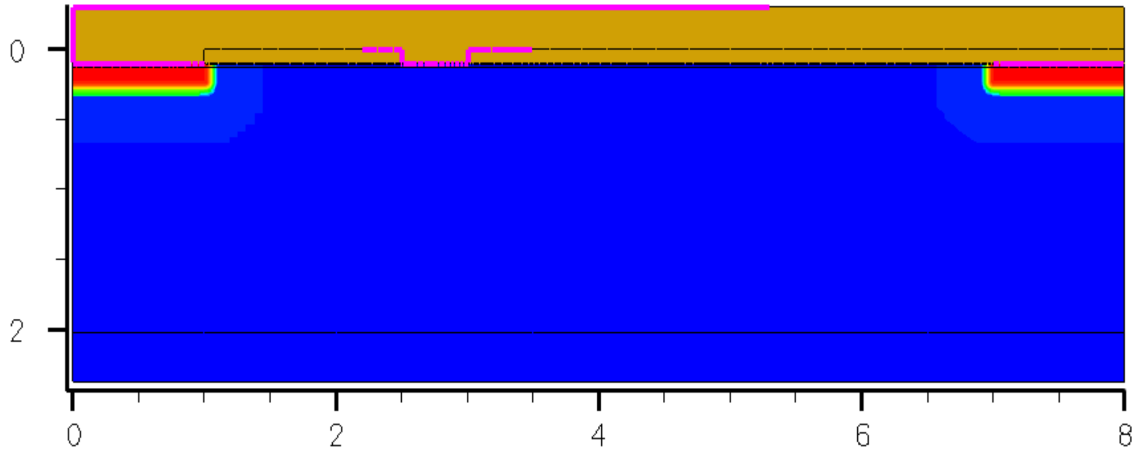

FIGURE 3.13: HEMT device structure for the second set of simulations implemented by Dessis tool.

It this case the mesh has been modified in such a way to put a thin mesh in the position of the possible electric field peak, i.e. below the field plates edges. In fig 3.14 it has been shown the two new meshes.

3.2.2 DC simulations

For the DC simulations we followed the same procedure of the first device. We firstly got the measurement characteristics and then we went on with the fitting of the $IdVg$ curve by varying the traps concentration. For this purpose we have to say that no important changes have been made for the traps characteristics respect to the deck used for the first device, indeed we moved the concentration from $3 \cdot 10^{17} cm^{-3}$, the supposed value of the first device, to $9 \cdot 10^{16} cm^{-3}$, value used in this device. Also the activation energy has been adjusted to $0.7eV$ from the CB instead of $0.8eV$ from the CB, value of the first device. These little variations are plausible since we are working on two different devices, produced with different growth processes by which traps with different features can be incorporated. To complete our deck we added the donor-like surface traps in the *passivation/cap* with a concentration of $2.55 \cdot 10^{13} cm^{-2}$ located at $1.5eV$ below the CB.

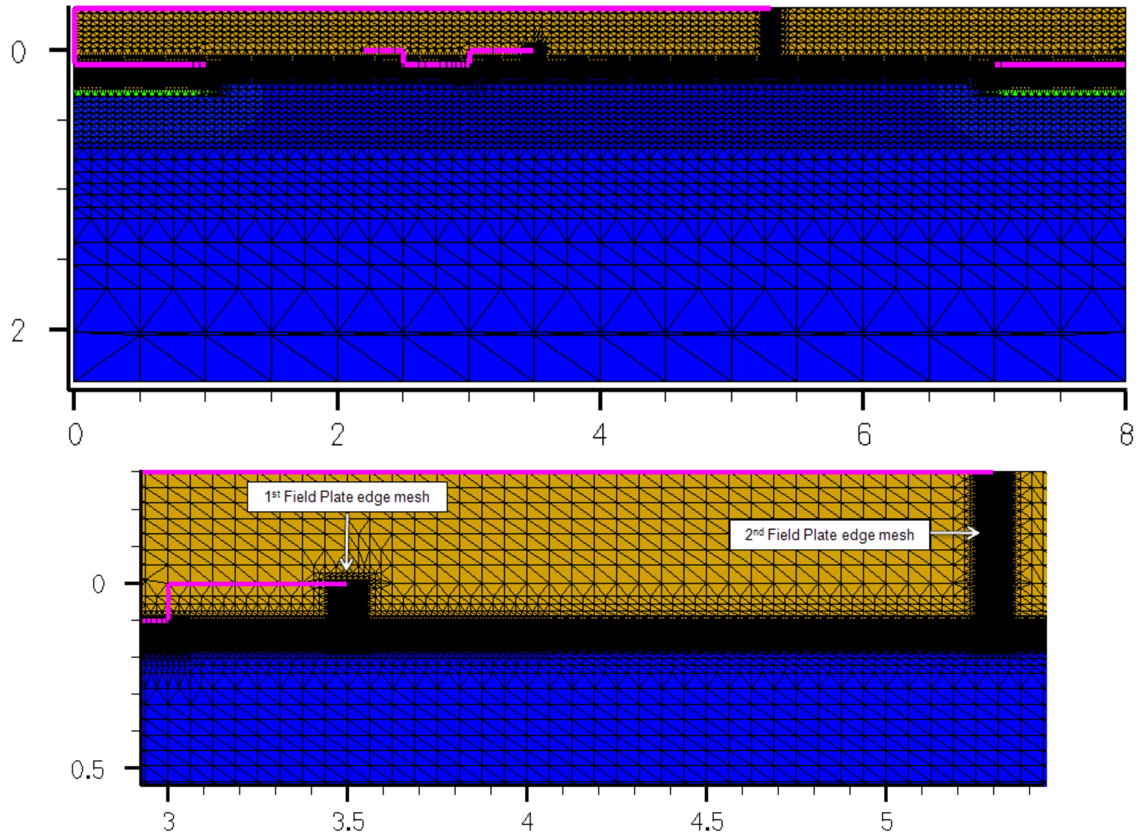

FIGURE 3.14: HEMT device structure for the second set of simulations with mesh included. ***top view:*** entire device, ***bottom view:*** zoom in the field plates region.

As it is depicted if fig 3.15, another time we managed to fit both the on-state $IdVg$ curve and the threshold value. Since the leakage model is not still included I stopped the simulation at $Vg = -2.5V$.

After the $IdVg$ curve we proceeded with the $IdVd$ ones. In fig 3.17 are showed the comparison between simulations and measurements. It is noticeable a good fitting mostly for the $Vg = -0.4V$ and $Vg = -1.05V$ curves. The simulated characteristic at $Vg = 0.25V$ is instead farther to the measured one, indeed while the measured curve starts bending after $Vd = 4V$, the simulated one keep going straight. This current decrement is due to the *self-heating* effect, by which the Id current has a negative slope. As reported in [31], DC characteristics of the high-power *AlGaN/GaN* devices are strongly negatively affected by self-heating, at high voltages and high currents regime. [32] The negative slope of the drain current is caused by an increment of the material resistance due to the increase of the device temperature. In fig 3.16 are depicted the channel resistance and the Id saturation current in function of the temperature. As it can see these two parameters have opposite trends, while one is increasing with T, the second one is decreasing. The thermal conductivity of the substrate should play a significant role in determining the temperature distribution in the epilayer structure and in the heat removal from the

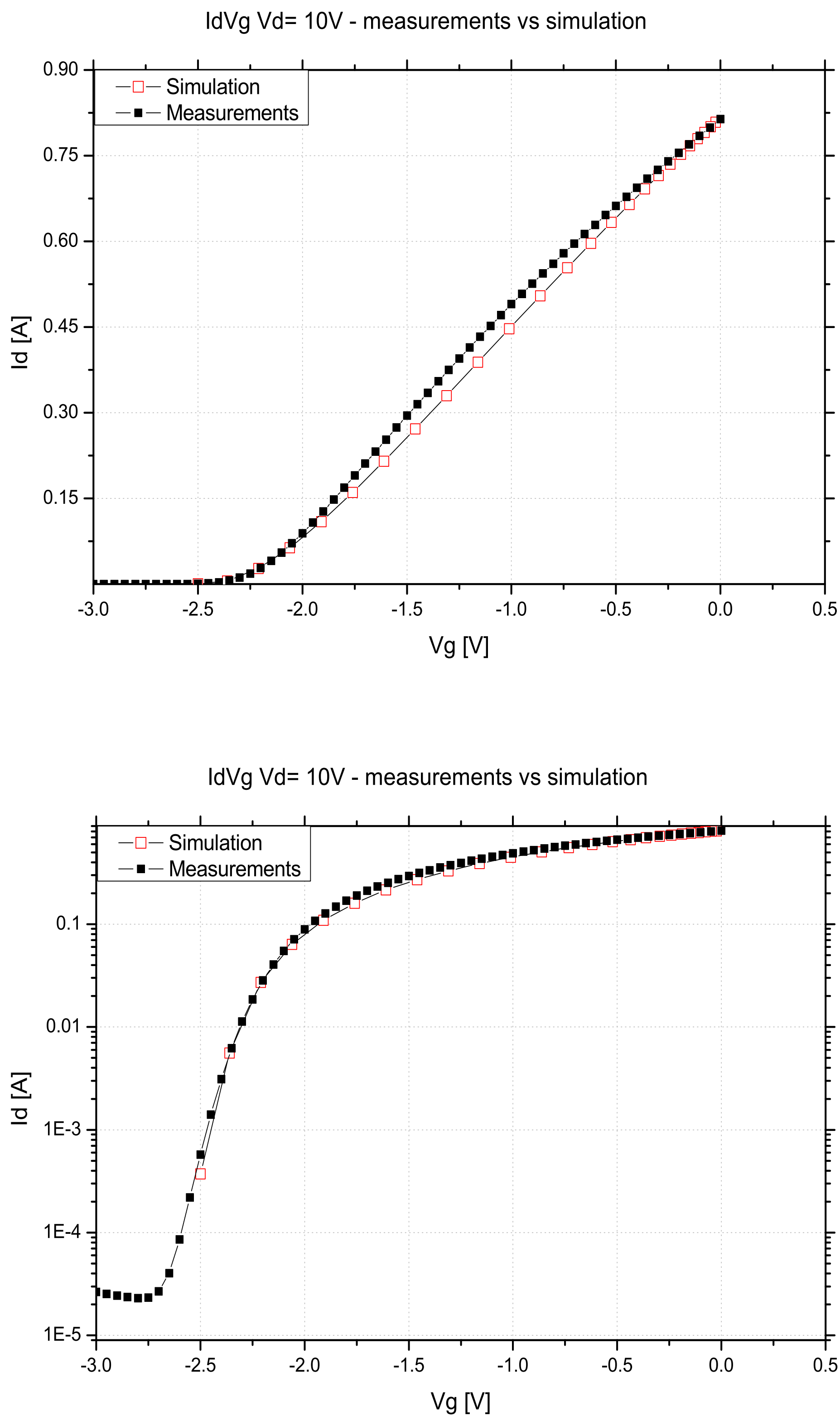

FIGURE 3.15: Comparison between simulation and measurement results for the second device. IdVg characteristic for $Vd = 10V$. ***top view:*** on state characteristics, ***bottom view:*** behaviour below threshold voltage.

active region of the device.

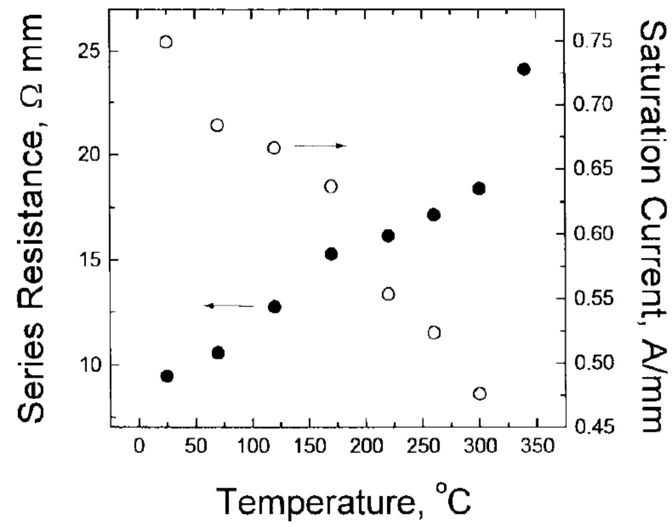

FIGURE 3.16: Effect of the self-heating on the drain current density and on the channel resistance.

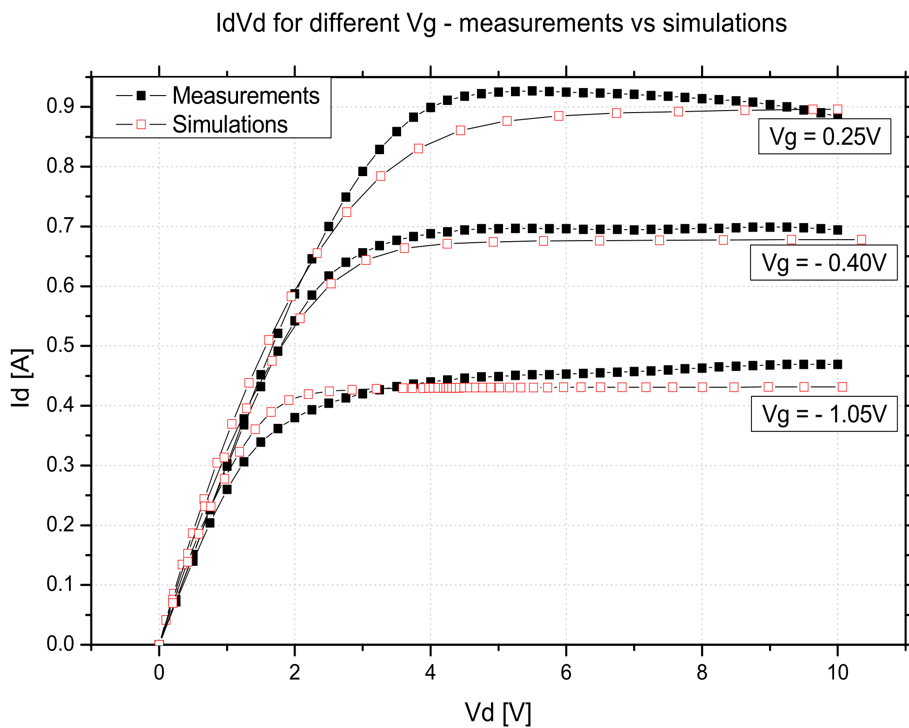

FIGURE 3.17: Comparison between simulation and measurement results for the second device. IdVd characteristic for various Vg.

3.2.3 AC simulations

Sentaurus software can run AC simulations as well as the DC ones, it has just to change the input file of the simulator. For instance, in our case, we were interested to gate capacitance simulations so we specified a final goal for the drain and for the gate voltages as well as the frequency we wanted the simulation to run. In this way the simulator provides to bias the device at the selected drain voltage, then it starts the sweep of the gate, starting form the initial value towards the goal one. For each point of the sweep the AC analysis is made.

[33] In any FET device, the charge density in the channel is opposed by charge of equal magnitude and opposite polarity on the gate terminal, forming the total gate charge, which itself is a function of the terminal voltages Vgs and Vds. Physically, the channel charge is distributed across the transistor gate length. In the equivalent circuit based modelling approach, the total gate charge is divided between (and attributed to) the gate-source and gate-drain terminals.

[34] The total gate differential capacitance may be obtained as

$$Cgg = \frac{dQ}{dVg} = \frac{d({Q_T}^+ + {Q_P}^+ - {Q_P}^- - {Q_T}^- - Q_{2DEG})}{dVg} \tag{3.1}$$

where Q is the total charge within the device and Vg the applied gate voltage. The total charge is composed of 5 terms: the positive charge due to ionized donor traps (${Q_T}^+$), the negative charge due to ionized donor traps (${Q_T}^-$), the positive polarization charge (${Q_P}^+$), the negative polarization charge (${Q_P}^-$), the negative charge in the 2DEG (Q_{2DEG}). Since the polarization charges are fixed, they does not contribute at the capacitance. If Vg is such that the Fermi level is well above the trap energy level, than all the traps are fully occupied and thus ${Q_T}^+ = {Q_T}^- = 0$. As V decreases, the Fermi level intersects the trap energy level (it is obvious that this intersection initially takes place at the *metal/cap* interface), the traps begin to empty and Q_T becomes nonzero. At the initial stage of emptying $dQ/d(Vg) > 0$ and thus an additional positive term appears in eq (3.1). This manifests itself as an increase in Cgg, in comparison with the situation when all the traps are fully occupied. However the main contribute is done by the charge in the 2DEG (Q_{2DEG}), in which the negative charge is modulated by the gate voltage.

In fig 3.18 is present a comparison between measured and simulated results obtained for the gate capacitance Cgg, sum of Cgd and Cgs. Both the curves have the typical characteristics to have two regions in which the $CggVg$ is flat and in between of them a rapidly change in Cgg occurs. [35] The Cgg drops as soon as the channel starts to deplete

due to the negative Vg and to keep decreasing as long as the channel is not completely empty. The voltage at which the capacitance starts decreasing is the threshold voltage. As it can be noticed there is a net difference in the Vth between the simulated and measured results. Indeed the Vth value in the simulated curve is around $-2.3V$, instead in the the measured one it seems the Vth to be around $-1.9V$, which means a positive shift of $0.4V$. If it has a look at the $IdVg$ charts, it can be seen that the measured capacitance has an higher threshold voltage respect to the measured $IdVg$. This could be related to the fact that during the characterization process current collapse occurred, meaning that the 2DEG has been depleted and hence leading to a Vth shift. Apart from that the amplitude of the capacitance change that results form our simulation is comparable with the measured one.

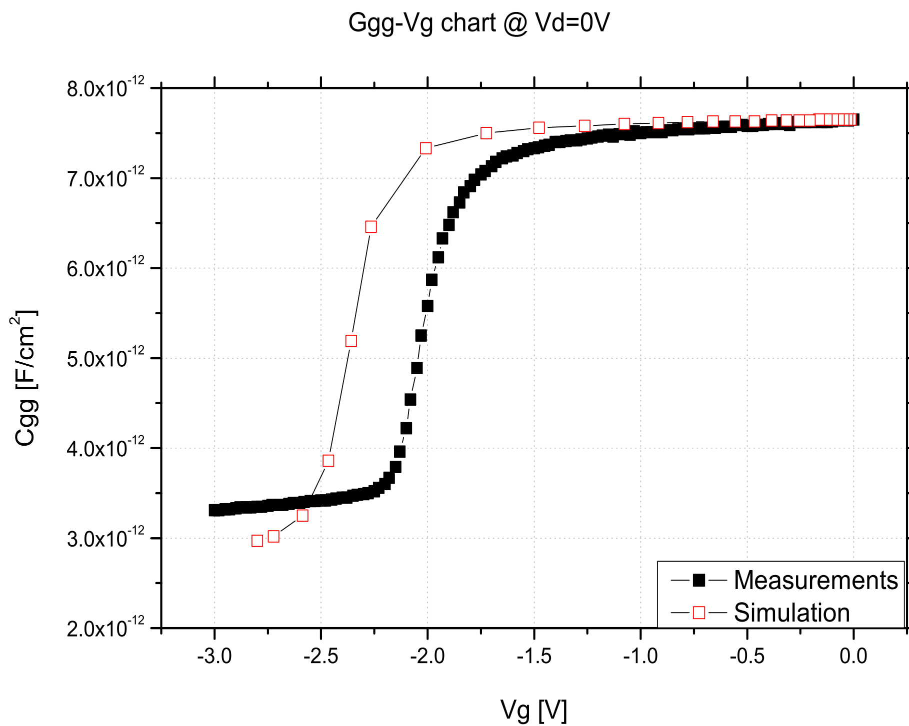

FIGURE 3.18: $Ggg - Vg$ for $Vd = 0V$. Comparison between simulation and measurement results for the second device.

During the capacitance simulation it has to be sure that the frequency used for the AC is not too high because it could happen that the charges do not follow the gate voltage. Indeed since the electric field is low because usually no drain voltage is applied, also the carriers velocity will be low, with the result that they take more time to respond to a voltage AC stimulus. So, the use of high frequency will lower all the upper part of the the capacitance simulated characteristic.

With our model we could match not only DC characteristics but capacitance one as well. This could be useful when it wants to check the capacitance load of the device especially when it is used in RF applications, field in which parasitic capacitance slows down the velocity of whole the circuit. The capacitance evaluation can help the calculation of the power consumption of the circuit and to find a way to reduce it.

3.2.4 Gate Leakage

[36], [37] In literature it has been noticed that leakage effect is strongly present in HEMT devices, as reported in various paper. It has just to have a look at the $IdVg$ measured characteristics in fig. 3.6 - fig 3.9 of the first device and fig 3.15 related to the second one, to realize that the drain current does not keep decreasing, rather it starts increasing after a certain gate negative voltage. This behaviour means that the leakage mechanism in ongoing, i.e. there is a parasitic current flowing to the drain. Minimizing the off-state leakage current in HEMT devices is essential to their incorporation into circuits and systems in which low noise and low power consumption are important considerations. [38], [39] In some cases it has been reported a very high leakage current of $10^{-4} A/mm$. There can be two causes for the leakage, *vertical transport* through to the Schottky interface and *lateral electron injection* to the surface from the gate edge. In fig 3.19 are depicted both the possible leakage mechanisms. While the latter contribution is easy to remove by passivation with a dielectric, the former one is difficult to avoid. According to some studies, the results show the important effect of the gate leakage current in the performance of *AlGaN/GaN* HEMTs and the importance of using high-quality gate dielectrics, such as Ga_2O_3 or SiN, to reduce the gate leakage current.

Among the causes which could induce the leakage, it seems that the direct gate leakage current is the main contributor to the observed leakage from the drain terminal. That's why we decided to take into account only the vertical leakage in our simulations.

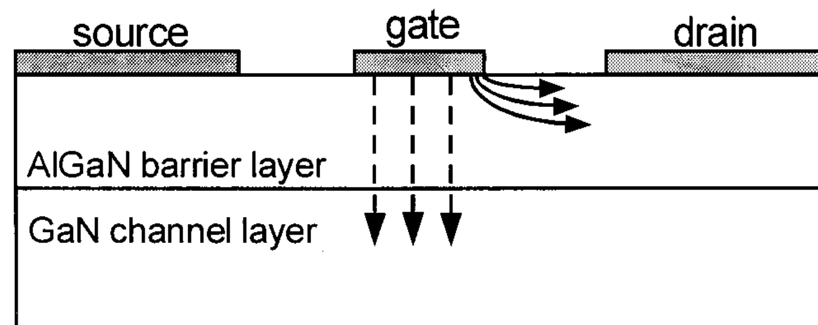

FIGURE 3.19: Leakage mechanisms in HEMT device. The structure illustrating vertical (dashed lines) and lateral (solid lines) tunneling current leakage paths for the gate-drain current.

Studies reported that the etching process in *GaN*-based devices produced traps, causing an increased leakage current. Indeed, it was found that the defect charges around the gate finger could result in barrier narrowing in the *AlGaN* cap layer, leading to increased gate leakage current. [40] At this purpose Fang et all. analysed the etching effect on the traps presence in a *GaN* sample by using *deep-level transient spectroscopy* (DLTS). In their work they found an enhancement of *N*-vacancy near the etched surface, meaning that surface donors are introduced.

In order to overcome this problem, beside the top device passivation with dielectric material, [36], [38] another technique has been used. It has been found that including a *GaN* cap layer on top of the standard *AlGaN* barrier can increase the HFET peak barrier height. This strategy yielded a large reduction in gate leakage current compared to that in a conventional HFET without the *GaN* cap layer.

Other cause of the presence of traps could the stress that the gate edge undergoes because of the high electric field. Indeed in the gate edge close to the drain region is the point in which the maximum electric field is present. As I reported in chapter 2.6, J.A. del Alamo and J. John claim that in an *AlGaN*/*GaN* HEMT under high voltage operation, a large electric field appears under the gate edge across the barrier. This can result in very large mechanical stress concentrated in a very small region of the *AlGaN* barrier. Under electrical stress, the elastic energy in the high-field region increases on top of this. If the elastic energy exceeds a critical value, crystallographic defects are formed. These defects are electrically active and affect the device characteristics in a profound way.

Since it seems there are traps beneath the gate area, we added a layer of donor traps just below the contact in our structure, as it can see in fig 3.20 where it is showed the added donors layer in a zoom of the gate region. This because, as it has been said above, the donor layer might modify the band diagram by narrowing the barrier.

In order to simulate the leakage we added the *non-local mesh*, a particular additional mesh required for the leakage model we used: *the non local tunneling.* With the non local mesh the simulator draws specific lines that represent the tunneling path for the carriers that are moving from the gate towards the 2DEG.

Firstly we analysed the influence of the traps concentration, keeping the activation energy of $0.1eV$ from the CB and the electron cross section of $10^{-15}cm^2$. The simulations results 3.21) follow what we found in literature, that is increasing the traps concentration the conduction band lowers and this barrier lowering leads to a barrier narrowing, allowing the electrons to tunnel through the *GaN* layer. From the image it seems that there is a sort of threshold value, below which no important effect can be seen. Indeed no modifications in the band diagram are present for concentration below $10^{20}cm^{-3}$ and

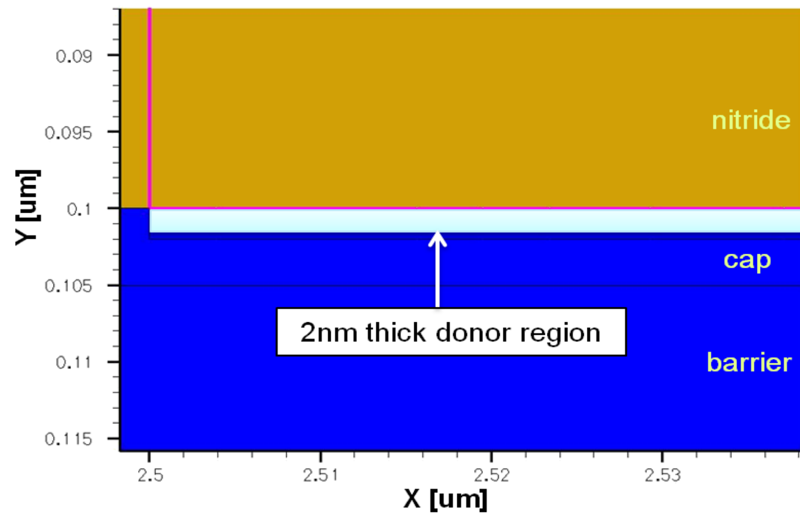

FIGURE 3.20: Zoom of the gate edge area.

for concentration greater or equal this threshold value, the bands start bending. With a donors concentration of $10^{21}cm^{-3}$ an electron driven by the electric field can tunnel much more easily than in the case of lower donors concentrations. In the illustration it can also notice that for high concentration the band in the 2DEG region is modified and we can expect a changing in the $IdVg$ on-state characteristics.

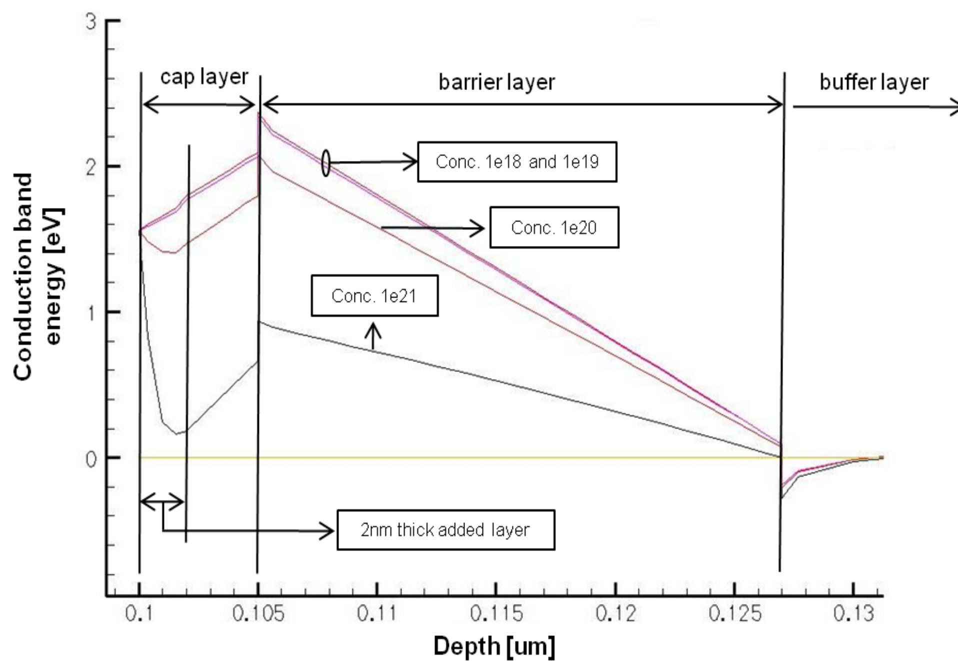

FIGURE 3.21: Conduction band diagram for various donors concentrations.

Analysing the $IdVg$ simulations (fig 3.22) it results that the leakage is ongoing as soon as the gate voltage reaches a certain negative value (around $-2.75V$). It can be noticed that unlike we expected, the on-state (top view) does not change heavily even if the

2DEG increased after the addition of the new layer. Also the threshold value does not shift leftwards, as we could expect when the 2DEG population increases. This is due to the fact that increasing the donors concentration, increases the number of free electrons because the shallow donors tend to be ionized and hence they tend to loose electrons. These electrons can be captured by the acceptor traps in the $AlGaN$ layer, lowering the amount of positive charge needed for sustain the 2DEG. This mechanism explanation is corroborated by the fig 3.23 in which it is showed that the amount of electrons taken by the $AlGaN$ traps raises with the increment of the free electrons.

After changing the concentration, we attempted to vary the traps activation energy from the CB and we got the results depicted in fig 3.24. In these results it can be noticed that the leakage current is greater for low activation energy and lowers increasing the energy value. The explanation of this effect is that rising the traps energy level less traps are ionized, as it can be seen by fig 3.26. In this image indeed, where the conduction band for different traps activation energies is showed, it can be understood that an increment of the energy level results in an upward movement of the conduction band. This means that the barrier thickness improves and less electrons can cross the barrier. In the $IdVg$ diagram it can see that no changes in the on state characteristics is produced because the 2DEG concentration does not vary, as it is showed in fig 3.26.

The proves that the leakage is ongoing in our simulations are not only present in the $IdVg$ characteristics, as we showed before. The image 3.27 represents the electron density in function of the device depth both for the tunneling model on and off. As it can see the difference in density between the two simulation results is about 10 orders of magnitude. Another prove is reported in fig 3.28 by the current vectors for $Vd = 0.1V$ and $Vg = -5V$. From this figure it is evident that the current vectors are present only in case of tunneling model turned on (left image) while no current vectors are present in the simulation result without this model active (right view). These vectors are pointing towards the gate, meanining that electrons are crossing the barrier.

As it can be seen TCAD platform can be suitable for the leakage study as well, as it has been testified by the simulation results just displayed. By these simulations we showed that it is plausible that etch process damage the gate surface in such a way to produce donor traps which modify the band diagram and hence allow the current leakage. In order to use improve the leakage in our model we used a non local mesh in the gate region. This added mesh, according to the guide, should get worse the deck convergence and should increase the simulation time. Fortunately this did not happen, indeed we managed to vary both the traps concentration and their activation energy without any bad impact on the simulation convergence and simulation time.

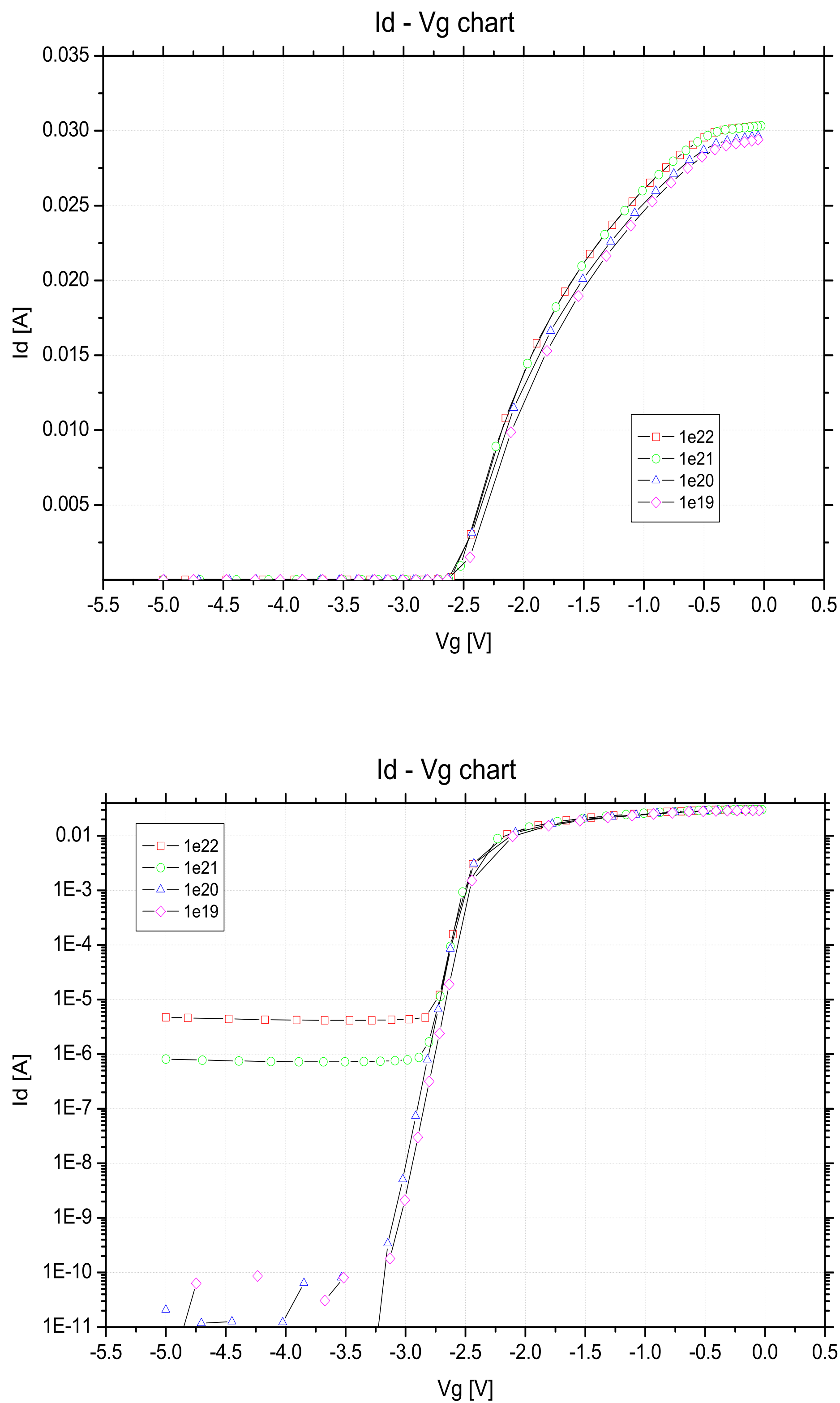

FIGURE 3.22: Comparison among simulation results with different concentrations of donor traps. $IdVg$ characteristic for $Vd = 0.1V$. ***top view:*** on state characteristics, ***bottom view:*** behaviour below threshold voltage.

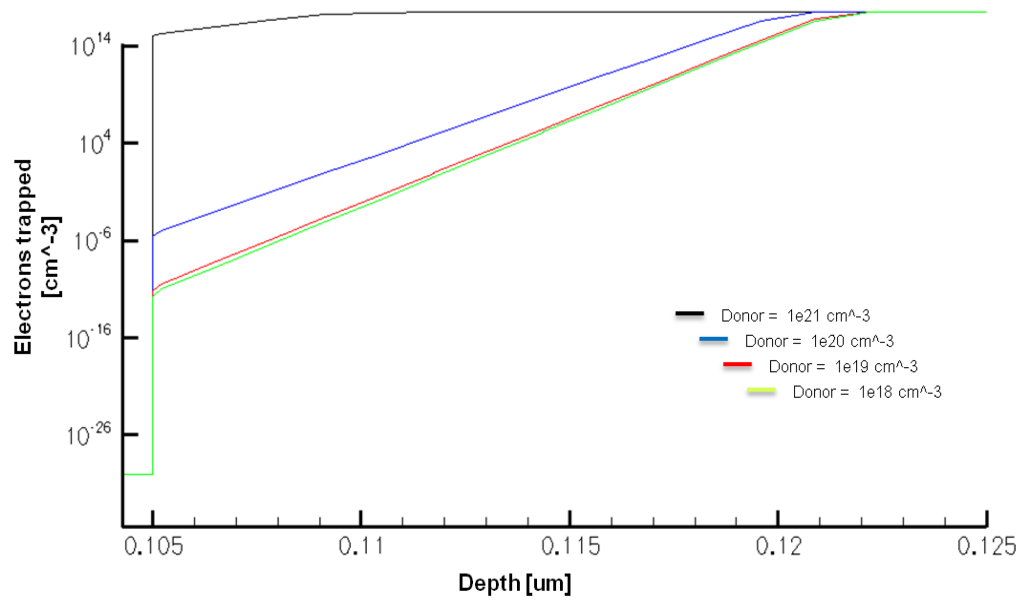

FIGURE 3.23: Trapped electrons function of the depth of the device.

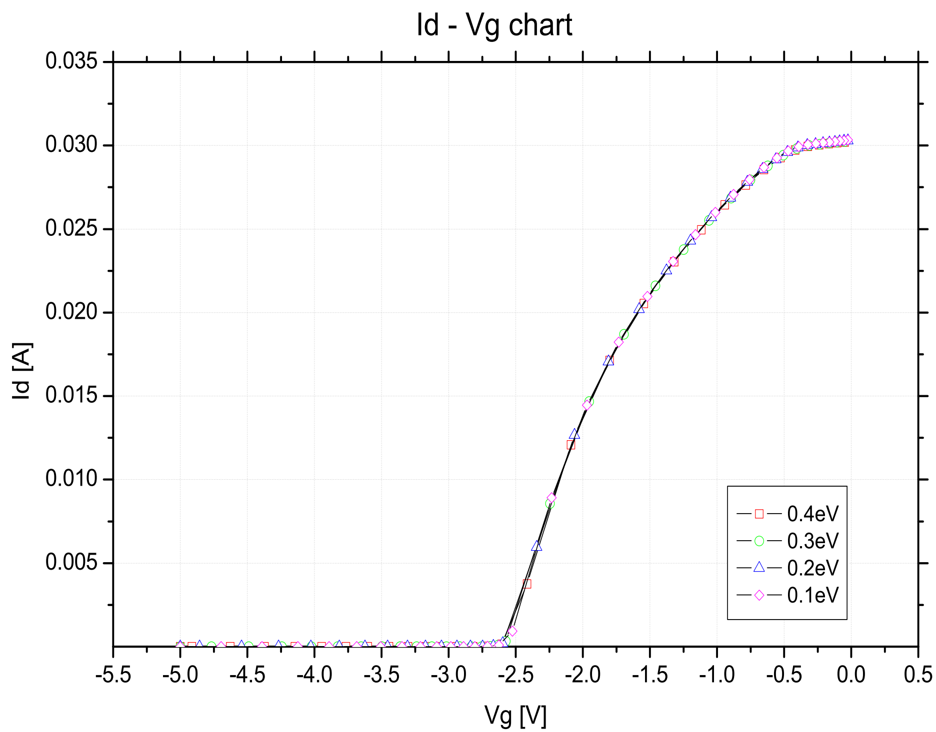

FIGURE 3.24: Comparison among simulation results with different traps activation energies. $IdVg$ characteristic for $Vd = 0.1V$. ***top view:*** on state characteristics, ***bottom view:*** behaviour below threshold voltage.

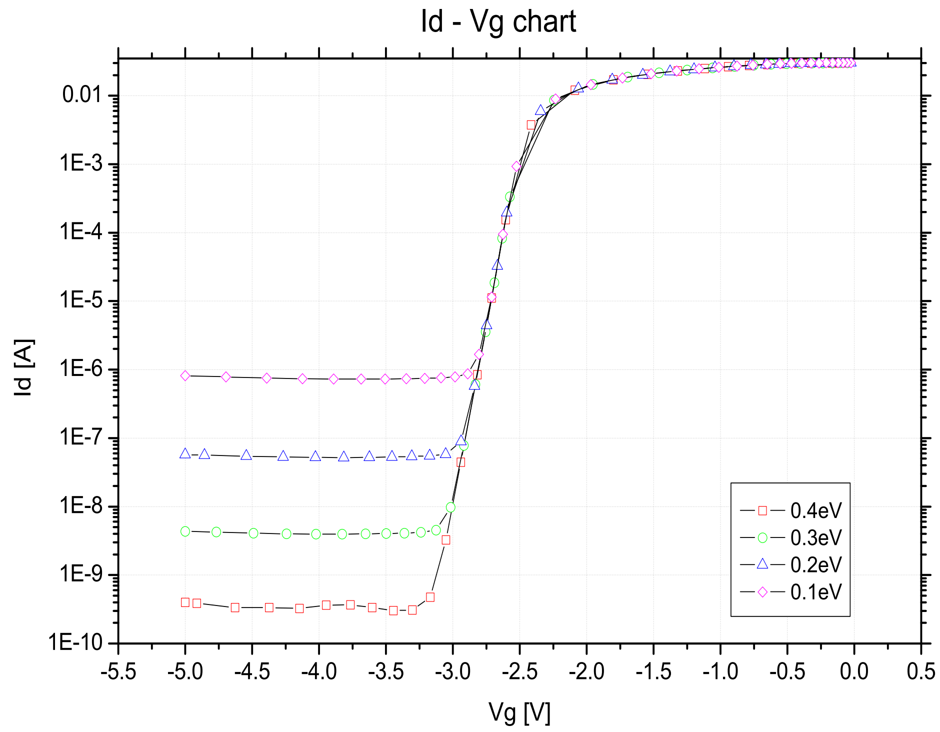

FIGURE 3.25: Comparison among simulation results with different traps activation energies. $IdVg$ characteristic for $Vd = 0.1V$. ***top view:*** on state characteristics, ***bottom view:*** behaviour below threshold voltage.

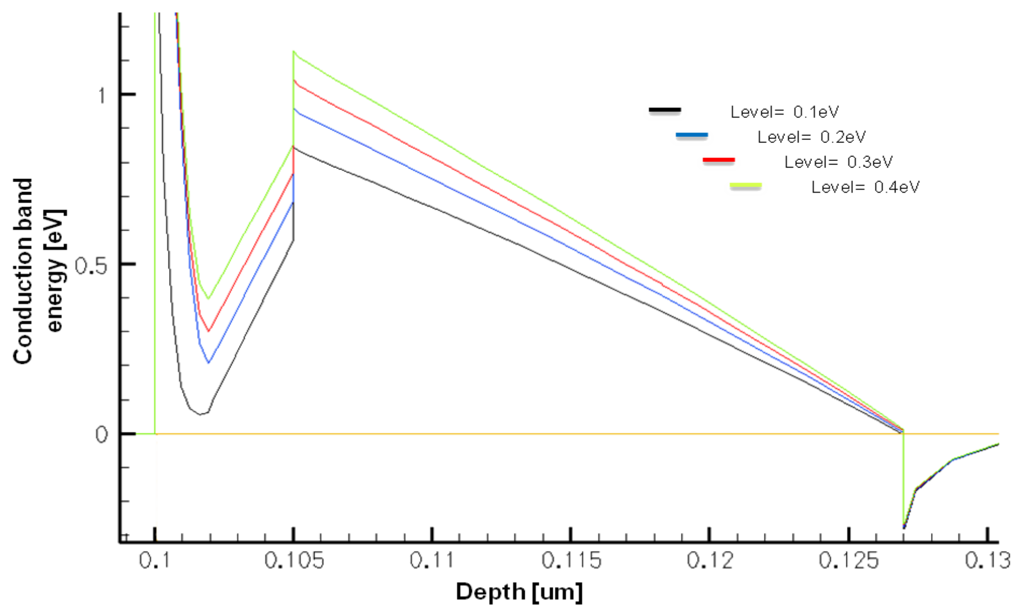

FIGURE 3.26: Conduction band for different activation energies at $Vg = 0V$.

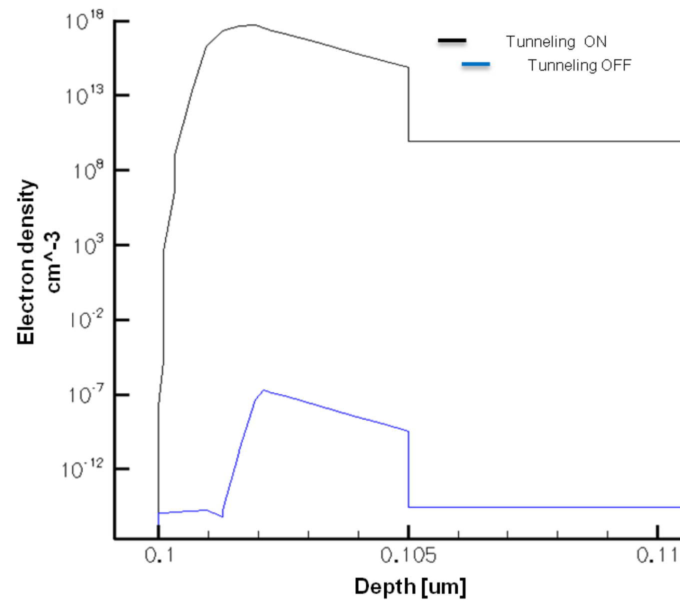

FIGURE 3.27: Electron density for tunneling model turned on and off. Simulation results for $Vd = 0.1V$ and $Vg = -5V$

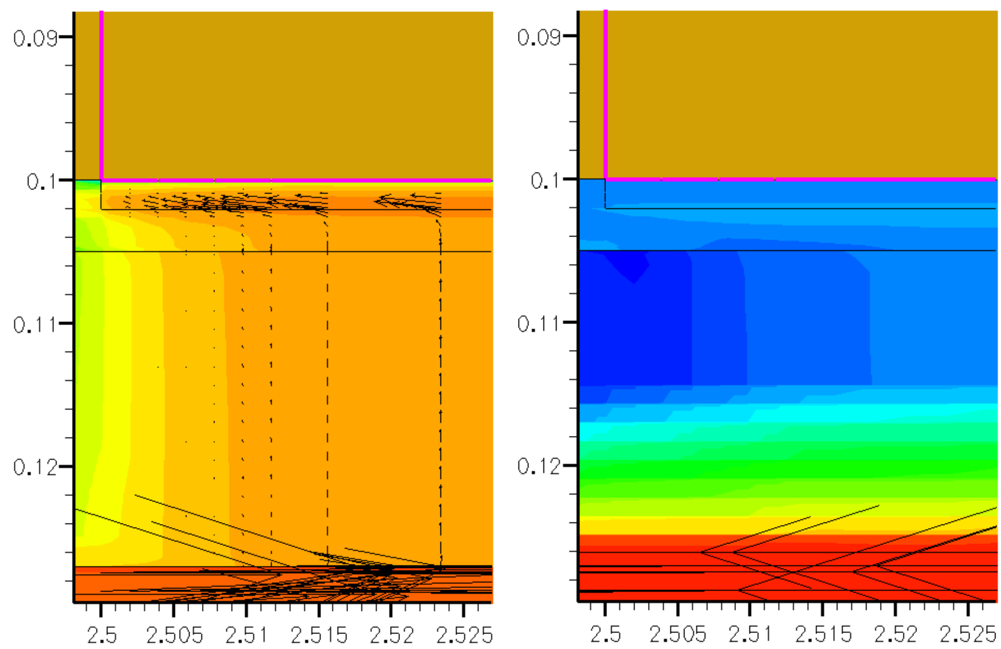

FIGURE 3.28: Current vector comparison for . $IdVg$ characteristic for $Vd = 0.1V$ and $Vg = -5V$. ***left view:*** tunneling model ON, ***right view:*** tunneling model OFF.

3.2.5 New mobility model

It is well known that GaN, unlike Si has a different bands diagram, i.e respect to the silicon, material with indirect bandgap (fig 3.29 left), gallium nitride has a direct bandgap (fig 3.29 right).

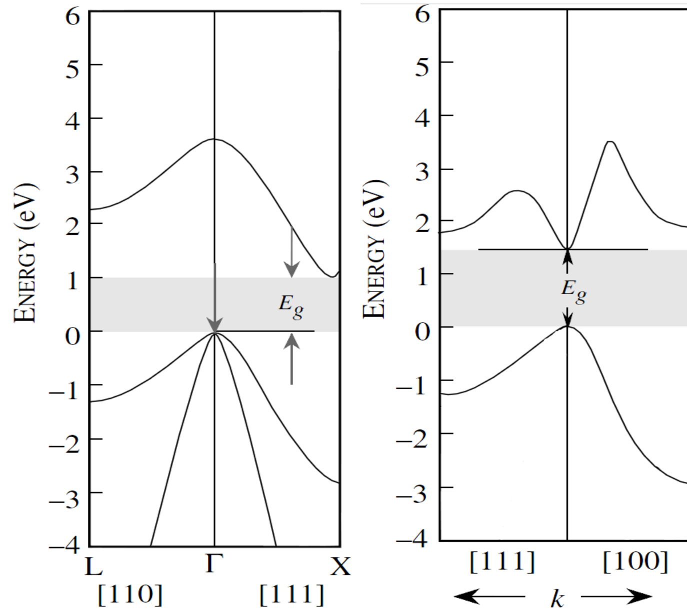

FIGURE 3.29: Comparison of different types of bandgap. ***left view:*** indirect bandgap, ***right view:*** indirect bandgap.

It is typical for the direct band gap materials to have a different mobility which includes a negative differential region, as it has shown in fig 3.30. Looking at this image it can immediately recognize the difference in the velocity trend between Si (in the inset), in which the velocity saturates for a certain value of the electric field and stays at the same value even increasing the electric field, and GaN, in which after reaching a maximum level the velocity starts decreasing. The negative differential velocity is present because as soon as an electron, moved by the high electric field, is carried out from the tight valley at the minimum of the CB to a wider one, the electron increases its relative mass and then its mobility decreases.

The implementation the new mobility model has been possible by means a $C{++}$ interface in which we wrote the new mobility formula and its derivative with respect to some parameters like lattice temperature, carriers density, electric field, and few others. In order to implement the new model we had to follow the template in the guide. In fact, the only way to write a new model is using the templates which are already present in the guide. At this purpose we took as reference the High-Field Saturation model and we wrote in it the formulas (3.2) written below and its derivatives. Then we took the template for the low field mobility and we included in it the formula (3.3) in the same

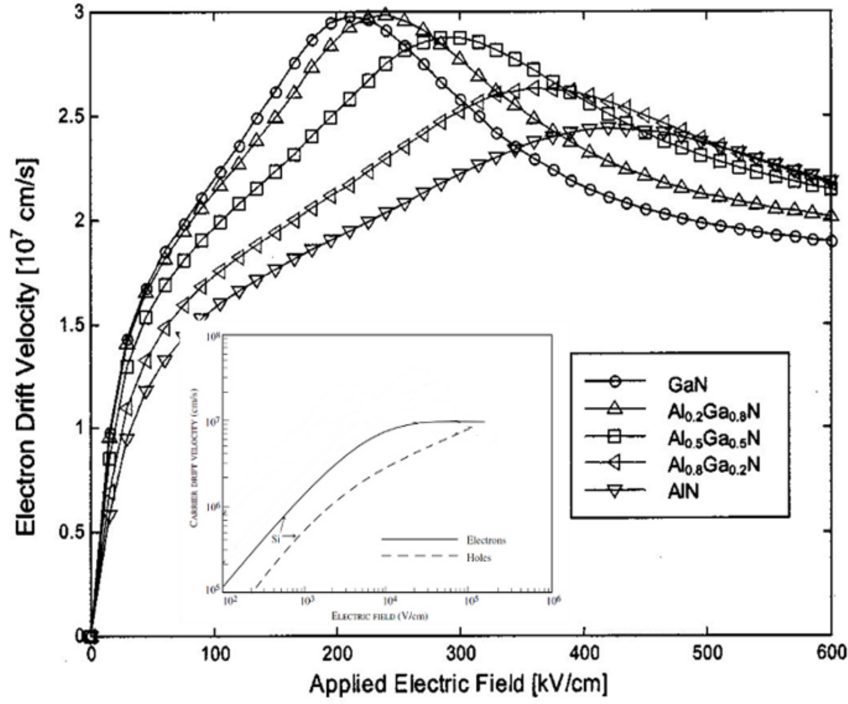

FIGURE 3.30: Electron velocity of GaN and $AlGaN$ materials in function of the electric field. ***Inset***: carrier velocity in Si

way as we did with the high field one. In the the appendix A.3 it can find the models implemented. The $C++$ file needs a compiler to let the simulator to use the model so we added to our simulator deck $TCLSH$ compiler, a TCL interpreter.

[41] The mobility model we implemented, found by Farahmand et al, is based on the following formula:

$$\mu = \frac{\mu_0(T,N) + v_{sat}\frac{E^{n1-1}}{{E_C}^{n1}}}{1 + a\left(\frac{E}{E_C}\right)^{n2} + \left(\frac{E}{E_C}\right)^{n1}} \tag{3.2}$$

where

$$\mu_0(T,N) = \mu_{min}\left(\frac{T}{300}\right)^{\beta 1} + \frac{(\mu_{max} - \mu_{min})\left(\frac{T}{300}\right)^{\beta 2}}{1 + \left[\frac{N}{N_{ref}\left(\frac{T}{300}\right)^{\beta 3}}\right]^{\alpha (T/300)^{\beta 4}}} \tag{3.3}$$

In (3.2) μ_0 is the low field mobility, as expressed in (3.3), and E is the electric field value. There are five parameters in the new model, which are determined from a least squares fit to the results of Monte Carlo simulation. These parameters are the saturation velocity v_{sat}, the electric field value of the max velocity E_C and the fitting parameters a, $n1$, $n2$. In (3.3) T is the temperature, N is the total doping density, μ_{max} and μ_{min}

are the mobility and α, $\beta1$, $\beta2$, $\beta3$, $\beta4$ are fitting parameters obtained by Monte Carlo simulations. The fitting parameters values can be found in the relative paper.

With this new mobility model we got the results showed in fig 3.31 for the $IdVg$ characteristic and in fig 3.33 for the $IdVd$ one. It is obvious that no improvements have been brought form this new model respect to the old one. The difference form simulation results using the new model and the ones obtained by using the old model is quite evident. Moreover the time consuming is very high, about 10 times more than the standard model and we had by far more convergence problems. Because of these reasons we decided to keep using the old mobility model.

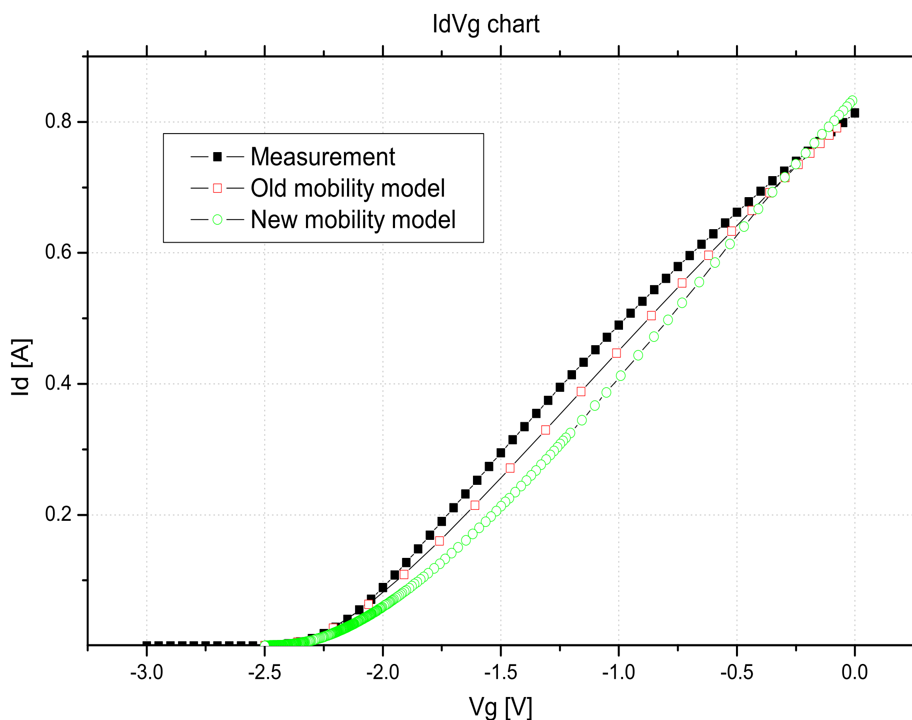

FIGURE 3.31: Comparison among simulation and measurements results with different mobility model. $IdVg$ characteristic for $Vd = 0.1V$. On state characteristics.

Even if we did not get any improvements buy using this model, we proved that it is possible to include a new physical model. We included a new mobility model but the same approach can be used to write a new recombination model or a new avalanche model or few others. It has just to respect the template which can be found in the guide. The necessity of implementing a new physical model could derive from the fact that most of the physical models already included in the simulator have been calibrated for *Si* and for few others well known materials, but not for the newest ones, like *GaN*, *AlGaN*, *InGaN*, ...

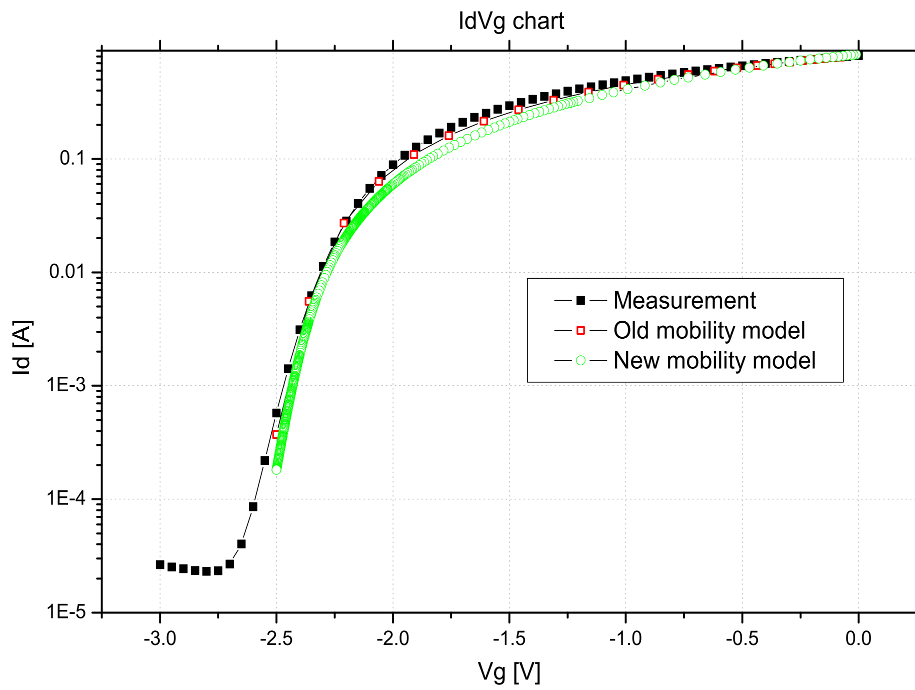

FIGURE 3.32: Comparison among simulation and measurements results with different mobility model. $IdVg$ characteristic for $Vd = 0.1V$. Behaviour below threshold voltage.

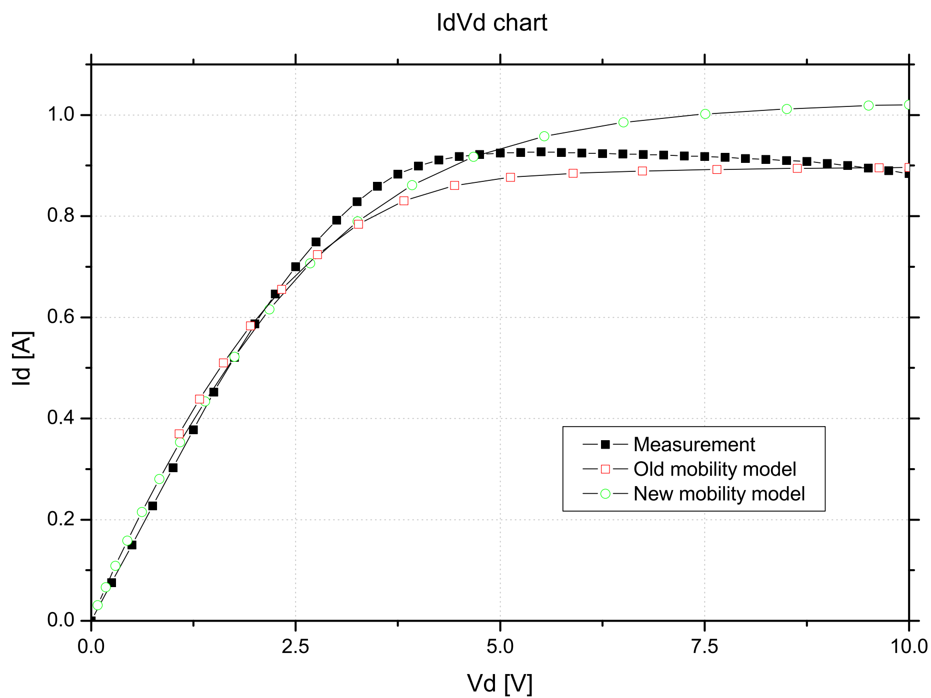

FIGURE 3.33: Comparison among simulation and measurements results with different mobility model. $IdVd$ characteristic for $Vg = 0.25V$.

3.2.6 Electric Field evaluation

Electric field evaluation is very important for reliability study since this kind of device is suitable for high voltage applications. This study consists of seeing the point where the maximum electric field is located and finding a way to lower it, in order to improve the system reliability. One way to do that is by the Field Plate, an extension of the metal contact towards the drain region which can spread the electric field that otherwise would be concentrated beneath the gate edges. If it manages to spread the EF along the channel the *avalanche* phenomena moves to higher voltage. The avalanche is a mechanism by which a carrier driven by the electric field can be multiplied because of the *impact ionization* which take place only whether the carrier energy is high enough. The carriers responsible of the avalanche could come from the gate or [42] they could be created by a band to band tunneling, when the bend bending is sufficient to get close the conduction band and the valence one in such a way to allow a carrier to pass through the barrier as it is depicted in fig 3.34. [43] Another way to improve the BV involves increasing the gate-drain distance. However, this increases the drain series resistance and hence degrades the power performance of the devices. Furthermore, increasing the gate-drain distance only works up to a certain distance, beyond which an additional increase in the distance will not further improve the breakdown voltage rather it will increment the channel resistance.

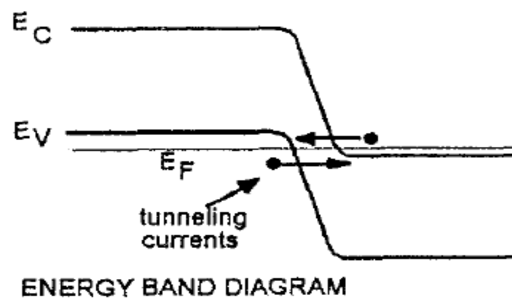

FIGURE 3.34: Band to band tunneling mechanism depiction.

In order to study the electric field distribution within the device, simulations with different FP lengths have been carried out and the EF has been evaluated in various sections of the device. Before that we needed to check if the electric field was properly distributed within the device, i.e. with the maximum electric field below the gate edge. Since it was not well distributed we incremented the thickness of the nitride on top of the device. This leaded the maximum electric field to move from a certain point away from the gate to the region beneath the gate edge, like it should be because of the presence of the gate corner. This behaviour can be seen in fig 3.35, where the thickness has been incremented from $0.3um$ to $1.2um$ leading, in the latter case, to a wiser distribution of the EF. These simulations have been run with a gate voltage below the threshold ($Vg = -2.7V$) and

a $Vd = 20V$. For this set of simulations we included the avalanche model as well. The band to band tunneling has not been inserted because it worsens the convergence of the simulations.

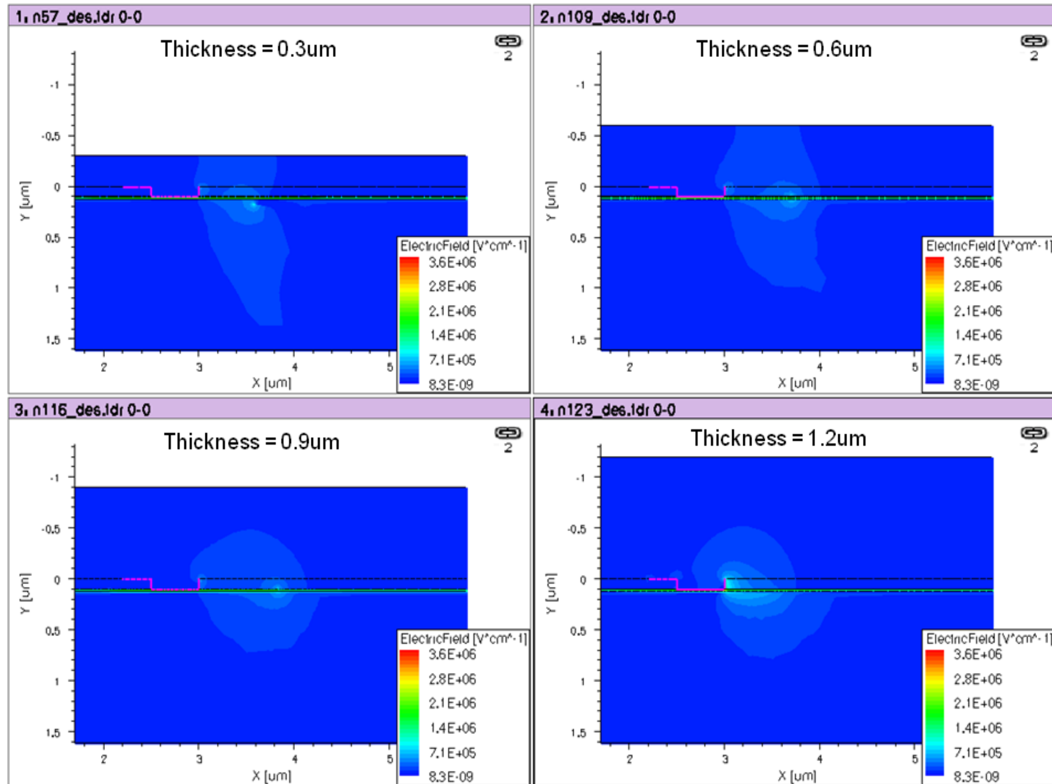

FIGURE 3.35: Effect of the Nitride thickness on the Electric Field distribution for $Vg = -2.7V$ and $Vd = 20V$. Zoom in the gate area.

Having a look at the cut in the 2DEG region (fig 3.36), it can see that the electric field distribution along the channel is not so straightforward for thickness less than $1.2um$. In fact only in the $1.2um$ result the EF peak is located just below the gate edge at $X = 3.0um$, as it should be. In the other cases instead the peak is present in a region at $X = 3.6um$.

A reasonable electrostatic potential has been obtained as well with a thicker Nitride, as it can notice in fig 3.37. In this image it sees that for a reduced thickness the potential starts dropping around $X = 3.6um$, the point where the maximum EF is concentrated. Only in the last case the EP decreases in a region close to the gate edge, meaning that a 2DEG depletion is occurring only there. It has to be noted that the potential does not drop nearby the drain contact because the 2DEG concentration is not heavily modified by the gate and the drain voltage. Indeed the depletion is taking place only in the area underneath the gate.

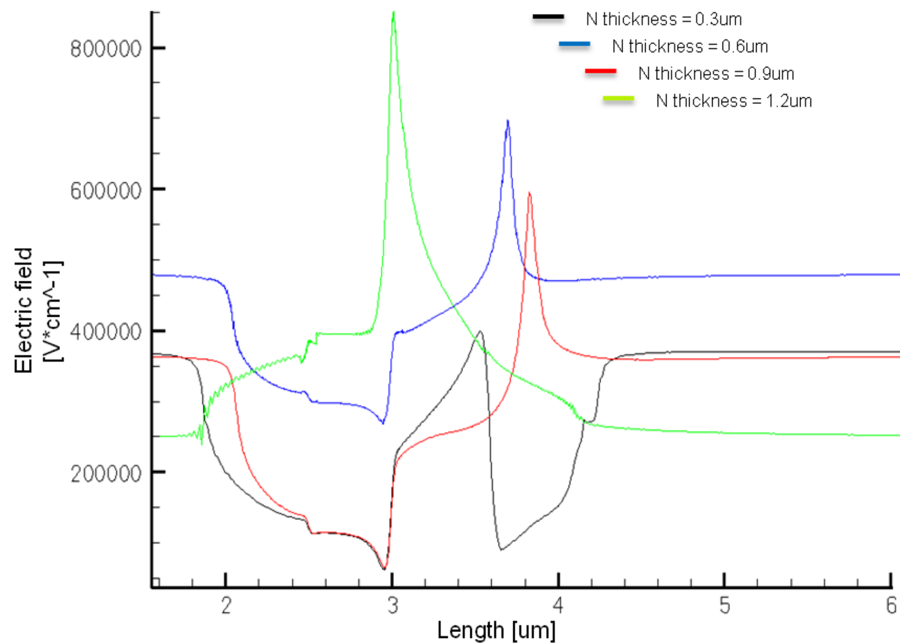

FIGURE 3.36: Effect of the Nitride thickness on the Electric Field distribution. Cut in the 2DEG region along the length of the device.

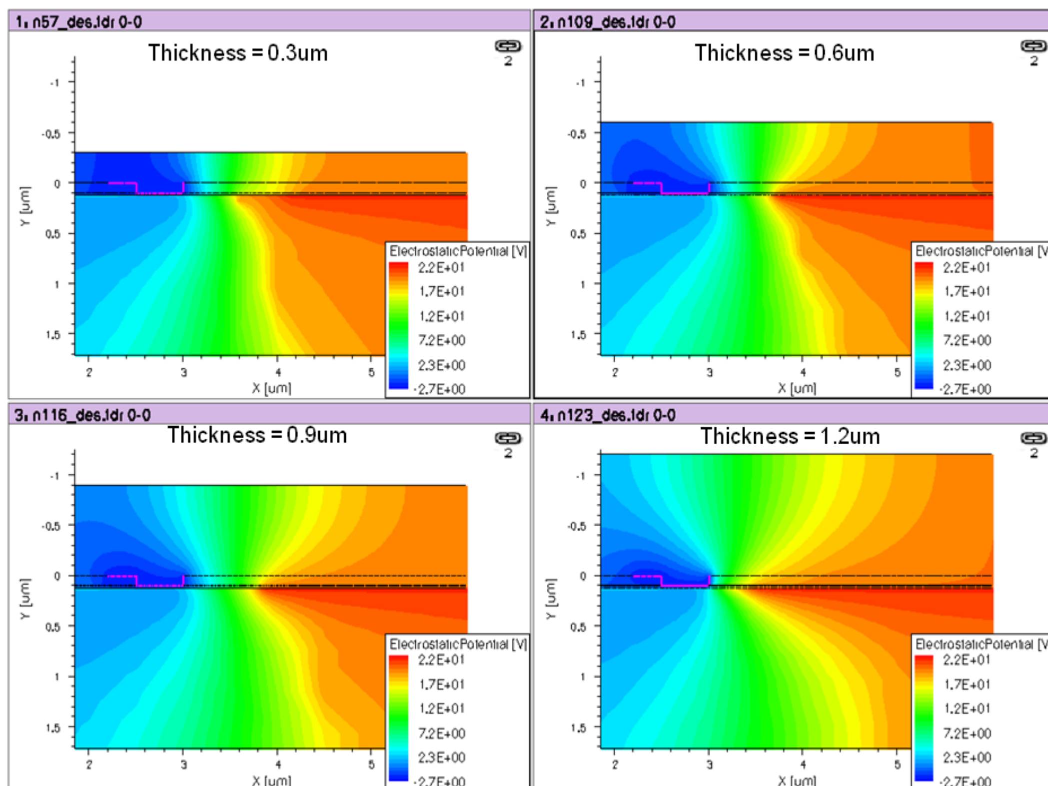

FIGURE 3.37: Effect of the Nitride thickness on the Electric Field distribution. Zoom in the gate area.

The further step was to gain some insights about the FP. At this purpose we attempted to vary the length (l) of the FP in such a way to see if its effect was the one which has been explained earlier in this section. We varied the FP extension towards the drain contact from $l = 0um$ to $l = 1um$ with steps of $0.2um$ and we run simulations with $Vg = -2.7V$ and $Vd = 20V$. For all of these simulations a $1.2um$ thick Nitride has been used. The fig 3.38 reports a general view of the various devices and it can see that the gate extension effective lowers the EF at the gate area and it creates another peak at the FP edge, cause the presence of the FP corner.

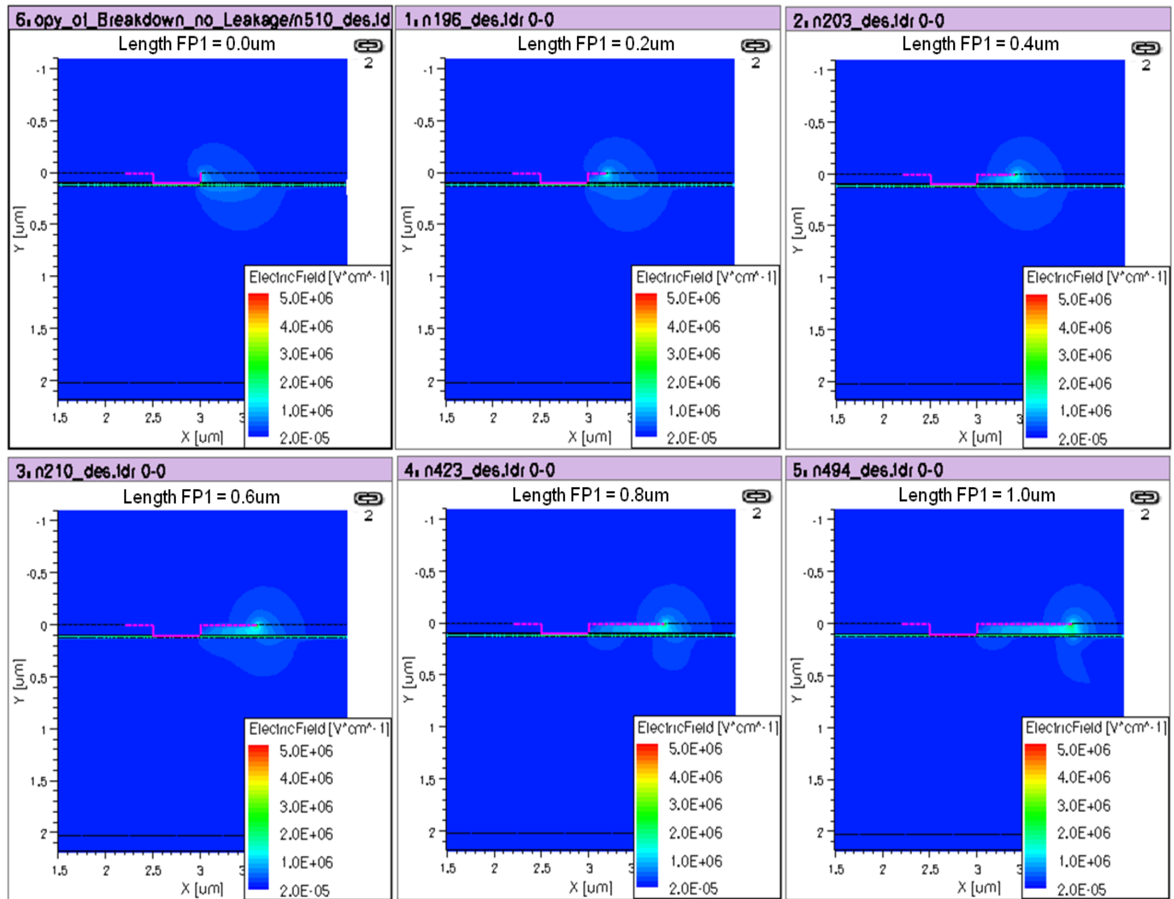

FIGURE 3.38: Effect of the FP length on the Electric Field distribution. Zoom in the gate area.

From fig 3.39, where a cut in the 2DEG is shown, it is more clear the FP effect. The FP leads to an effective lowering of the highest peak, which is the one at the gate edge, with the apparition of another peak just below the FP edge. Being the maximum EF lower than it the case without FP it has to point out the utility of this gate extension for a better reliability as long as the FP does not reach a certain length, above which the EF underneath the FP edge starts increasing. Indeed this is what our simulations revealed, i.e. further increasing the FP length above $1.0um$ the peak at the FP edge results by far higher than in the other cases. Moreover substantial reduction of the highest peak

can be seen moving the length of the FP from 0.0um to 0.4um, instead only a slight decrement can be noticed from a FP length of 0.4um to 0.6um and above this length no further improvement is present. This behaviour testifies that a clear FP effect has been predicted by the simulations.

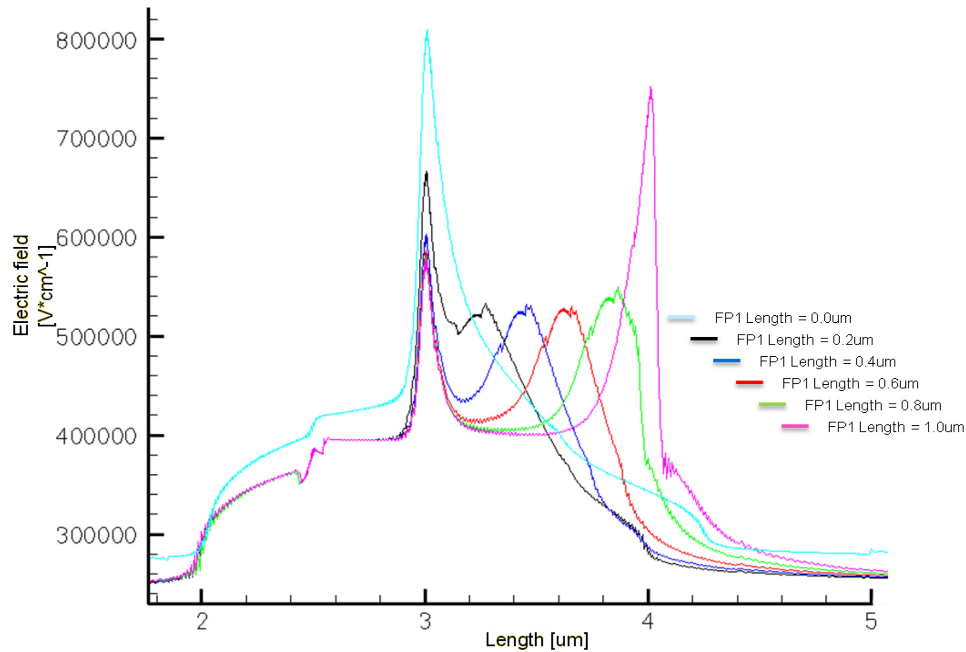

FIGURE 3.39: Effect of the FP length on the Electric Field distribution. Cut in the 2DEG along the length of the device.

The modification of the EF results in a changing of the depletion region in the sense that wider is the electric field spread and wider is the depletion zone, as it is shown in fig 3.40. Furthermore lower is the EF peak lower is the depletion below the gate edge.

Not only the 2DEG region has been analysed. Two other cuts have been evaluated, the former in the middle of the $AlGaN$ layer and the latter in the middle of the cap layer, shown respectively in fig 3.41 and in fig 3.42. The electric field in these cuts follows the trends of the one in the 2DEG region, with the maximum peak located underneath the gate edge, with its maximum value that decreases extending the FP towards the drain and with the presence of the second peak at the FP edge. As it can see the EF in the $AlGaN$ material is higher than that in the 2DEG but it has not to worry about it since this material has a wider band gap that the GaN and hence it can withstand higher voltage than GaN. What it has to consider instead is that in the cap layer the peak of the EF seems to be higher than that in the 2DEG. This is due to the proximity of the cap layer at the FP which induces higher EF. This fact could be a reason of the device failure when the drain is at high voltage, meaning that the weaker point of the device could be the cap layer.

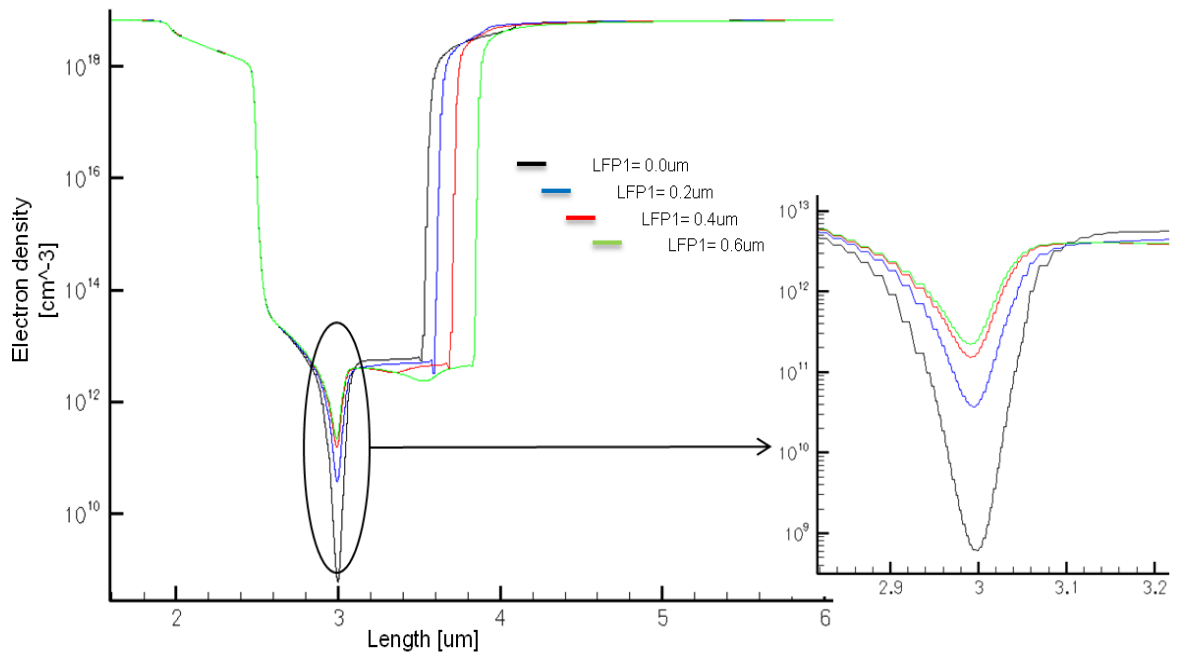

FIGURE 3.40: Effect of the FP length on the electron density in off-state. Cut in the 2DEG along the length of the device. In the inset it can see better the lowering of the maximum depletion.

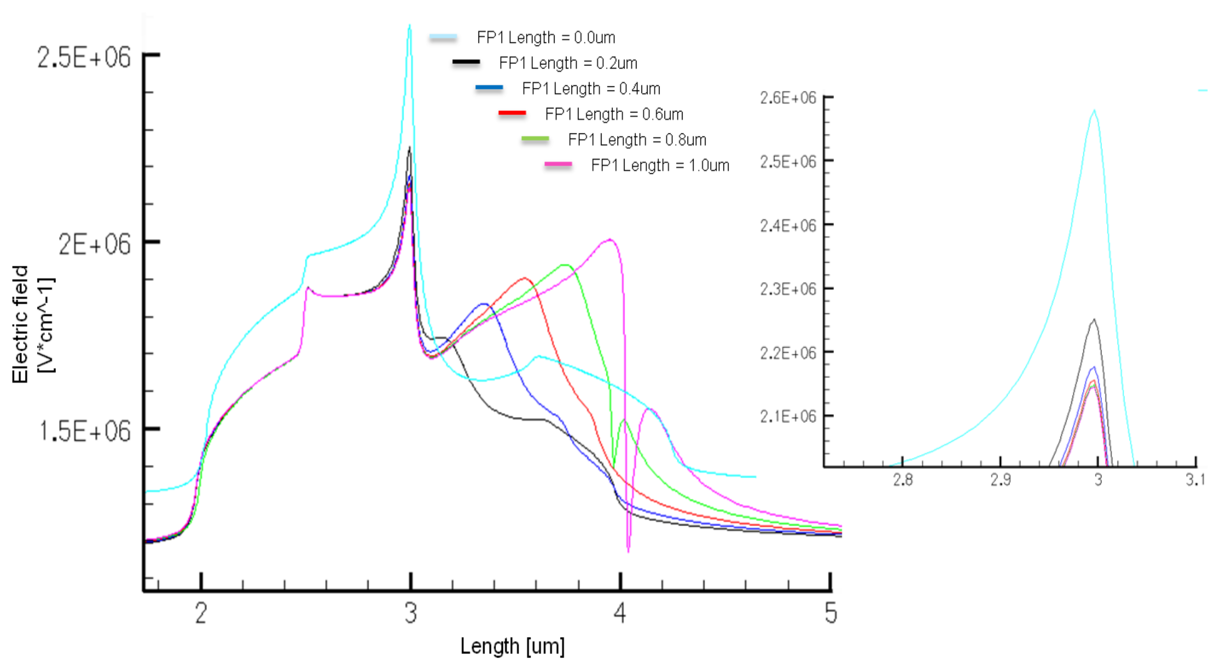

FIGURE 3.41: Effect of the FP1 length on the Electric Field distribution. Cut in the AlGaN layer along the length of the device. In the inset it can see better the lowering of the maximum EF.

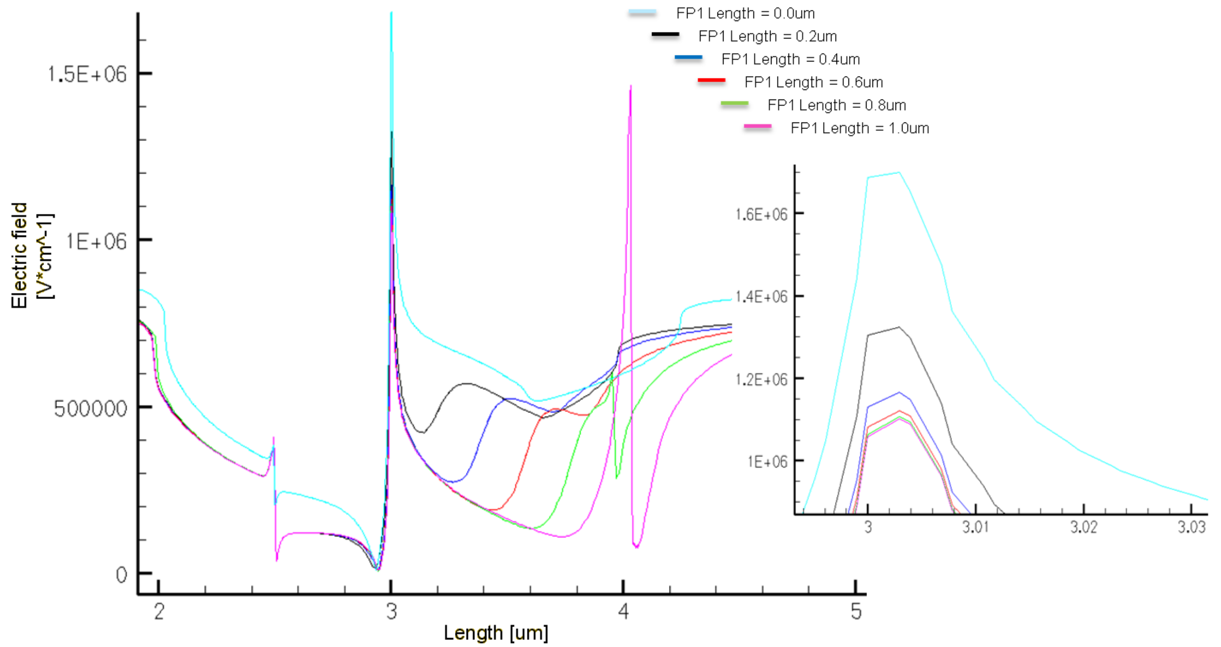

FIGURE 3.42: Effect of the FP1 length on the Electric Field distribution. Cut in the cap layer along the length of the device. In the inset it can see better the lowering of the maximum EF.

We repeated the simulations moving the drain voltage towards higher values, keeping the gate at the same voltage. Unfortunately there is an unexpected artefact which appears in the gate to drain region. We tried to modify both the mesh and the physical model included in order to simplify the deck and we attempted to change the dimensions of the device as well with the aim to see if it was a matter of good distribution of the electric field. In all this trial we did not get any improvement. Further efforts need to be put on this model in such a way to manage to obtain useful results about breakdown voltage.

Chapter 4

Summary and Conclusions

This thesis research was the result of my internship in NXP semiconductors R&D in Leuven (Belgium) thanks to a collaboration with the University of Padova (Italy). During this period various simulations have been carried out using Sentaurus software by Synopsys with the aim to check the usefulness of the simulation activity on the *GaN/AlGaN*-based HEMTs study.

The better electrical characteristics of *GaN* respect to the ones of *Si*, the most widely used material in electronics, make this material very suitable for high voltage, high temperature and high frequency applications and hence a lot of efforts on its study are being recently putting. Features like high electric breakdown field ($3MV/cm$), high electron saturation velocity ($1.5 \cdot 10^7 cm/s$) and the resistance at much higher operating temperatures ($300^o C - 500^o C$) than can the conventional semiconductor materials such like Si, $GaAs$, InP, are the result of the wide bandgap ($3.44eV$). Moreover a big advantage of *GaN* is to create heterostructures. For instance *GaN* and *AlN* create *AlGaN*, giving the possibility to grow epilayer *GaN/AlGaN* like the one that can be found in HEMTs. Cause the spontaneous polarization, which is due to the difference in the electronegativity of the various elements with which the compound material is made, and the piezoelectric polarization, resulted at the interface because of the strain caused by the different lattice parameters, a very high electron concentration is present at the interface. This high concentration, dependent on the *Al* percentage and on the *AlGaN* thickness, can reach values $> 10^{13} cm^{-2}$ and is characterized by an high electron mobility, with a maximum theoretical value of $2000 cm^2/Vs$. These last features make *GaN* suitable for high power applications as well, where high currents density are required.

Being a new technology the characteristics are still not well known so many researches are focused on it nowadays. At this purpose simulation activity could be used beside

the characterization in order to gain insight related to physical behaviours or in such a way to predict the electric behaviour without physically process the device since these materials are very expensive.

My activity began with the simulations of the DC characteristics of a real HEMT device which has been characterized in NXP. Basing on the $IdVg$ and $IdVd$ measurements I tried to create a simulation deck suitable to predict the same electrical characteristics as the real device. In the first model I introduced the iron doping in the buffer layer. The iron doping behaves as a p-type, helping to deplete the channel and to increase the resistance of the bulk buffer layer in order to avoid the punch-through phenomena. This mechanism involves electrons which, attracted from the high electric field of the drain region when high voltage is applied on this terminal, can come from the substrate leading to an avalanche multiplication. With a graded iron doping instead, high resistive bulk *GaN* can be achieved, keeping low the channel resistance and hence not contributing to rise the power consumption of the device. With the purpose to include this kind of doping, since this material was not present in the materials list file (datextcode.txt), I had to include the iron among them. Beside I had to specify the activation energy, the degeneracy factor and the cross section in the *GaN* parameter file (*GaN*.par). After that the *Fe* material could be used as a dopant. Unfortunately, speaking with a professor from Reggio Emilia, Giovanni Verzellesi, I knew that the simulator threats the doping in a simpler way respect to the traps, mostly in case in which the dopant creates deep levels. Since it has been found that *Fe* in *GaN* creates deep acceptor level, I defined the iron not as dopant but as trap. In this new definition way I could check that the result was effectively different that that obtained with Iron implemented as dopant. This model has been completed including traps in *AlGaN* layer. Varying the parameters of these traps I could firstly assess that the graded iron doping helps to deplete the 2DEG not contributing to lower the Id in on-state and secondly I managed to get a good fitting for the $IdVg$ both in the on-state and in the threshold regions. In the off state instead the visible difference is due to the fact that the gate leakage was not included in the simulation deck and hence it has not been possible to follow the Id leaking current. With this model I obtained good results also in the attempt to reproduce the output characteristics for various Vg.

The same procedure has been adopted in order to match the input and output characteristics of a second device, with a different structure. At this purpose I added to the deck the traps at the Nitride/cap interface and, starting from the values used in the first device, I varied slightly the concentration and the energy level of the traps in the *AlGaN* and buffer layers. The charts reported show that good matching has been obtained for both $IdVg$ and $IdVd$ curves. Basing on the same device I run AC simulation with the aim to verify whether the deck was suitable for gate capacitance simulations as well as

the DC ones. As it has been shown there is agreement with the measurements, at least concerning to the minimum and the maximum capacitance values. The positive shift in the Vth found in the measurements respect to the simulation could be related to the fact that trapping phenomena occurred before the capacitance test. Indeed characterization process can induce degradation effects, especially if stress measurements have been run. For this reason it should know the history of measurements in order to get further informations about the results.

From the measured $IdVg$ characteristics of both the devices it's clear that for gate voltage below a certain value the drain current does not decrease any more, meaning that leakage is ongoing. This effect is due to a flowing of electrons, which can move on the surface or can tunnel through the barrier, from the gate to the drain. Since it seems that the major cause is the latter one and since not many leakage simulations on HEMTs have been carried out so far, I attempted to include this behaviour in the model. In literature has been found that donor traps could be crated beneath the gate because of the etch process of the nitride layer in order to get the contact. Moreover the strong electric field at the gate edge can increase the strain in this region, creating cracks in the material and hence traps. In my simulations I added a $2nm$ thick donor layer just underneath the gate and I varied both the concentration and the energy level, founding that both modify the band diagram in such a way to allow the tunneling. Indeed, the increment of the traps concentration gives rise to a conduction band lowering of the cap layer. The same happens if it decreases the activation energy from the CB because it becomes more easy for the traps to be ionized. The droop in the CB results in a reduction of the barrier thickness, allowing the electron driven by the gate voltage to tunnel. This result has been achieved activating the non local tunneling which requires a non local mesh at the gate. This added mesh did not get any convergence problem so this model is very suitable for leakage simulations.

It is well known that GaN, contrary to silicon, has a different band structure. All the materials with direct band gap have the negative differential velocity characteristic which means that after reaching the maximum value for a certain electric field, the velocity decreases. Since it is possible to include new physical models by means of a $C++$ interface, basing on the paper from Farhaman et all I implemented a new mobility model. Unfortunately the results were worst than in the case we used the standard mobility. Furthermore the new mobility was by far more time consuming than the old one and created many convergence problems. Even if this trial has not been useful, we gained the insight that such a method could be used to implement some new physical model, since this material is object of various studies which might find out new informations.

Since the GaN-based HEMTs are very promising in high voltage applications, a very good device reliability must be reach. At this purpose the electric field distribution within the device needs to be evaluated in order to find a way to improve it, for instance by extending the gate contact towards the drain one, called field plate, or by prolonging the gate to drain distance. I analysed the effect of the field plate and the result is that it truly helps the lowering of the maximum electric field beneath the gate edge by creating another peak underneath the extension edge. This positive effect persists as long as its length is below a certain value above which the electric field peak created by the FP becomes higher than the one at the gate edge. It has also been shown that the weaker part of the device could be located in the cap layer because of its proximity at the gate contact. This is only a guess that needs to be controlled with two real devices, one with cap layer and one without it, by breakdown voltage test. The FP effect has been studied only for $Vd = 20V$ since artefacts appeared for higher voltages. This means that this model has to be further improved. Another improvement could be to include the gate leakage which is missing in the simulation deck I used for the EF study.

The results I obtained testify the utility of the simulations in the predictive results. Playing with the device structure could be possible to see the effect of the structure changing, for instance a lengthening of the gate, on the electric characteristics without process a new device. One possible investigation could be to find out a way to obtain a normally off device. Indeed, being the 2DEG concentration high even with $Vg = 0V$, it needs negative voltage in order to empty the channel and hence to switch-off the device, negatively impacting on the power consumption. In other words the HEMT is in on-state even if no gate voltage is applied.

With this work I proved the Sentaurus simulator can play an important role in the understanding of the GaN technology.

Appendix A

Code

In this appendix I reported some code used in our simulations. Firstly I wrote the parameter files used for *GaN* and *AlN*. The parameters for *AlGaN* have been automatically evaluated considering the Vegard's formula. After that I will present some command files which have been used for DC, AC, leakage and electric field avaluation. As last the it can find the mobility model implemented by means of the $C++$ interface. The basic formula and its derivative with respect to some parameters are showed. As firsty there is the model implemented for the high field mobility, then there is the mobility model for the low field.

A.1 Parameters files

A.1.1 GaN.par

```
Material = "GaN" {
**************************** Dielectric Constant: **************************
****************************************************************************
Epsilon
{ *  Ratio of the permittivity of material and vacuum
  * epsilon() = epsilon
epsilon = 9.5 # [1]
}

Epsilon_aniso
{ *  Ratio of the permittivity of material and vacuum
  * epsilon() = epsilon
epsilon = 10.4 # [1]
}
```

```
************************** Lattice Heat Capacity: *************************
***************************************************************************
LatticeHeatCapacity
{ *  lumped electron-hole-lattice heat capacity
  * cv() = cv + cv_b * T + cv_c * T^2 + cv_d * T^3
cv = 3.0 # [J/(K cm^3)]
cv_b = 0.0000e+00 # [J/(K^2 cm^3)]
cv_c = 0.0000e+00 # [J/(K^3 cm^3)]
cv_d = 0.0000e+00 # [J/(K^4 cm^3)]
}
*************************** Thermal Conductivity: *************************
***************************************************************************
Kappa
{ *  Lattice thermal conductivity

  Formula = 1
  * Formula = 1:
  * kappa() = kappa + kappa_b * T + kappa_c * T^2
kappa = 1.3 # [W/(K cm)]
kappa_b = 0.0000e+00 # [W/(K^2 cm)]
kappa_c = 0.0000e+00 # [W/(K^3 cm)]
}
*****************************  Hydro Parameters  *************************
***************************************************************************
EnergyRelaxationTime
{ *  Energy relaxation times in picoseconds
Formula(tau_w)_ele = 3
Spline(tau_w)_ele {
    0.0535 0.02921
    0.0600 0.02927
    0.0824 0.02941
    0.102 0.03051
    0.124 0.03179
    0.155 0.03533
    0.203 0.04224
    0.267 0.05133
    0.362 0.06543
    0.467 0.07951
    0.672 0.10620
    0.974 0.13855
    1.222 0.15871
    1.400 0.16764
    1.538 0.16912
    1.625 0.16697
```

```
    1.740 0.15494
    1.820 0.14296
    1.880 0.13077
    1.932 0.11952
    1.965 0.10944
    1.980 0.10027
    2.000 0.09286
    2.100 0.04000
    2.200 0.02000
    2.300 0.01200
    2.400 0.00800
    2.500 0.00600
}
(tau_w)_hol = 0.2 # [ps]
}

EnergyFlux
{ *  Coefficient in front of the energy flux equation
  *  energy_flux_coef=0.6 corresponds to Stratton model
energy_flux_coef_ele = 0.6 # [1]
energy_flux_coef_hol = 0.6 # [1]
}

ThermalDiffusion
{ *  Thermal diffusion factor (0 <= td <= 1)
  *  td=0. corresponds to Stratton model
td_n = 0.0000e+00 # [1]
td_p = 0.0000e+00 # [1]
}

HeatFlux
{ *  Heat flux factor (0 <= hf <= 1)
  * Heat flux plays some role in the vertical reach of hot carriers.
  * The values of hf below are NOT calibrated
hf_n = 1.0 # [1]
hf_p = 1.0 # [1]
}

AvalancheFactors
{ *  Coefficientss for avalanche generation with hydro
  *  Factors n_l_f, p_l_f for energy relaxation length in the expressions
  *  for effective electric field for avalanche generation
  *  eEeff = eEeff / n_l_f  ( or b = b*n_l_f )
  *  hEeff = hEeff / p_l_f  ( or b = b*p_l_f )
```

```
  *  Additional coefficients n_gamma, p_gamma, n_delta, p_delta
n_l_f = 0.8 # [1]
p_l_f = 0.8 # [1]
n_gamma = 0.0000e+00 # [1]
p_gamma = 0.0000e+00 # [1]
n_delta = 0.0000e+00 # [1]
p_delta = 0.0000e+00 # [1]
}
*************************** Bandgap  **********************************
***********************************************************************
Bandgap
{ * Eg = Eg0 + alpha Tpar2 / (beta + Tpar) - alpha T2 / (beta + T)
  * Parameter 'Tpar' specifies the value of lattice
  * temperature, at which parameters below are defined
  * Chi0 is electron affinity.
Chi0 = 3.4 # [eV]
Bgn2Chi = 0.5 # [1]
Eg0 = 3.47 # [eV]
alpha = 7.40e-04 # [eV K^-1]
beta = 6.00e+02 # [K]
Tpar = 0.0000e+00 # [K]
}

eDOSMass
{
  * For effective mass specificatition Formula1 (me approximation):
  * or Formula2 (Nc300) can be used :
Formula = 2 # [1]
  * Formula2:
  * me/m0 = (Nc300/2.540e19)2/3
  * Nc(T) = Nc300 * (T/300)3/2
Nc300 = 2.65e18 # [cm-3]
  * mass=0.222*mo
}

hDOSMass
{
  * For effective mass specificatition Formula1 (mh approximation):
  * or Formula2 (Nv300) can be used :
Formula = 2 # [1]
  * Formula2:
  * mh/m0 = (Nv300/2.540e19)2/3
  * Nv(T) = Nv300 * (T/300)3/2
Nv300 = 2.5e19 # [cm-3]
```

```
  *mass=1.0*mo
}
***************************************************************************
* Doping
***************************************************************************

*****************************  Mobility Models: **************************
* mu_lowfield^(-1) = mu_dop(mu_max)^(-1) + mu_Enorm^(-1) + mu_cc^(-1)
* Variable = electron value ,   hole value       # [units]
****************************************************************************
ConstantMobility:
{ * mu_const = mumax (T/T0)^(-Exponent)
mumax = 1700 ,2.0000e+01 # [cm2/(Vs)]
Exponent = 1 ,2.1 # [1]
}

DopingDependence:
{
  * For doping dependent mobility model three formulas
  * can be used. Formula1 is based on Masetti et al. approximation.
  * Formula2 uses approximation, suggested by Arora.
formula = 1 ,1 # [1]
  * If formula=1, model suggested by Masetti et al. is used:
  * mu_dop = mumin1 exp(-Pc/N) + (mu_const - mumin2)/(1+(N/Cr)^alpha)
  *                             - mu1/(1+(Cs/N)^beta)
  * with mu_const from ConstantMobility
mumin1 = 85,33 # [cm2/Vs]
mumin2 = 75,0.00E+00 # [cm2/Vs]
mu1 = 50,20 # [cm2/Vs]
Pc = 6.50E+15,5.00E+15 # [cm3]
Cr = 9.50E+16,8.00E+16 # [cm3]
Cs = 7.20E+19,8.00E+20 # [cm3]
alpha = 0.55,       0.55          # [1]
beta = 0.75,0.7 # [1]

  * If formula=2, model suggested by Arora is used:
  ***** Not Callibrated  *****
  ***** Parameters Below are for InN  *****
  * mu_dop = muminA + mudA/(1.+(N/N00)^AA),
  * where muminA=Ar_mumin*(T/T0)^Ar_alm; mudA = Ar_mud*(T/T0)^Ar_ald
  * N is net doping
  * N00=Ar_N0*(T/T0)^Ar_alN; AA = Ar_a*(T/T0)^Ar_ala
}
```

```
HighFieldDependence:
{ * Caughey-Thomas model:
  * mu_highfield = mu_lowfield / ( 1 + (mu_lowfield E / vsat)^beta )1/beta
  * beta = beta0 (T/T0)^betaexp.
beta0 = 0.9 ,0.8 # [1]
betaexp = 0.0000e+00 ,0.0000e+00 # [1]

  * Smoothing parameter for HydroHighField Caughey-Thomas model:
  * if Tl < Tc < (1+K_dT)*Tl, then smoothing between low field mobility
  * and HydroHighField mobility is used.
K_dT = 0.01 ,0.01 # [1]
  * Transferred-Electron Effect:
  * mu_highfield = (mu_lowfield+(vsat/E)*(E/E0_TrEf)4)/(1+(E/E0_TrEf)4)
E0_TrEf = 1.5000e+05 ,1.5000e+05 # [1]
Ksmooth_TrEf = 1 ,1 # [1]

 * For vsat either Formula1 or Formula2 can be used.
Vsat_Formula = 2 ,2 # [1]
 * Formula2 for saturation velocity:
 *            vsat = A_vsat - B_vsat*(T/T0)
 * (Parameter Vsat_Formula has to be equal to 2):
 * Obs: experiments seem to confirm a lower vsat for the 2D electron gas
than  bulk
A_vsat = 2.6e7 ,2.6e+07 # [1]
B_vsat = 0 , 0 # [1]
vsat_min = 5.000e+05 ,5.000e+05 # [1]
}

******************  Recombination/Generation Models: **********************
* Variable = electron value ,   hole value       # [unit]
****************************************************************************
Scharfetter * relation and trap level for SRH recombination:
{ * tau = taumin + ( taumax - taumin ) / ( 1 + ( N/Nref )^gamma
  * tau(T) = tau * ( (T/300)^Talpha )          (TempDep)
  * tau(T) = tau * exp( Tcoeff * ((T/300)-1) ) (ExpTempDep)
taumin = 0.0000e+00 ,0.0000e+00 # [s]
taumax = 1.0000e-9 ,1.0000e-9 # [s]
Nref = 1.0000e+16 ,1.0000e+16 # [cm^(-3)]
gamma = 1 ,1 # [1]
Talpha = -1.5000e+00 ,-1.5000e+00 # [1]
Tcoeff = 2.55 ,2.55 # [1]
Etrap = 0.0000e+00 # [eV]
}
```

```
vanOverstraetendeMan * Impact Ionization:
{ * G_impact = alpha_n n v_drift_n  +  alpha_p p v_drift_p
  * with alpha = gamma a  exp(-b gamma/E) for E<E0 (low) and E>E0 (high)
  *  with gamma = tanh(hbarOmega/(2kT0)) / tanh(hbarOmega/(2kT))
a(low) = 2.9e+08 ,1.3400e+08 # [1/cm]
a(high) = 2.9e+08 ,1.3400e+08 # [1/cm]
b(low) = 3.4e+07 ,2.0300e+07 # [V/cm]
b(high) = 3.4e+07 ,2.0300e+07 # [V/cm]
E0 = 4.0000e+05 ,4.0000e+05 # [V/cm]
hbarOmega = 0.035 ,0.035 # [eV]
}

QuantumPotentialParameters
{ * gamma:  weighting factor for quantum potential
  * theta:  weight for quadratic term
  * xi:     weight for quasi Fermi potential
  * eta:    weight for electrostatic potential
gamma = 1.41,5.6 # [1]
theta = 0.5 ,0.5 # [1]
xi = 1 ,1 # [1]
eta = 1 ,1 # [1]
}
*******************************************************************
*  Parameters for the recombination models below were taken
*  from GaAs and require calibration for accurate simulations
*******************************************************************
Auger * coefficients:
{ * R_Auger = ( C_n n + C_p p ) ( n p - ni_eff^2)
  * with C_n,p = (A + B (T/T0) + C (T/T0)^2) (1 + H exp(-{n,p}/N0))
A = 1.0000e-30 ,1.0000e-30 # [cm^6/s]
B = 0.0000e+00 ,0.0000e+00 # [cm^6/s]
C = 0.0000e+00 ,0.0000e+00 # [cm^6/s]
H = 0.0000e+00 ,0.0000e+00 # [1]
N0 = 1.0000e+18 ,1.0000e+18 # [cm^(-3)]
}

RadiativeRecombination * coefficients:
{ * R_Radiative = C (n p - ni_eff^2)
C = 2.0000e-10 # [cm^3/s]
}

BarrierTunneling {
mt = 0.5, 0.5
g = 1 , 2
```

```
}

HurkxTrapAssistedTunneling {
mt = 0.5, 0.5
}

}
```

A.1.2 AlN.par

```
Material = "AlN" {
**************************** Dielectric Constant: *************************
***************************************************************************
Epsilon
{ *  Ratio of the permittivities of material and vacuum
  * epsilon() = epsilon
epsilon = 8.5 # [1]
}

Epsilon_aniso
{ *  Ratio of the permittivities of material and vacuum
  * epsilon() = epsilon
epsilon = 10.7 # [1]
}
*************************** Lattice Heat Capacity: ************************
***************************************************************************
LatticeHeatCapacity
{ *  lumped electron-hole-lattice heat capacity
  * cv() = cv + cv_b * T + cv_c * T^2 + cv_d * T^3
cv = 1.94 # [J/(K cm^3)]
cv_b = 0.0000e+00 # [J/(K^2 cm^3)]
cv_c = 0.0000e+00 # [J/(K^3 cm^3)]
cv_d = 0.0000e+00 # [J/(K^4 cm^3)]
}
**************************** Thermal Conductivity: ************************
***************************************************************************
Kappa
{ *  Lattice thermal conductivity
  Formula = 1
  * Formula = 1:
  * kappa() = kappa + kappa_b * T + kappa_c * T^2
kappa = 2.85 # [W/(K cm)]
kappa_b = 0.0000e+00 # [W/(K^2 cm)]
```

```
kappa_c = 0.0000e+00 # [W/(K^3 cm)]
}
******************************  Hydro Parameters  **************************
****************************************************************************
EnergyRelaxationTime
{ *  Energy relaxation times in picoseconds
(tau_w)_ele = 0.05 # [ps]
(tau_w)_hol = 0.1 # [ps]
}

EnergyFlux
{ *  Coefficient in front of the energy flux equation
  *  energy_flux_coef=0.6 corresponds to Stratton model
energy_flux_coef_ele = 0.6 # [1]
energy_flux_coef_hol = 0.6 # [1]
}

ThermalDiffusion
{ *  Thermal diffusion factor (0 <= td <= 1)
  *  td=0. corresponds to Stratton model
td_n = 0.0000e+00 # [1]
td_p = 0.0000e+00 # [1]
}

HeatFlux
{ *  Heat flux factor (0 <= hf <= 1)
hf_n = 0.5 # [1]
hf_p = 0.5 # [1]
}

AvalancheFactors
{ *  Coefficientss for avalanche generation with hydro
  *  Factors n_l_f, p_l_f for energy relaxation length in the expressions
  *  for effective electric field for avalanche generation
  *  eEeff = eEeff / n_l_f  ( or b = b*n_l_f )
  *  hEeff = hEeff / p_l_f  ( or b = b*p_l_f )
  *  Additional coefficients n_gamma, p_gamma, n_delta, p_delta
n_l_f = 0.8 # [1]
p_l_f = 0.8 # [1]
n_gamma = 0.0000e+00 # [1]
p_gamma = 0.0000e+00 # [1]
n_delta = 0.0000e+00 # [1]
p_delta = 0.0000e+00 # [1]
}
```

```
**************************** Bandgap  **************************************
****************************************************************************
Bandgap
{ * Eg = Eg0 + alpha Tpar2 / (beta + Tpar) - alpha T2 / (beta + T)
  * Parameter 'Tpar' specifies the value of lattice
  * temperature, at which parameters below are defined
  * Chi0 is electron affinity.
Chi0 = 1.9 # [eV]
Eg0 = 6.2 # [eV]
alpha = 1.7900e-03 # [eV K^-1]
beta = 1.4620e+03 # [K]
Tpar = 3.0000e+02 # [K]
}

eDOSMass
{
  * For effective mass specificatition Formula1 (me approximation):
  * or Formula2 (Nc300) can be used :
Formula = 2 # [1]
  * Formula2:
  * me/m0 = (Nc300/2.540e19)2/3  = 0.3
  * Nc(T) = Nc300 * (T/300)3/2
a = 0.1905 # [1]
ml = 0.9163 # [1]
mm = 0.0000e+00 # [1]
Nc300 = 4.10e18 # [cm-3]
}

hDOSMass
{
  * For effective mass specificatition Formula1 (mh approximation):
  * or Formula2 (Nv300) can be used :
Formula = 2 # [1]
  * Formula2:
  * mh/m0 = (Nv300/2.540e19)2/3  ~= 5.0
  * Nv(T) = Nv300 * (T/300)3/2
a = 0.443587 # [1]
b = 3.6095e-03 # [K^-1]
c = 1.1735e-04 # [K^-2]
d = 1.2632e-06 # [K^-3]
e = 3.0256e-09 # [K^-4]
f = 4.6834e-03 # [K^-1]
g = 2.2869e-04 # [K^-2]
h = 7.4693e-07 # [K^-3]
```

```
i = 1.7275e-09 # [K^-4]
mm = 0.0000e+00 # [1]
Nv300 = 2.8400e+20 # [cm-3]
}

*****************************  Mobility Models: ****************************
* mu_lowfield^(-1) = mu_dop(mu_max)^(-1) + mu_Enorm^(-1) + mu_cc^(-1)      *
* Variable = electron value ,   hole value      # [units]                  *
****************************************************************************
ConstantMobility:
{ * mu_const = mumax (T/T0)^(-Exponent)
Exponent = 1,2.1 #[1]
mumax = 400,14 #[cm2/(Vs)]
}

DopingDependence:
{
  * For doping dependent mobility model three formulas
  * can be used. Formula1 is based on Masetti et al. approximation.
  * Formula2 uses approximation, suggested by Arora.
formula = 1 ,1 # [1]
  * If formula=1, model suggested by Masetti et al. is used:
  * mu_dop = mumin1 exp(-Pc/N) + (mu_const - mumin2)/(1+(N/Cr)^alpha)
  *                             - mu1/(1+(Cs/N)^beta)
  * with mu_const from ConstantMobility
mumin1 = 20,11 # [cm2/Vs]
mumin2 = 65,0.00E+00 # [cm2/Vs]
mu1 = 20,10 # [cm2/Vs]
Pc = 8.00E+17,5.00E+18 # [cm3]
Cr = 7.00E+16,8.00E+17 # [cm3]
Cs = 5.20E+17,8.00E+18 # [cm3]
alpha = 0.88,1.05         # [1]
beta = 0.75,0.75 # [1]

  * If formula=2, model suggested by Arora is used:
  ***** Not Callibrated  *****
  ***** Parameters Below are for InN  *****
  * mu_dop = muminA + mudA/(1.+(N/N00)^AA),
  * where muminA=Ar_mumin*(T/T0)^Ar_alm; mudA = Ar_mud*(T/T0)^Ar_ald
  * N is net doping
  * N00=Ar_N0*(T/T0)^Ar_alN; AA = Ar_a*(T/T0)^Ar_ala
}

HighFieldDependence:
```

```
{ * Caughey-Thomas model:
  * mu_highfield = mu_lowfield / ( 1 + (mu_lowfield E / vsat)^beta )1/beta
  * beta = beta0 (T/T0)^betaexp.
beta0 = 0.9,0.8 #[1]
betaexp = 0.0000e+00,0.0000e+00 #[1]

  * Smoothing parameter for HydroHighField Caughey-Thomas model:
  * if Tl < Tc < (1+K_dT)*Tl, then smoothing between low field mobility
  * and HydroHighField mobility is used.
K_dT = 0.01,0.01 # [1]
  * Transferred-Electron Effect:
  * mu_highfield = (mu_lowfield+(vsat/E)*(E/E0_TrEf)4)/(1+(E/E0_TrEf)4)
E0_TrEf = 2.7000e+05 ,2.7000e+05 # [1]
Ksmooth_TrEf = 1 ,1 # [1]

 * For vsat either Formula1 or Formula2 can be used.
Vsat_Formula = 2 ,2 # [1]
 * Formula2 for saturation velocity:
 *           vsat = A_vsat - B_vsat*(T/T0)
 * (Parameter Vsat_Formula has to be equal to 2):
A_vsat = 2.6e+07,2.6e+07 #[cm/s]
B_vsat = 0,0 #[cm/s]
vsat_min = 5.0000e+06,5.0000e+06 #[cm/s]
}
******************  Recombination/Generation Models: **********************
* Variable = electron value ,   hole value      # [units]                *
***************************************************************************
Scharfetter * relation and trap level for SRH recombination:
{ * tau = taumin + ( taumax - taumin ) / ( 1 + ( N/Nref )^gamma
  * tau(T) = tau * ( (T/300)^Talpha )          (TempDep)
  * tau(T) = tau * exp( Tcoeff * ((T/300)-1) ) (ExpTempDep)
taumin = 0.0000e+00 ,0.0000e+00 # [s]
taumax = 1.0000e-9 ,1.0000e-9 # [s]
Nref = 1.0000e+16 ,1.0000e+16 # [cm^(-3)]
gamma = 1 ,1 # [1]
Talpha = -1.5000e+00 ,-1.5000e+00 # [1]
Tcoeff = 2.55 ,2.55 # [1]
Etrap = 0.0000e+00 # [eV]
}

vanOverstraetendeMan * Impact Ionization:
{ * G_impact = alpha_n n v_drift_n  +  alpha_p p v_drift_p
  * with alpha = gamma a  exp(-b gamma/E) for E<E0 (low) and E>E0 (high)
  *  with gamma = tanh(hbarOmega/(2kT0)) / tanh(hbarOmega/(2kT))
```

```
a(low) = 2.9e8 ,1.3400e+07 # [1/cm]
a(high) = 2.9e8 ,1.3400e+07 # [1/cm]
b(low) = 3.4e8 ,2.0300e+08 # [V/cm]
b(high) = 3.4e8 ,2.0300e+08 # [V/cm]
E0 = 4.0000e+05,4.0000e+05 #[V/cm]
hbarOmega = 0.035,0.035 #[V/cm]
}
*******************************************************************
*  Parameters for the recombination models below were taken
*  from GaAs and require calibration for accurate simulations
*******************************************************************
Auger * coefficients:
{ * R_Auger = ( C_n n + C_p p ) ( n p - ni_eff^2)
  * with C_n,p = (A + B (T/T0) + C (T/T0)^2) (1 + H exp(-{n,p}/N0))
A = 1.0000e-30 ,1.0000e-30 # [cm^6/s]
B = 0.0000e+00 ,0.0000e+00 # [cm^6/s]
C = 0.0000e+00 ,0.0000e+00 # [cm^6/s]
H = 0.0000e+00 ,0.0000e+00 # [1]
N0 = 1.0000e+18 ,1.0000e+18 # [cm^(-3)]
}

RadiativeRecombination * coefficients:
{ * R_Radiative = C (n p - ni_eff^2)
C = 2.0000e-10 # [cm^3/s]
}

BarrierTunneling {
mt = 0.5, 0.5
g = 1 , 2
}

}
```

A.2 command files

A.2.1 Header

The header is the common code for every command files since it contains only the calculations or the polarizations.

```
# Computation of interface charges
```

```
!(
set q 1.602e-19
set x @x@
set x1 @x1@
set strainRelax @strainRelax@

# Enforce correct range for strainRelax
if ($strainRelax>1) {set strainRelax 1}
if ($strainRelax<0) {set strainRelax 0}

# Mole fraction dependent spontaneous polarization
set Psp_AlN [expr -8.1e-6/$q]
set Psp_GaN [expr -2.9e-6/$q]
set Psp_AlGaN [expr $x*$Psp_AlN + (1-$x)*$Psp_GaN]
set DPsp [expr $Psp_GaN - $Psp_AlGaN]

# Mole fraction dependent piezoelectric polarization
set e33i [expr ($x*1.46e-4 + (1 - $x)*0.73e-4)/$q]
set e31i [expr ($x*(-0.60e-4) + (1 - $x)*(-0.49e-4))/$q]
set c13i [expr $x*108 + (1 - $x)*103]
set c33i [expr $x*373 + (1 - $x)*405]
set straini [expr (1-$strainRelax)*($x*(3.189 - 3.112)/($x*3.112 + (1-$x)*3.189))]
set Ppz_AlGaN [expr 2*$straini*($e31i - $c13i/$c33i*$e33i)]
set DPpz [expr -$Ppz_AlGaN]
set intCharge [expr $DPsp + $DPpz]
set ToT_AlGaN [expr $Psp_AlGaN + $Ppz_AlGaN]
set Tot_GaN [expr $Psp_GaN + 0]
set Tot_1st [expr $x1* ($Tot_GaN -$ToT_AlGaN)]
set Tot_2nd [expr $x1* ($ToT_AlGaN - $Tot_GaN)]
set Tot_3rd [expr $x1* ($Tot_GaN + 0)]

# Reporting
puts "* Spontaneous polarization for AlGaN: [format %1.2e [expr $q*$Psp_AlGaN]]
(C/cm^2)"
puts "* Piezopolarization for AlGaN: [format %1.2e [expr $q*$Ppz_AlGaN]] (C/cm^2)"
puts "*   Total AlGaN Polarization: [format %1.2e [expr $q*($Psp_AlGaN +
$Ppz_AlGaN)]] (C/cm^2)"
puts "\n*   Total GaN Polarization: [format %1.2e [expr $q*$Psp_GaN]] (C/cm^2)"
puts "\n* Int. charge due to spontaneous polarization variation: [format %1.2e
[expr $q*$DPsp]] (C/cm^2)"
puts "* Int. charge due to piezopolarization variation: [format %1.2e
[expr $q*$DPpz]] (C/cm^2)"
puts "*   Total interface charge: [format %1.2e [expr $q*$intCharge]] (C/cm^2)"
)!
```

A.2.2 DC simulations

This following is the code which has been used for the DC simulations, i.e. $IdVg$, $IdVd$, Leakage and breakdown. For the latter one no leakage has been considered.

```
Electrode {
{ Name="Gate"   Voltage= 0 Schottky Workfunction=@WF@}
{ Name="Source" Voltage= 0 resist=200}
{ Name="Drain"  Voltage= 0 resist=200}
}

File {
Grid= "@tdr@"
Parameter= "@parameter@"

Current= "@plot@"
Plot= "@tdrdat@"
Output = "@log@"
}

Physics {
AreaFactor=@area@
Mobility(
DopingDependence
eHighfieldsaturation
  )
  Recombination(
  SRH
  Auger
  Radiative
eAvalanche(Eparallel)
  )
EffectiveIntrinsicDensity (Nobandgapnarrowing)
Fermi
Aniso(Poisson)
eBarrierTunneling "NLM"
}

Physics (RegionInterface="schottky/buffer") {
Charge(Conc=!(puts $Tot_1st)!)
}

Physics (RegionInterface="schottky/cap") {
```

```
eThermionic
Charge(Conc=!(puts $Tot_2nd)!)
}

Physics (RegionInterface="cap/insulator1") {
Charge(Conc=!(puts $Tot_3rd)!)
Traps (
Donor Level Conc=2.55e13 EnergyMid=1.5 FromCondBand
eXSection=1e-15 hXSection= 1e-15
)
}

Physics (RegionInterface="cap/insulator2") {
Charge(Conc=!(puts $Tot_3rd)!)
Traps (
Donor Level Conc=2.55e13 EnergyMid=1.5 FromCondBand
eXSection=1e-15 hXSection= 1e-15
)
}

Physics (Region="traps_cap") {
Traps(
Donor Level Conc=@don@ EnergyMid=@Lev@ FromCondBand
eXSection=1e-15 hXSection=1e-15
)
}

Physics (Region="buffer") {
Traps (
Acceptor Level Conc=9e16 EnergyMid=0.7 EnergySig= 0 FromCondBand
eXSection= 1e-15 hXSection= 1e-15
)
}

Physics (Region="schottky") {
Traps (
Acceptor Level Conc=3e17 EnergyMid= 0.7 EnergySig= 0 FromCondBand
eXSection= 1e-15 hXSection= 1e-15
)
}

Physics (Electrode="Gate") {
eThermionic
}
```

```
Plot {
Potential Electricfield/Vector eDensity hDensity
eCurrent/Vector hCurrent/Vector TotalCurrent/Vector
SRH Auger Avalanche eMobility hMobility
eQuasiFermi hQuasiFermi eGradQuasiFermi hGradQuasiFermi
eEparallel hEparallel eMobility hMobility
eVelocity hVelocity DonorConcentration Acceptorconcentration
Doping SpaceCharge ConductionBand ValenceBand
BandGap Affinity xMoleFraction eTemperature hTemperature
eTrappedCharge hTrappedCharge eInterfaceTrappedCharge
}

Math {
Nonlocal "NLM" ( Electrode="Gate"
Length=5e-7
Digits=4
EnergyResolution=0.001
)
Extrapolate
Digits= 7
ErrRef(electron) = 1E5
ErrRef(hole) = 1E3
RHSmin= 1e-10
RHSmax= 1e30
CDensityMin= 1e-20
DirectCurrentComputation
RelTermMinDensity= 1e5
eMobilityAveraging= ElementEdge
CNormPrint
}

Solve {

* a) zero solution
Coupled (Iterations= 1500 LinesearchDamping= 0.001)  {Poisson}
Coupled (Iterations= 100) {Poisson Electron}

*---------------------------------------------------------------
* IdVg simulation
#if @<[string compare Simul "IdVg"] == 0>@
*---------------------------------------------------------------
* - Vd bias
Quasistationary (
```

```
InitialStep= 5e-2 Minstep= 1e-4 MaxStep= 0.1 Increment= 1.3 Decrement=1.35
Goal {Name="Drain" Voltage=@Vd@}
) {
Coupled(Iterations= 18) {Poisson Electron}
}

* - Vg ramp
NewCurrentFile="IdVg_"
Quasistationary (
InitialStep= 8e-3 Minstep= 4e-4 MaxStep= 0.1 Increment= 1.2 Decrement=1.25
Goal {Name="Gate" Voltage=@Vg@}
) {
Coupled(Iterations= 20) {Poisson Electron}
}

*----------------------------------------------------------------
* IdVd simulation
#elif @<[string compare Simul "IdVd"] == 0>@
*----------------------------------------------------------------
* - Vg bias
Quasistationary (
InitialStep= 2e-2 Minstep= 1e-4 MaxStep= 0.1 Increment= 1.3 Decrement=1.35
Goal {Name="Gate" Voltage=@Vg@}
) {
Coupled(Iterations= 18) {Poisson Electron}
}

* - Vd ramp
NewCurrentFile="IdVd_"
Quasistationary (
InitialStep= 1e-2 Minstep= 4e-4 MaxStep= 0.1 Increment= 1.2 Decrement=1.25
Goal {Name="Drain" Voltage=@Vd@}
) {
Coupled(Iterations= 20) {Poisson Electron}
}

*------------------------------------------------------------------
#endif
*------------------------------------------------------------------
}
```

A.2.3 AC simulations

Code wrote for the AC simulations.

```
Device NMOS {

Electrode {
{ Name="Gate"   Voltage= 0 Schottky Workfunction=5.1}
{ Name="Source" Voltage= 0 resist=200}
{ Name="Drain"  Voltage= 0 resist=200}
}

File {
* Input files
Grid= "@tdr@"
Parameter= "@parameter@"

* Output files
Current= "@plot@"
Plot= "@tdrdat@"
}

Physics {
AreaFactor=2400
Hydrodynamic(eTemperature)
Mobility(
DopingDependence
eHighfieldsaturation
  )
EffectiveIntrinsicDensity (Nobandgapnarrowing)
Fermi
Recombination(SRH)
RecGenHeat
Aniso(Poisson)
}

Physics (RegionInterface="schottky/buffer") {
Charge(Conc=!(puts $Tot_1st)!)
}

Physics (RegionInterface="schottky/cap") {
Charge(Conc=!(puts $Tot_2nd)!)
}
```

```
Physics (RegionInterface="cap/insulator1") {
Charge(Conc=!(puts $Tot_3rd)!)
Traps (
Donor Level Conc=2.55e13 EnergyMid=1.5 FromCondBand
eXSection=1e-15 hXSection= 1e-15
)
}

Physics (RegionInterface="cap/insulator2") {
Charge(Conc=!(puts $Tot_3rd)!)
Traps (
Donor Level Conc=2.55e13 EnergyMid=1.5 FromCondBand
eXSection=1e-15 hXSection= 1e-15
)
}

Physics (Region="buffer") {
Traps (
(Acceptor Level Conc= 8e16 EnergyMid=0.7 EnergySig= 0 FromCondBand
 eXSection= 1e-15 hXSection= 1e-15)
)
}

Physics (Region="schottky") {
Traps (
(Acceptor Level Conc= 2e17 EnergyMid= 0.7 EnergySig= 0 FromCondBand
 eXSection= 1e-15 hXSection= 1e-15)
)
}

Plot {
Potential Electricfield/Vector eDensity hDensity
eCurrent/Vector hCurrent/Vector TotalCurrent/Vector
SRH Auger Avalanche eMobility hMobility
eQuasiFermi hQuasiFermi eGradQuasiFermi hGradQuasiFermi
eEparallel hEparallel eMobility hMobility
eVelocity hVelocity DonorConcentration Acceptorconcentration
Doping SpaceCharge ConductionBand ValenceBand
BandGap Affinity xMoleFraction eTemperature hTemperature
eTrappedCharge hTrappedCharge eInterfaceTrappedCharge
}
}
```

```
Math {
Extrapolate
Iterations= 16
Digits= 6
ErrRef(electron) = 1E5
ErrRef(hole) = 1E3
RHSmin= 1e-10
RHSmax= 1e30
CDensityMin= 1e-20
DirectCurrentComputation
RelTermMinDensity= 1e5
eMobilityAveraging= ElementEdge
CNormPrint
}

File {
Output = "@log@"
    ACExtract = "@acplot@"
}

System {
NMOS trans (Drain=d Source=s Gate=g )
Vsource_pset vd (d 0) {dc=0}
Vsource_pset vs (s 0) {dc=0}
Vsource_pset vg (g 0) {dc=0}
 }

Solve {

* a) zero solution
Coupled (Iterations= 100000 LinesearchDamping= 0.001)  {Poisson}
Coupled (Iterations= 100) {Poisson Electron Hole}
Coupled (Iterations= 100) {Poisson Electron Hole eTemperature}

* b) Vd bias
Quasistationary (
InitialStep= 1e-2 Minstep= 5e-4 MaxStep= 0.2 Increment= 1.2
Goal {Parameter=vd.dc Voltage=@Vd@}
) {
Coupled {Poisson Electron Hole eTemperature}
}

* c) Ac analisys - gate sweep
NewCurrentFile="Ac_"
```

```
Quasistationary (
InitialStep= 5e-3 Minstep= 5e-4 MaxStep= 0.2 Increment= 1.2 Decrement=1.25
Goal {Parameter=vg.dc Voltage=@Vg@}
)
{ACCoupled  (
StartFrequency=@freq@ EndFrequency=@freq@
NumberOfPoints=1 Decade
Node (d s g) Exclude (vd vs vg) )
{Poisson Electron Hole eTemperature}
}

}
```

A.3 New mobility model files

A.3.1 High Field Mobility

```
#include <iostream.h>
#include <math.h>
#include "PMIModels.h"

// implementation of the high field dependent mobility model for HEMT device
using the PMI interface

class HEMT_HighFieldMobility : public PMI_HighFieldMobility {

protected:
  double a, n1, n2, Ecc, vsat;

private:
  short ind_field;
  double Ec, Fabs;

  void Compute_internal (const double F);

public:
  HEMT_HighFieldMobility ( const PMI_Environment& env,
   const PMI_HighFieldDrivingForce force,
                         const PMI_AnisotropyType anisotype );

  ~HEMT_HighFieldMobility ();
```

```
void Compute_mu
  (const double pot,        // electrostatic potential
   const double n,          // electron density
   const double p,          // hole density
   const double t,          // lattice temperature
   const double ct,         // carrier temperature
   const double mulow,      // low field mobility
   const double F,          // driving force
   double& mu);             // mobility

void Compute_dmudpot
  (const double pot,        // electrostatic potential
   const double n,          // electron density
   const double p,          // hole density
   const double t,          // lattice temperature
   const double ct,         // carrier temperature
   const double mulow,      // low field mobility
   const double F,          // driving force
   double& dmudpot);        // derivative of mobility
                            // with respect to electrostatic potential

void Compute_dmudn
  (const double pot,        // electrostatic potential
   const double n,          // electron density
   const double p,          // hole density
   const double t,          // lattice temperature
   const double ct,         // carrier temperature
   const double mulow,      // low field mobility
   const double F,          // driving force
   double& dmudn);          // derivative of mobility
                            // with respect to electron density

void Compute_dmudp
  (const double pot,        // electrostatic potential
   const double n,          // electron density
   const double p,          // hole density
   const double t,          // lattice temperature
   const double ct,         // carrier temperature
   const double mulow,      // low field mobility
   const double F,          // driving force
   double& dmudp);          // derivative of mobility
                            // with respect to hole density
```

```
  void Compute_dmudt
    (const double pot,        // electrostatic potential
     const double n,          // electron density
     const double p,          // hole density
     const double t,          // lattice temperature
     const double ct,         // carrier temperature
     const double mulow,      // low field mobility
     const double F,          // driving force
     double& dmudt);          // derivative of mobility
                              // with respect to lattice temperature

  void Compute_dmudct
    (const double pot,        // electrostatic potential
     const double n,          // electron density
     const double p,          // hole density
     const double t,          // lattice temperature
     const double ct,         // carrier temperature
     const double mulow,      // low field mobility
     const double F,          // driving force
     double& dmudct);         // derivative of mobility
                              // with respect to carrier temperature

  void Compute_dmudmulow
    (const double pot,        // electrostatic potential
     const double n,          // electron density
     const double p,          // hole density
     const double t,          // lattice temperature
     const double ct,         // carrier temperature
     const double mulow,      // low field mobility
     const double F,          // driving force
     double& dmudmulow);      // derivative of mobility
                              // with respect to low field mobility

  void Compute_dmudF
    (const double pot,        // electrostatic potential
     const double n,          // electron density
     const double p,          // hole density
     const double t,          // lattice temperature
     const double ct,         // carrier temperature
     const double mulow,      // low field mobility
     const double F,          // driving force
     double& dmudF);          // derivative of mobility
                              // with respect to driving force
};
```

```
void HEMT_HighFieldMobility::
Compute_internal ( const double F )
{
Fabs = fabs (F);
}

HEMT_HighFieldMobility::
HEMT_HighFieldMobility (const PMI_Environment& env,
   const PMI_HighFieldDrivingForce force,
                        const PMI_AnisotropyType anisotype ) :
PMI_HighFieldMobility (env, force, anisotype)
{
  ind_field = FieldName2Index("ElectricField");
}

HEMT_HighFieldMobility::
~HEMT_HighFieldMobility ()
{
}

void HEMT_HighFieldMobility::
Compute_mu (const double pot, const double n,
            const double p, const double t, const double ct,
            const double mulow, const double F, double& mu)
{
const double kb = 8.62e-5;
  const double q  = 1.6021892e-19;
double num, denom, num_mu, denom_mu;
double Ec, in;

Compute_internal (F);

num = mulow+vsat*(pow(Fabs,(n1-1))/pow(Ecc,n1));
  denom = 1+a*pow((Fabs/Ecc),n2)+pow((Fabs/Ecc),n1);
mu = num/denom;
}

void HEMT_HighFieldMobility::
Compute_dmudpot (const double pot, const double n,
             const double p, const double t, const double ct,
             const double mulow, const double F, double& dmudpot)
{  dmudpot=0.0;
}
```

```
void HEMT_HighFieldMobility::
Compute_dmudn ( const double pot, const double n,
            const double p, const double t, const double ct,
            const double mulow, const double F, double& dmudn)
{  dmudn=0.0;
}

void HEMT_HighFieldMobility::
Compute_dmudp ( const double pot, const double n,
             const double p, const double t, const double ct,
             const double mulow, const double F, double& dmudp)
{  dmudp=0.0;
}

void HEMT_HighFieldMobility::
Compute_dmudt ( const double pot, const double n,
             const double p, const double t, const double ct,
             const double mulow, const double F, double& dmudt)
{  dmudt=0.0;
}

void HEMT_HighFieldMobility::
Compute_dmudct (const double pot, const double n,
             const double p, const double t, const double ct,
             const double mulow, const double F, double& dmudct)
{  dmudct=0.0;
}

void HEMT_HighFieldMobility::
Compute_dmudmulow ( const double pot, const double n,
             const double p, const double t, const double ct,
             const double mulow, const double F, double& dmudmulow)
{
double num, denom, num_mu, denom_mu;
double Ec, in;

Compute_internal (F);

  denom = 1+a*pow((Fabs/Ecc),n2)+pow((Fabs/Ecc),n1);
dmudmulow=1/denom;
}

void HEMT_HighFieldMobility::
```

```
Compute_dmudF ( const double pot, const double n,
             const double p, const double t, const double ct,
             const double mulow, const double F, double& dmudF)
{
const double kb = 8.62e-5;
  const double q  = 1.6021892e-19;
  double num1, num2, num3, num4;
  double denom, num_mu, denom_mu;
  double Ec, in;
const double signF = (F >= 0.0) ? 1.0 : -1.0;

Compute_internal (F);

num1= (vsat/pow(Ecc,n1))*(n1-1)*pow(Fabs,(n1-2));
num2= 1+a*pow((Fabs/Ecc),n2)+pow((Fabs/Ecc),n1);
num3= mulow+vsat*pow(Fabs,(n1-1))/pow(Ecc,n1);
num4= a*(n2/pow(Ecc,n2))*pow(Fabs,(n2-1))+(n1/pow(Ecc,n1))*pow(Fabs,(n1-1));
denom= pow(num2,2);
dmudF= ((num1*num2-num3*num4)/denom)*signF;
}

class HEMT_e_HighFieldMob : public HEMT_HighFieldMobility {

public:
  HEMT_e_HighFieldMob ( const PMI_Environment& env,
   const PMI_HighFieldDrivingForce force,
        const PMI_AnisotropyType anisotype );

  ~HEMT_e_HighFieldMob () {}
};

HEMT_e_HighFieldMob::
HEMT_e_HighFieldMob ( const PMI_Environment& env,
   const PMI_HighFieldDrivingForce force,
        const PMI_AnisotropyType anisotype ):

HEMT_HighFieldMobility (env, force, anisotype)
{
a=InitParameter ("a_e" , 6.1973);
  vsat=InitParameter ("vsat_e" , 1.9e7);
  n1=InitParameter ("n1_e" , 7.2044);
  n2=InitParameter ("n2_e" , 0.7857);
  Ecc = InitParameter ("Ecc_e", 220.8936e3);
}
```

```
class HEMT_h_HighFieldMob : public HEMT_HighFieldMobility {

public:
  HEMT_h_HighFieldMob ( const PMI_Environment& env,
   const PMI_HighFieldDrivingForce force,
        const PMI_AnisotropyType anisotype );

  ~HEMT_h_HighFieldMob () {}
};

HEMT_h_HighFieldMob::
HEMT_h_HighFieldMob ( const PMI_Environment& env,
   const PMI_HighFieldDrivingForce force,
        const PMI_AnisotropyType anisotype ) :

HEMT_HighFieldMobility (env, force, anisotype)
{
a=InitParameter ("a_h" , 6.1973);
  vsat=InitParameter ("vsat_h" , 1.9e7);
  n1=InitParameter ("n1_h" , 7.2044);
  n2=InitParameter ("n2_h" , 0.7857);
  Ecc = InitParameter ("Ecc_h", 220.8936e3);
}

extern "C"
PMI_HighFieldMobility* new_PMI_HighField_e_Mobility
  ( const PMI_Environment& env,
const PMI_HighFieldDrivingForce force,
const PMI_AnisotropyType anisotype )
{
return new HEMT_e_HighFieldMob (env, force, anisotype);
}

extern "C"
PMI_HighFieldMobility* new_PMI_HighField_h_Mobility
  ( const PMI_Environment& env,
const PMI_HighFieldDrivingForce force,
        const PMI_AnisotropyType anisotype )
{
return new HEMT_h_HighFieldMob (env, force, anisotype);
}
```

A.3.2 Low Field Mobility

```
#include <iostream.h>
#include <math.h>
#include "PMIModels.h"

// implementation of the conc. dependent mobility model for HEMT device using
 the PMI interface

class HEMT_LowFieldMob : public PMI_DopingDepMobility {

protected:
  double mumin, mumax, alfa, b1, b2, b3, b4, Nref, NN, Tamb;

public:
  HEMT_LowFieldMob (const PMI_Environment& env,
                    const PMI_AnisotropyType anisotype);

  ~HEMT_LowFieldMob () {}

  void Compute_m
    (const double n,        // electron density
     const double p,        // hole density
     const double t,        // lattice temperature
     double& m);            // doping dependent mobility

  void Compute_dmdn
    (const double n,        // electron density
     const double p,        // hole density
     const double t,        // lattice temperature
     double& dmdn);         // derivative of doping dependent mobility
                            // with respect to electron density

  void Compute_dmdp
    (const double n,        // electron density
     const double p,        // hole density
     const double t,        // lattice temperature
     double& dmdp);         // derivative of doping dependent mobility
                            // with respect to hole density

  void Compute_dmdt
    (const double n,        // electron density
     const double p,        // hole density
```

```
     const double t,        // lattice temperature
     double& dmdt);         // derivative of doping dependent mobility
                            // with respect to lattice temperature
};

HEMT_LowFieldob::
HEMT_LowFieldMob (const PMI_Environment& env,
                  const PMI_AnisotropyType anisotype) :

PMI_DopingDepMobility (env, anisotype) {}

void HEMT_LowFieldMob::
Compute_m (const double n, const double p,
           const double t, double& m)
{
const double kb = 8.62e-5;
  const double q  = 1.6021892e-19;
  double k0, k1, k2, k3, num, den;

  k0=mumin*pow((t/Tamb),b1);
  num=(mumax-mumin)*pow((t/Tamb),b2);
  k1=Nref*pow((t/Tamb),b3);
  k2=NN/k1;
  k3=alfa*pow((t/Tamb),b4);
  den=1+pow(k2,k3);
  m=k0+num/den;
}

void HEMT_LowFieldMob::
Compute_dmdn (const double n, const double p,
              const double t, double& dmdn)
{ dmdn=0;
}

void HEMT_LowFieldMob::
Compute_dmdp (const double n, const double p,
              const double t, double& dmdp)
{
const double kb = 8.62e-5;
  const double q  = 1.6021892e-19;
  dmdp=0;
}

void HEMT_LowFieldMob::
```

```
Compute_dmdt (const double n, const double p,
              const double t, double& dmdt)
{
double k0, k1, k2, k3, num, den;
  double ka1, ka2, ka3, ka4, ka5, ka6;

  k0=mumin*pow((t/Tamb),b1);
  num=(mumax-mumin)*pow((t/Tamb),b2);
  k1=Nref*pow((t/Tamb),b3);
  k2=NN/k1;
  k3=alfa*pow((t/Tamb),b4);
  den=1+pow(k2,k3);
  ka1=b1*(mumin/pow(Tamb,b1))*pow(t,b1-1);
  ka2=(b2/pow(Tamb,b2))*(mumax-mumin)*pow(t,b2-1);
  ka3=(ka2*den)/pow(den,2);
  ka4=((mumax-mumin)*pow((t/Tamb),b2))/pow(den,2);
  ka5=alfa*(b4/pow(Tamb,b4))*pow(t,b4-1)*log(k2)-
+ alfa*pow((t/Tamb),b4)*(b3/(t*NN));
  ka6=pow(k2,k3)*ka5;
  dmdt=ka1+ka3-ka4*ka6;
}

class HEMT_e_LowFieldMob : public HEMT_LowFieldMob {

public:
  HEMT_e_LowFieldMob (const PMI_Environment& env,
                      const PMI_AnisotropyType anisotype);
  ~HEMT_e_LowFieldMob () {}
};

HEMT_e_LowFieldMob::
HEMT_e_LowFieldMob (const PMI_Environment& env,
                    const PMI_AnisotropyType anisotype) :

HEMT_LowFieldMob (env, anisotype)
{
alfa=InitParameter ("alfa_e" ,  0.66);
  mumax=InitParameter ("mumax_e" , 1500);
  mumin=InitParameter ("mumin_e" , 295);
  b1=InitParameter ("b1_e" , -1.02);
  b2= InitParameter ("b2_e", -3.84);
  b3=InitParameter ("b1_e" ,  3.02);
  b4= InitParameter ("b2_e",  0.81);
  Nref= InitParameter ("Nref_e", 1e17);
```

```
  NN=InitParameter ("NN_e" ,  1e15);
  Tamb= InitParameter ("Tamb_e",  300);
}

class HEMT_h_LowFieldMob : public HEMT_LowFieldMob {

public:
  HEMT_h_LowFieldMob (const PMI_Environment& env,
                             const PMI_AnisotropyType anisotype);
  ~HEMT_h_LowFieldMob () {}
};

HEMT_h_LowFieldMob::
HEMT_h_LowFieldMob (const PMI_Environment& env,
                    const PMI_AnisotropyType anisotype) :

HEMT_LowFieldMob (env, anisotype)
{
  alfa=InitParameter ("alfa_h" ,  0.66);
  mumax=InitParameter ("mumax_h" , 1500);
  mumin=InitParameter ("mumin_h" , 295);
  b1=InitParameter ("b1_h" , -1.02);
  b2= InitParameter ("b2_h", -3.84);
  b3=InitParameter ("b1_h" ,  3.02);
  b4= InitParameter ("b2_h",  0.81);
  Nref= InitParameter ("Nref_e", 1e17);
  NN=InitParameter ("NN_e" ,  1e15);
  Tamb= InitParameter ("Tamb_e",  300);
}

extern "C"
PMI_DopingDepMobility* new_PMI_DopingDep_e_Mobility
  (const PMI_Environment& env, const PMI_AnisotropyType anisotype)
{
return new HEMT_e_LowFieldMob (env, anisotype);
}

extern "C"
PMI_DopingDepMobility* new_PMI_DopingDep_h_Mobility
  (const PMI_Environment& env, const PMI_AnisotropyType anisotype)
{
return new HEMT_h_LowFieldMob (env, anisotype);
}
```

Bibliography

[1] Comitato Guglielmo Marconi International. Breve storia del transistor. http://www.radiomarconi.com/marconi/transistor.html, July 2010.

[2] M.C.J.C.M. Krmer. *Gallium Nitride-based Microwave High-Power Heterostructure Field-Effect Transistors, design, technology, and characterization.* 2006.

[3] Jasprit Singh Umesh K. Mishra. *Semiconductor Device Physics and Design.* Springer, 2008.

[4] Rudiger Quay. *Gallium Nitride Electronics.* Springer, 2008.

[5] Young Chul Choi, Milan Pophristic, Ho-Young Cha, Boris Peres, Michael G. Spencer, and Lester F. Eastman. The effect of an fe-doped gan buffer on off-state breakdown characteristics in algan/gan hemts on si substrate. *Electron Devices, IEEE Transactions on*, 53(12):2926 –2931, dec. 2006. ISSN 0018-9383. doi: 10.1109/TED.2006.885679.

[6] LEDs Magazine. Led market ready for accelerated growth in lighting, display backlights and automotive applications. http://www.ledsmagazine.com/features/4/3/3, July 2010.

[7] Optics.org. Laser market to reach $ 8.8 billion in 2014. http://www.optics.org/article/42567, July 2010.

[8] O. Ambacher, J. Smart, J. R. Shealy, N. G. Weimann, K. Chu, M. Murphy, W. J. Schaff, L. F. Eastman, R. Dimitrov, L. Wittmer, M. Stutzmann, W. Rieger, and J. Hilsenbeck. Two-dimensional electron gases induced by spontaneous and piezoelectric polarization charges in n- and ga-face algan/gan heterostructures. *Journal of Applied Physics*, 85(6):3222 –3233, mar. 1999. ISSN 0021-8979. doi: 10.1063/1.369664.

[9] J. P. Ibbetson, P. T. Fini, K. D. Ness, S. P. DenBaars, J. S. Speck, and U. K. Mishra. Polarization effects, surface states, and the source of electrons in algan/gan heterostructure field effect transistors. *Applied Physics Letters*, 77(2):250 –252, jul. 2000. ISSN 0003-6951. doi: 10.1063/1.126940.

[10] Doo-Hyeb Youn, Jae-Hoon Lee, V. Kumar, Kyu-Seok Lee, Jung-Hee Lee, and I. Adesida. The effects of isoelectronic al doping and process optimization for the fabrication of high-power algan-gan hemts. *Electron Devices, IEEE Transactions on*, 51(5):785 – 789, may. 2004. ISSN 0018-9383. doi: 10.1109/TED.2004.825813.

[11] Young Chul Choi, Milan Pophristic, Ho-Young Cha, Boris Peres, Michael G. Spencer, and Lester F. Eastman. The effect of an fe-doped gan buffer on off-state breakdown characteristics in algan/gan hemts on si substrate. *Electron Devices, IEEE Transactions on*, 53(12):2926 –2931, dec. 2006. ISSN 0018-9383. doi: 10.1109/TED.2006.885679.

[12] Y.C. Choi, L.F. Eastman, and M. Pophristic. Effects of an fe-doped gan buffer in algan/gan power hemts on si substrate. *Solid-State Device Research Conference, 2006. ESSDERC 2006. Proceeding of the 36th European*, pages 282 –285, sep. 2006. ISSN 1930-8876. doi: 10.1109/ESSDER.2006.307693.

[13] S. Arulkumaran. Surface passivation effects in algan/gan hemts on high-resistivity si substrate. *Physics of Semiconductor Devices, 2007. IWPSD 2007. International Workshop on*, pages 317 –322, dec. 2007. doi: 10.1109/IWPSD.2007.4472507.

[14] P. B. Klein, J. A. Freitas, S. C. Binari, and A. E. Wickenden. Observation of deep traps responsible for current collapse in gan metalsemiconductor field-effect transistors. *Applied Physics Letters*, 75(25):4016 –4018, dec. 1999. ISSN 0003-6951. doi: 10.1063/1.125523.

[15] A. Y. Polyakov, N. B. Smirnov, A. V. Govorkov, A. V. Markov, T. G. Yugova, E. A. Petrova, H. Amano, T. Kawashima, K. D. Scherbatchev, and V. T. Bublik. Electrical properties and deep traps spectra in undoped and si-doped m-plane gan films. *Journal of Applied Physics*, 105(6):063708 –063708–9, mar. 2009. ISSN 0021-8979. doi: 10.1063/1.3078769.

[16] A. Y. Polyakov, N. B. Smirnov, A. V. Govorkov, A. V. Markov, T. G. Yugova, A. M. Dabiran, A. M. Wowchak, B. Cui, A. V. Osinsky, P. P. Chow, S. J. Pearton, K. D. Scherbatchev, and V. T. Bublik. Electrical and structural properties of aln/gan and algan/gan heterojunctions. *Journal of Applied Physics*, 104(5):053702 –053702–6, sep. 2008. ISSN 0021-8979. doi: 10.1063/1.2973463.

[17] A. Y. Polyakov, N. B. Smirnov, A. V. Govorkov, A. V. Markov, A. M. Dabiran, A. M. Wowchak, A. V. Osinsky, B. Cui, P. P. Chow, and S. J. Pearton. Deep traps responsible for hysteresis in capacitance-voltage characteristics of algan/gan heterostructure transistors. *Applied Physics Letters*, 91(23):232116 –232116–3, dec. 2007. ISSN 0003-6951. doi: 10.1063/1.2823607.

[18] A. Y. Polyakov, N. B. Smirnov, A. V. Govorkov, A. V. Markov, T. G. Yugova, E. A. Petrova, A. M. Dabiran, A. M. Wowchak, A. V. Osinsky, P. P. Chow, S. J. Pearton, K. D. Shcherbatchev, and V. T. Bublik. Semi-insulating, fe-doped buffer layers grown by molecular beam epitaxy. *Journal of The Electrochemical Society*, 154(9):H749–H754, 2007. doi: 10.1149/1.2749094. URL `http://link.aip.org/link/?JES/154/H749/1`.

[19] H. K. Cho, C. S. Kim, and C.-H. Hong. Electron capture behaviors of deep level traps in unintentionally doped and intentionally doped n-type gan. *Journal of Applied Physics*, 94(3):1485 –1489, aug. 2003. ISSN 0021-8979. doi: 10.1063/1.1586981.

[20] Masashi Kubota, Takeyoshi Onuma, Yujiro Ishihara, Akira Usui, Akira Uedono, and Shigefusa F. Chichibu. Thermal stability of semi-insulating property of fe-doped gan bulk films studied by photoluminescence and monoenergetic positron annihilation techniques. *Journal of Applied Physics*, 105(8):083542 –083542–9, apr. 2009. ISSN 0021-8979. doi: 10.1063/1.3110205.

[21] Jungwoo Joh and J.A. del Alamo. Impact of electrical degradation on trapping characteristics of gan high electron mobility transistors. *Electron Devices Meeting, 2008. IEDM 2008. IEEE International*, pages 1 –4, dec. 2008. ISSN 8164-2284. doi: 10.1109/IEDM.2008.4796725.

[22] T. Okino, M. Ochiai, Y. Ohno, S. Kishimoto, K. Maezawa, and T. Mizutani. Drain current dlts of algan-gan mis-hemts. *Electron Device Letters, IEEE*, 25(8):523 – 525, aug. 2004. ISSN 0741-3106. doi: 10.1109/LED.2004.832788.

[23] Jungwoo Joh and Jesus A. del Alamo. Mechanisms for electrical degradation of gan high-electron mobility transistors. *Electron Devices Meeting, 2006. IEDM '06. International*, pages 1 –4, dec. 2006. doi: 10.1109/IEDM.2006.346799.

[24] J.A. del Alamo and J. Joh. Gan hemt reliability. *Microelectronics Reliability*, 49(9-11):1200 – 1206, 2009. ISSN 0026-2714. doi: DOI:10.1016/j.microrel.2009.07.003. 20th European Symposium on the Reliability of Electron Devices, Failure Physics and Analysis, 20th European Symposium on the Reliability of Electron Devices, Failure Physics and Analysis.

[25] S.C. Binari, P.B. Klein, and T.E. Kazior. Trapping effects in gan and sic microwave fets. *Proceedings of the IEEE*, 90(6):1048 – 1058, jun. 2002. ISSN 0018-9219. doi: 10.1109/JPROC.2002.1021569.

[26] S. Arulkumaran, T. Egawa, H. Ishikawa, T. Jimbo, and Y. Sano. Surface passivation effects on algan/gan high-electron-mobility transistors with sio2, si3n4, and silicon

oxynitride. *Applied Physics Letters*, 84(4):613 –615, jan. 2004. ISSN 0003-6951. doi: 10.1063/1.1642276.

[27] Gaudenzio Meneghesso, Fabiana Rampazzo, Peter Kordos, Giovanni Verzellesi, and Enrico Zanoni. Current collapse and high-electric-field reliability of unpassivated gan/algan/gan hemts. *Electron Devices, IEEE Transactions on*, 53(12):2932 –2941, dec. 2006. ISSN 0018-9383. doi: 10.1109/TED.2006.885681.

[28] Young Chul Choi, Milan Pophristic, Ho-Young Cha, Boris Peres, Michael G. Spencer, and Lester F. Eastman. The effect of an fe-doped gan buffer on off-state breakdown characteristics in algan/gan hemts on si substrate. *Electron Devices, IEEE Transactions on*, 53(12):2926 –2931, dec. 2006. ISSN 0018-9383. doi: 10.1109/TED.2006.885679.

[29] S. Karmalkar and U.K. Mishra. Enhancement of breakdown voltage in algan/gan high electron mobility transistors using a field plate. *Electron Devices, IEEE Transactions on*, 48(8):1515 –1521, aug. 2001. ISSN 0018-9383. doi: 10.1109/16.936500.

[30] W. Saito, M. Kuraguchi, Y. Takada, K. Tsuda, I. Omura, and T. Ogura. Influence of surface defect charge at algan-gan-hemt upon schottky gate leakage current and breakdown voltage. *Electron Devices, IEEE Transactions on*, 52(2):159 – 164, feb. 2005. ISSN 0018-9383. doi: 10.1109/TED.2004.842710.

[31] R. Gaska, A. Osinsky, J.W. Yang, and M.S. Shur. Self-heating in high-power algan-gan hfets. *Electron Device Letters, IEEE*, 19(3):89 –91, mar. 1998. ISSN 0741-3106. doi: 10.1109/55.661174.

[32] R. Gaska, Q. Chen, J. Yang, A. Osinsky, M. Asif Khan, and M.S. Shur. High-temperature performance of algan/gan hfets on sic substrates. *Electron Device Letters, IEEE*, 18(10):492 –494, oct. 1997. ISSN 0741-3106. doi: 10.1109/55.624930.

[33] I. Kallfass, H. Schumacher, and T.J. Brazil. A unified approach to charge-conservative capacitance modelling in hemts. *Microwave and Wireless Components Letters, IEEE*, 16(12):678 –680, 2006. ISSN 1531-1309. doi: 10.1109/LMWC.2006.885627.

[34] N.B. Gorev, I.F. Kodzespirova, S.A. Kostylev, Yu.A. Kovalenko, and E.F. Prokhorov. Effect of deep traps on the low-frequency capacitance-voltage characteristic of selectively doped alxga1-xas/gaas heterostructures. pages 661 –663, 1998. doi: 10.1109/ICSICT.1998.785976.

[35] S. Takatani and Cheng-Duan Chen. Accurate hemt switch large-signal device model derived from pulsed-bias capacitance and current characteristics. pages 1 –4, 2009. ISSN 1550-8781. doi: 10.1109/csics.2009.5315652.

[36] E. J. Miller, X. Z. Dang, and E. T. Yu. Gate leakage current mechanisms in algan/gan heterostructure field-effect transistors. *Journal of Applied Physics*, 88 (10):5951 –5958, nov. 2000. ISSN 0021-8979. doi: 10.1063/1.1319972.

[37] J.W. Chung, J.C. Roberts, E.L. Piner, and T. Palacios. Effect of gate leakage in the subthreshold characteristics of algan/gan hemts. *Electron Device Letters, IEEE*, 29 (11):1196 –1198, nov. 2008. ISSN 0741-3106. doi: 10.1109/LED.2008.2005257.

[38] Yu-Syuan Lin, Yi-Wei Lain, and S.S.H. Hsu. Algan/gan hemts with low leakage current and high on/off current ratio. *Electron Device Letters, IEEE*, 31(2):102 –104, feb. 2010. ISSN 0741-3106. doi: 10.1109/LED.2009.2036576.

[39] Junji Kotani, Masafumi Tajima, Seiya Kasai, and Tamotsu Hashizume. Mechanism of surface conduction in the vicinity of schottky gates on algan/gan heterostructures. *Applied Physics Letters*, 91(9):093501 –093501–3, aug. 2007. ISSN 0003-6951. doi: 10.1063/1.2775834.

[40] Z.-Q. Fang, D. C. Look, X.-L. Wang, Jung Han, F. A. Khan, and I. Adesida. Plasma-etching-enhanced deep centers in n-gan grown by metalorganic chemical-vapor deposition. *Applied Physics Letters*, 82(10):1562 –1564, mar. 2003. ISSN 0003-6951. doi: 10.1063/1.1560562.

[41] M. Farahmand, C. Garetto, E. Bellotti, K.F. Brennan, M. Goano, E. Ghillino, G. Ghione, J.D. Albrecht, and P.P. Ruden. Monte carlo simulation of electron transport in the iii-nitride wurtzite phase materials system: binaries and ternaries. *Electron Devices, IEEE Transactions on*, 48(3):535 –542, mar. 2001. ISSN 0018-9383. doi: 10.1109/16.906448.

[42] A. Rusu, A.M. Ionescu, and A. Chovet. Avalanche phenomena in deeply depleted mos capacitors. 2:645 –650 vol.2, September 1995. doi: 10.1109/ICMEL.1995.500942.

[43] J. Li, S.J. Cai, G.Z. Pan, Y.L. Chen, C.P. Wen, and K.L. Wang. High breakdown voltage gan hfet with field plate. *Electronics Letters*, 37(3):196 –197, February 2001. ISSN 0013-5194. doi: 10.1049/el:20010091.